THE FLORIDA STATE UNIVERSITY

COLLEGE OF ARTS AND SCIENCES

SYNTHESIS AND CHARACTERIZATION OF DILUTE MAGNETIC
SEMICONDUCTOR NANOPARTICLES

By

DONNY MAGANA

A Dissertation submitted to the
Department of Chemistry
in partial fulfillment of the
requirements for the degree of
Doctor of Philosophy

Degree Awarded:
Fall Semester, 2007

The members of the Committee approve the Dissertation of Donny Magana defended on August 30, 2007.

Geoffrey F. Strouse
Professor Directing Dissertation

Stephan von Molnár
Outside Committee Member

Naresh Dalal
Committee Member

Sir Harold Kroto
Committee Member

The Office of Graduate Studies has verified and approved the above named committee members.

To my parents, whose struggle made this journey possible.

ACKNOWLEDGEMENTS

Life adventures are nothing without the people that help along the way. My graduate $\frac{decade}{2}$ would have been far less adventurous without moving literally across the US to the great state of Florida. Without this experience I would have missed on a plethora of new friends and colleagues.

I would like to thank Professor Geoff Strouse for keeping me on my toes these five years. For teaching me more than just research and for giving me the opportunity to learn the vast amount of research techniques I now know.

My committee for the help, patience, and the knowledge you were always willing to give.

I would like to thank my family for listening to all of my complaints even if they were small. To my brothers who are a great example of perseverance. Elvis, the tactics you employ to get though life inspire nothing but greatness. Andres, you inspire the ability to do anything you set your mind to. Luis, your knowledge on the abstracts of space and time make me jealous of how little I know. Jesus, I see myself in you in the way you handle the desire for more knowledge. Naomi, someday you will understand the great distance that separated us. I wish I knew your technique in delegating what you want. My parents who have inspired me to never give up.

Dr. Naresh Dalal, I couldn't have found a better friend, colleague and mentor. Our lives are more similar than you may think. Thank you for the help.

Dr. Stephan von Molnar, it was a lot easier to ask you questions since you can recall most papers. Your vast knowledge is an inspiration. Thank you for putting up with my questions and comments.

Dr. Tegi Kim, my learning curve increases exponentially every time I converse with you. The conversation with you are nothing but inspiration to the knowledge one can obtain. You are also a great friend.

Khalid, I had fun attempting science with you. Your a good friend.

Jeff, this adventure couldn't have been any more fun with out you.

Martha, only a few people how much I owe you.

Greg, thanks for prescribing the right antidote, and for the couch.

Mani, I couldn't have had a better neighbor.

Aaron, your car projects kept a dream alive.

Andy, you kept my faith alive along with my outlook about life.

The Dalal group couldn't have challenged my brain more often, thank you.

The Strouse group, thank you for the help provided. The people who shared this adventure know the sacrifices some of us had to make and the lives it took.

I would also like to thank the many other people I don't mention here who encouraged me to continue my endeavor to know more by inspiring the greatness of science.

TABLE OF CONTENTS

LIST OF TABLES

LIST OF FIGURES

ABSTRACT

This dissertation studies the optical and magnetic properties of CdSe, including alloys which incorporate Mn (II) and sulfur. The first chapter explains the theory used to analyze the data and the properties expected for condensed phase materials at the nanoscale. The second chapter probes the magnetic and EPR results for Mn doped CdSe under different synthetic environments. The process of annealing was found to cluster the manganese resulting in ferromagnetic exchange. The third chapter involves further analysis of Mn doped CdSe with the possibility of sulfur incorporation from the synthetic strategy employed where a spin wave was observed due to the ferromagnetic interactions in the sample. The presence of carriers helps explain reasons for the observation of a spin wave in Mn:CdSSe as observed in the heat capacity measurements. The fourth chapter is the magneto-absorption study on the Mn doped CdSSe in comparison to CdSSe. The sulfur incorporation may have affected the results. The fifth chapter is a study of sulfur incorporation in CdSe and the effects on the magneto-photoluminescence properties. The techniques employed include a magnetic field to separate the spin levels and determine which of the states was influenced by the sulfur incorporation. The sixth chapter involves an exciton temperature dependent study of CdSSe in a magnetic field.

CHAPTER 1

INTRODUCTION

Nanomaterials have been the focus of technology advancements for many years, as replacements of phosphors in solid state lighting, lasers, magnetic probes, and spin related devices to name a few[1, 2, 3]. Quantum confinement in general opens a degree of freedom to manipulate the desired electronic properties of a material by systematically tuning the size. Of particular interest has been the magnetic doping at the nanoscale, which has been an area of interest ever since the early efforts to dope II-VI semiconductors [4, 5, 6, 7, 8, 9, 10, 11, 12, 13, 14, 15, 16, 17, 18]. II-VI materials are expected to be paramagnetic or antiferromagnetic, although the presence of carriers can lead to long range coupling of the manganese and the observation of ferromagnetism. The major impetus for incorporating paramagnetic donor ions into nanoscale II-VI semiconductors revolves around the hope of observing large Zeeman splitting of the excitonic transition of the host lattice induced by the presence of the magnetic donor ions. The physics of donor atom inclusion into bulk materials is well-studied and the fundamental changes in the magnetic and optical measurements have been probed for decades[5, 8, 7, 10, 11, 12, 13, 19, 2]. The influence of quantum confinement on the orbital mixing between the donor atom and band levels is still an area of intense curiosity[20]. Although controlling the type, location, and concentration of donor atoms is generally achievable in bulk and by engineered nanomaterials [21], donor atom inclusion into thermally grown nanocrystals has proven difficult[20, 22, 23, 24, 25, 26, 27, 28].

The major problem has been that donor atom inclusion into CdSe is still a conundrum. The major reasons are attributed to a combination of lattice self-healing processes during the high temperature reaction conditions necessary for formation of nanocrystals and to contributions from differences in the solubility product (K_{sp}) for the ions of interest [29]. The problems associated with K_{sp}, which are well-defined in the crystallization literature[29], have

been overcome by use of a pre-doped single source precursor. Self-healing on the other hand is potentially the more significant barrier to doping of thermally grown nanocrystals due to the presumed exclusion of defect ions as the nanocrystal heals defects that are kinetically trapped in the rapidly growing material.

The dissertation develops the concept of controlled ion doping of CdSe to produce nanocrystalline dilute magnetic semiconductor (DMS) materials. The material are analyzed by a set of optical and magnetic experiments to more fully understand the exchange dynamics in a size confined system. While the "particle in a box" picture is effective for undoped systems, the Coulomb interaction between the electron and the hole, is too simple to use for doped material. At sizes where exciton Coulombic interactions are significant, there are also effects on the phonons as a result of the large surface and disorder in the structure due to donor inclusion. The level of detail pertaining to the interaction that phonons play in the tuning of the electronic properties help explain some of the abstract results in both magnetism and electron exchange in these materials. To tackle this problem it is necessary to understand the intrinsic properties of the host lattice and how the incorporation of ions, in general, influences the electronic properties. The experiments performed include electron paramagnetic resonance (EPR), magnetic susceptibility and heat capacity, magneto-photoluminescence and magnetic circular dichroism. Intentional doping of CdSe nanocrystals doped with Mn and sulfur were carried out and all measurements are compared to the undoped system. The effect of induced clustering is analyzed for the Mn doped CdSe where an annealing step in the synthesis of the nanocrystals is used to observe the effect clustering of Mn on the magnetic properties (Chapter 2). This is used to explain the spinwave formation at high concentration of manganese (Chapter 3). Using magnetic circular dichroism one can see the effect of Mn on the electronic groundstate of CdSe (Chapter 4). Lastly in attempt to explain the carriers in the heat capacity inclusion of sulfur is analyzed in the magneto-photoluminescence as a function of magnetic field (Chapter 5) and temperature (Chapter 6). This helps explain the delocalization of the polaron to the confines of the particle's size, observed for the first time.

The introduction outlines the theory needed to understand dimensionally confined DMS systems. This chapter summarizes the optical properties to be expected from a CdSe semiconductor, the effect on the magnetic properties upon addition of a magnetic ion, and how quantum confinement plays a role. As a general theme the interplay of the different

degrees of freedom between the lattice, the electronic, and magnetic properties are discussed. The following theoretical summary of the theory used followed several books including those by Flurry[30], Hammermesh[31], Struve[32], and Kotov[33] for the spectroscopy and Kittel[34], Aschcroft and Mermin[35], and Gopal[36] for the physical characterization.

1.1 Semiconductors

A simple review of condensed matter physics is important if the physical properties of nanocrystalline semiconductors are to be understood and more importantly the influence of doping. The bandgap of a semiconductor originates from the projection of the atomic orbitals in a periodic lattice as described by the Bloch approximation. The atomic orbitals are periodic for a set of precise atomic positions. Uncertainty lies only in the momentum of the crystal. In this study, the wurtzite structure of CdSe is a direct band gap containing C_{6v}^4 symmetry, where the translational symmetry is shown in figure 1.1A. Using the Bravais lattice one can arrive at the reciprocal lattice for the wurtzite structure. To convert the Bravais lattice (a, b, c) to the reciprocal lattice one assumes the reciprocal lattice (g_1, g_2, g_3) vectors are basic vectors of the Bravais lattice. The conversion factor for a hexagonal case is ($g_1 = (\frac{2\pi}{a\sqrt{3}}, \frac{-2\pi}{a}, 0)$, $g_2 = (\frac{4\pi}{a\sqrt{3}}, 0, 0)$, $g_3 = (0, 0, \frac{2\pi}{c})$). Using the reciprocal lattice one can begin to consider the Brillouin zones over which all electronic and magnetic behavior is described.

As observed in figure 1.1B the Brillouin zone for the hexagonal lattice shows the symmetry points in k-space (momentum space) with Γ at the point of origin. The symmetry at any point can be described in terms of the reducible representation or in Koster notation. For example at the gamma point for a hexagonal lattice the group describing the symmetry is a G_{12}^3 which generates a set of energy levels defined by their symmetry (Table 1.1). The same procedure can be carried out to describe the symmetry at any point in the different Brillouin space zones (M, A, K). The parts of the band structure of major importance are the states composing the valence and conduction band (Fig 1.2). For CdSe, as an unperturbed wurtzite structure, the valence and conduction band are composed of Γ_6 and Γ_1 as observed in figure 1.2.The cross product of these two polarized waves ($\Gamma_6 \times \Gamma_1$) give rise to the unperturbed wurtzite exciton that has a formal symmetry of a degenerate E state as observed in table 1.1.

3
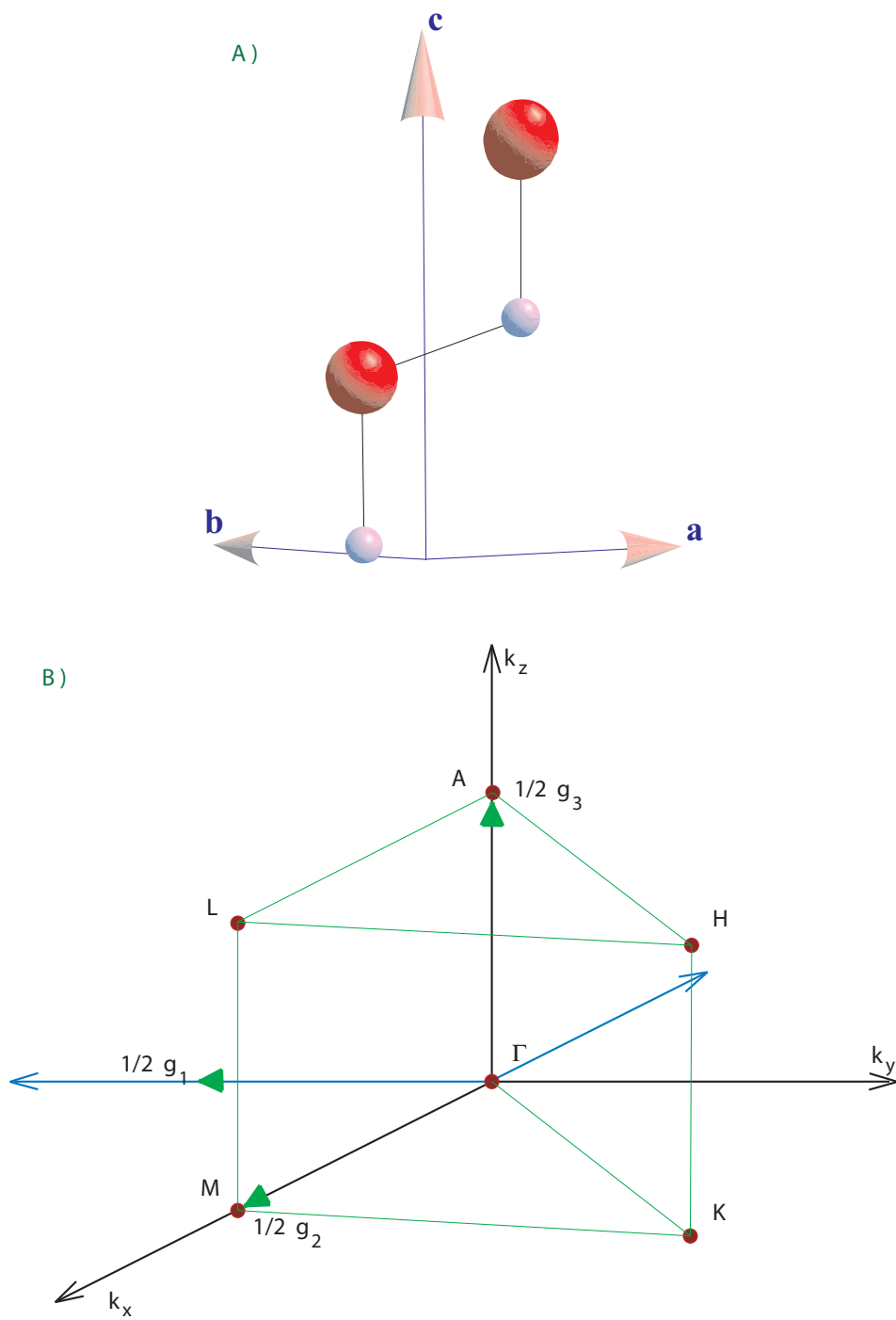
Figure 1.1: A) 4 atom primitive cell of a wurtzite CdSe. B) Symmetry points of the hexagonal lattice as a function of wavevector k.

Table 1.1: representation table for a C_{6v}^4

C_{6v}^4		R_1	R_2	R_3	R_4	R_5	R_6
	c	A_1	A_2	B_1	B_2	E_2	E_1
G_{12}^3		Γ_1	Γ_2	Γ_3	Γ_4	Γ_5	Γ_6
G_4^2		M_1	M_2	M_3	M_4	-	-

Table 1.2: C_{6v} symmetry table

C_{6v}	E	$2C_6$	$2C_3$	C_2' C_2	$3\sigma_v'$ $3\sigma_v$	$3\sigma_d'$ $3\sigma_d$	E'	$2C_6'$	$2C_3'$	
A_1	1	1	1	1	1	1	1	1	1	z
A_2	1	1	1	1	-1	-1	1	1	1	
B_1	1	-1	1	-1	1	-1	1	-1	1	
B_2	1	-1	1	-1	-1	1	1	-1	1	
E_1	2	1	-1	-2	0	0	2	1	-1	(x,y)
E_2	2	-1	-1	2	0	0	2	-1	-1	
$E_{1/2}$	2	$\sqrt{3}$	1	0	0	0	-2	-$\sqrt{3}$	-1	
$E_{3/2}$	2	0	-2	0	0	0	-2	0	2	
$E_{5/2}$	2	-$\sqrt{3}$	1	0	0	0	-2	$\sqrt{3}$	-1	

5
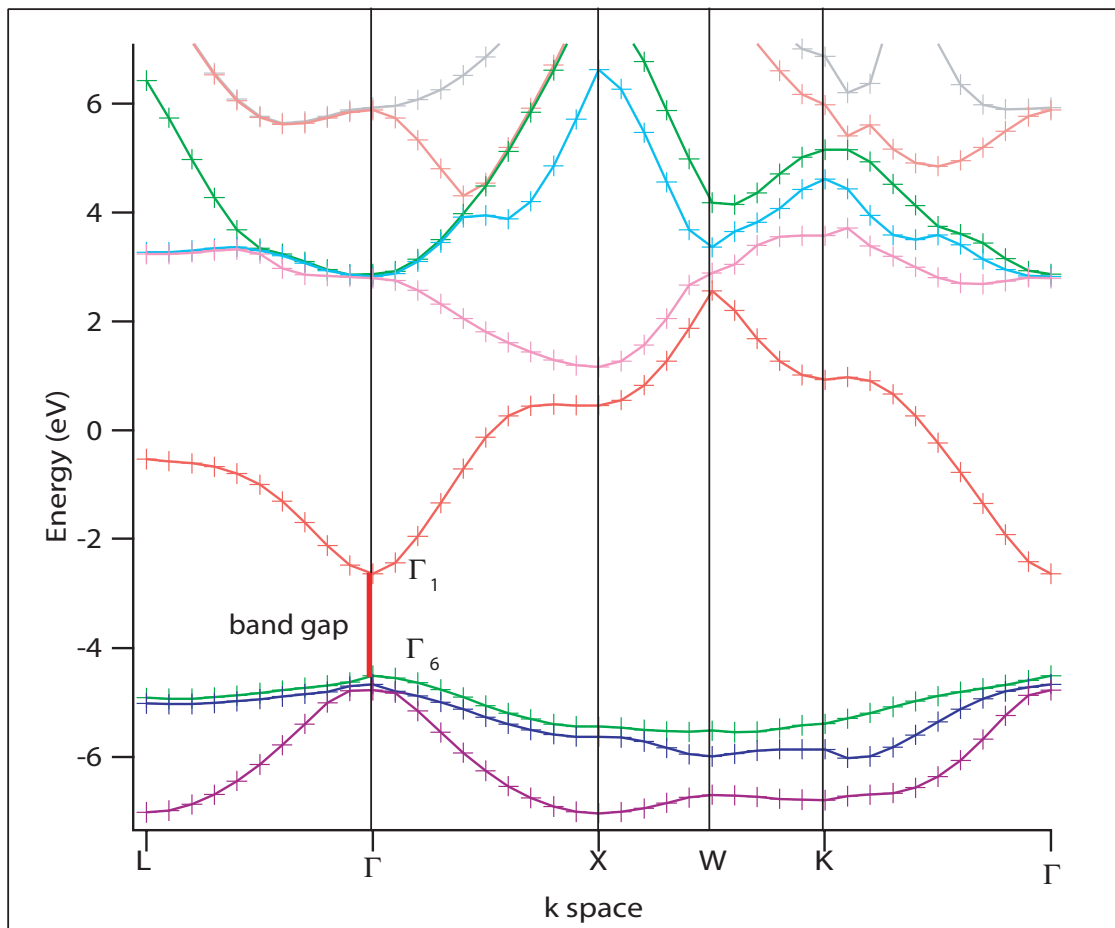
Figure 1.2: Band diagram of CdSe using a perturbation to the cubic structure to form degenerate valence band.

In order to include the spin of the exciton state, one needs to use double group symmetry to represent the spinor levels in the unit cell. The double group produces degenerate states by including a rotational component. The rotational constant used depends on the order of the group elements involved.

In the C_n groups the double group representation is represented in a generalized form as

$$\chi(A) = e^{\frac{2\pi i l m}{g}} \qquad (1.1)$$

where l is the order of the element and g is the order of operation. The element characters are then determined by taking the powers of eqn 1.1 (m). The half integers (m) give doubled-valued representations while the whole integers are single- valued. For a wurtzite structure the state symmetry follows table 1.2 where the conduction and valence band are composed of the $E_{1/2}$ and $E_{3/2}$, respectively (Table 1.2). The exciton symmetry the cross product of these two states. This produces a quadruplely degenerate exciton $E_1 + E_2$. The second excitonic transition from the $E_{1/2} \times E_{1/2}$ transition results in a $E_1 + A_1 + A_2$ degenerate state. The crystal field state also results in a $E_1 + A_1 + A_2$ state as in the second transition. The exciton levels can couple to phonons of the same symmetry as long as they lie in the same geometrical axis. The splitting of the different energy levels is influenced primarily by changes in the symmetry of the atoms, but at the nanoscale this is an important parameter that complicates the observed optical and magnetic behavior.

1.2   Optical properties

The optical properties of CdSe can be explained using the symmetry operators generated in section 1.1. In a nanocrystalline semiconductor the absorption of an electron generates an exciton which is describable by the hydrogenic model. Changes in the symmetry due to non-spheroidal shape, surface atoms, and presence of dopant ions complicate the energy level model. To understand the nature of the optical properties (absorption and photoluminescence) the limiting conditions need to be described. Two types of excitons can be described, the Wannier and the Frohlich excitons. These form the basis for describing exciton projection in a semiconductor lattice and will be useful in interpretation of nanocrystalline CdSe photophysics.

1.2.1   Wannier

A Wannier (free) exciton can be described as a hydrogen atom where the ionization energy is dependent on the effective mass of the electron and hole, as well as the exciton binding energy, defined by the Coulomb interaction between the electron and hole pair. For the electron and hole to have the same momentum, they must move at different velocities and hence differences in the curvature of the bands, in other words to stay together in the crystal their translational velocities must be the same. This restricts the range over which the exciton can exist in addition to the electron-electron and hole-hole interactions which also restrict the exciton translational range. In effect using the hydrogen model, the exciton radius is the size of the material bohr radius (CdSe = 5.0 nm).

Using quantum mechanics, the particle in a box, and the free electron approximation the unperturbed time-independent Schrodinger equation follows

$$\left(\frac{-\hbar^2}{2m}\right)\nabla^2\psi = E\psi \tag{1.2}$$

where the generalized wavefunction is

$$\psi(x,y,z) = A(coskx + cosky + coskz) + B(sinkx + sinky + sinkz) \tag{1.3}$$

with the initial boundary conditions that the electron is confined to the box ($\psi(0,0,0) = 0$). The trial wavefunction must also be zero at the boundary conditions such that $k_{x,y,z} = 2\pi n/L$ where L is the size of the box. The normalization constant can be determined when calculating the probability of the electron being inside the box. The resulting energy is equal to

$$E = \frac{\hbar^2(k_x^2 + k_y^2 + k_z^2)}{2m} \tag{1.4}$$

where the energy is based on the atomic lattice positions in momentum space notation($k_{x,y,z}$). The momentum is then equal to the wavevector if Planck's constant is included (p=$\hbar$(k_x, k_y, k_z)). Just like a particle in a box the exciton states can also be labeled as s, p, and d exciton states. A free exciton is also weakened by internal fields that can exceed the exciton Coulombic interaction (binding energy) resulting in the destruction of the exciton.

1.2.2   Frohlich

The Frohlich exciton is a phonon coupled to an exciton that produces a change in the electron-hole effective mass. This effect can lead to a self trapping as a result of the formation of

the polaron where the electron- phonon coupling strength can be measured. In this case an electron coupling to a lattice phonon can produce a pathway for fast recombination. For a polar semiconductor, the coupling occurs between the LO (Longitudinal Optical) modes and the exciton states with the same symmetry. Contributions from the transverse (TO) or acoustic modes typically have no contribution.

Phonon contributions play a role in semiconductor recombination producing a nonradiative pathway or state mixing. The use of a virtual state allows the el-ph interaction to be described by separating the individual interactions. The use of creation and annihilation operators simplifies the explanation for the formation of the instantaneous dipole moment in the electron-field interaction. For a single electron transition using the weak electric field approximation, the instantaneous moment gives rise to an absorption. In the case of the phonon a harmonic oscillation is assumed to describe the phonons. The result is a hamiltonian that involves the electron-field interaction and the phonon-field interaction. To explain the interactions that give rise to the el-ph coupling it is necessary to explain the Hamiltonian that describes the system

$$H = H_e + H_{el-ph} + H_p \tag{1.5}$$

where the Hamiltonian is composed of the electron interaction (H_e), the electron-phonon interaction (H_{el-ph}), and the lattice phonon (H_p). H_{el-ph} is assumed to be non-zero when the electron and phonon are in the same space and time to transfer their momentum. It assumes that the time independent Schrödinger equation cannot treat the system correctly and requires the wavefunction to be time dependent in order to allow enough time for the movement of the lattice to influence the electronic properties.

Quantum mechanically, the electron Hamiltonian describes the excitonic transition by promoting an electron from the groundstate into the excited state ($m \rightarrow n$). The phonon Hamiltonian involves the motion of the atoms as phonons where the absorption of a phonon is similar to that of an electron ($g \rightarrow h$). The electron- phonon interaction involves a combination of both the electron and phonon at the same space and time to produce an absorption that produces a phonon absorption. The electron having lost energy absorbed by the phonon then is capable of emitting radiatively by exciton recombination. In the next section we describe the single electron transition as an optical absorption but for the mean time the only important part is the transition matrix and how it involves the phonon

contribution. In the single electron transition matrix, we involve an intermediate excited state that involves the electron phonon interaction

$$W_{mn} = \frac{<n|H|g><g|H|h><h|H|m>}{(E_g - E_m)(E_h - E_m)} \tag{1.6}$$

where the absorption from state m to h involves the interaction of light with the semiconductor dipole producing a virtual (absorpton of a phonon) which then relaxes into an excited phonon state. Mathematically, using a harmonic oscillator to explain the polarization in the absence of an electric field, one can write

$$\ddot{P}(R) + \omega^2 P(R) = 0 \tag{1.7}$$

where P(R) is the polarization of the lattice. The solutions include a generalized P(R) $(P(R) = A_1 e^{\omega R} + A_2 e^{-\omega R})$ solution that is dependent on the frequency (ω) of the lattice vibration. When the electron interaction is added to the polarization of the lattice, the polarization of the system can be solved using an inhomogeneous differential equation that places the vibrations in the same space as the electronic polarization.

$$\ddot{P}(R) + \omega^2 P(R) = \frac{1}{4\pi} \left(\frac{1}{\varepsilon_\infty} - \frac{1}{\varepsilon} \right) D(R) \tag{1.8}$$

where D(R) is the electric displacement in the material and ε and ε_∞ are the static and high frequency dielectric constants, respectively allowing one to determine the instance when there is an interaction present to give rise to the electron-phonon interaction. The energy of the phonon involved will be evident in the temperature dependent absorption and photoluminescence. The expectation is to have the lowest LO phonon be the main contributor to the el-ph coupling. Using an el-ph coupling constant of 0.1 which is predicted for CdSe[37], the temperature dependence can be simulated for the different LO phonon energies (1.3) using a correction to the band-gap that involves the phonon contribution

$$E(T) = E_o - \alpha h\omega(Coth[h\omega/k_B T] - 1/(h\omega/k_B T)) \tag{1.9}$$

where ω is the frequency of the phonon and α is the electron phonon coupling constant related to the polaron size by the expression

$$\alpha = \left(\frac{1}{\epsilon_\infty} - \frac{1}{\epsilon_0} \right) \frac{e^2}{2r_p^2} \frac{1}{\hbar\omega_L} \tag{1.10}$$

where ϵ_∞ and ϵ_0 are the high and low frequency dielectric constants, e is the charge of an electron, r_p is the polaron radii, and ω_L is the LO phonon frequency. This allows quantitative analysis of the phonons involved in the exciton formation and recombination.
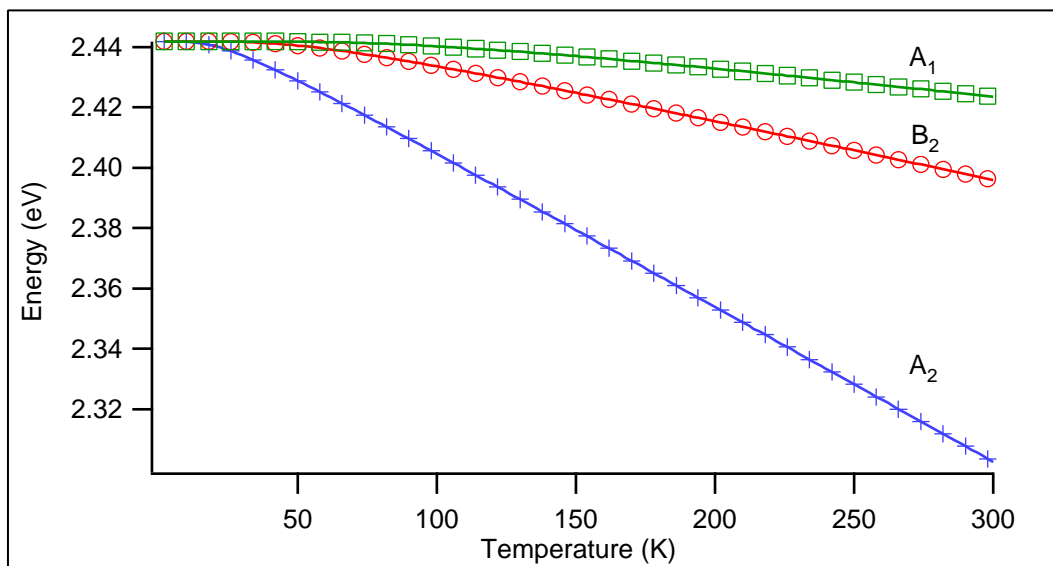
Figure 1.3: Temperature dependent bandgap as a function of three phonon frequencies A_1=210 cm $^{-1}$, B_2=110 cm $^{-1}$, and A_2=43 cm $^{-1}$[38].

1.3   Optical spectroscopy

The interaction of light as an electric field with a medium is fully explained by the use of time dependent and independent Shrödinger equations, where the total Hamiltonian to be used contains the natural state of the system $\hat{H}_o$, electric field $\hat{H}_e$ and the interaction (A) between both. Using the ground state wave function of the system $|\Psi_0(r,t)>= e^{-iE_n t/\hbar}|\psi_n(r)>$ one can simply see the superposition of the different contributions. First it is necessary to treat the interaction of an electric field as it comes in contact with the system.

1.3.1   Linear polarized spectroscopy

The field has the wave form $E = E_o cos(\omega t - kz)$ for the electric field where ω is the angular frequency and k is the wavenumber. The use of Maxwell's equations show that $E_o \cdot k = B_o \cdot k = 0$ where in the direction of propagation (k) two components of the electromagnetic field exist that shows that the electric (E) and magnetic (B) fields oscillate $\pi/2$ from each other. When the electric field is at its maximum, the magnetic term is a minor component and vice versa. In dealing with an electric field passing through a semiconductor, the easiest approach is to approximate the system as an insulator, where no conductivity will be present. The presence of an electric field will cause a motion of charges in the material and in turn polarize the charges. For the case of the electronic polarization, it is a purely covalent interaction that induces a displacement of electron nuclear charge ($D_\varepsilon = \varepsilon_o \varepsilon_r E$), proportional to the magnitude of the electric field (E) times the internal field (dielectric constant, ε_r). The dielectric constant (ε_r) is material specific because it is proportional to the polarization in the material and therefore electron nuclear-distance ($P = \varepsilon_o E(\varepsilon_r - 1) = Nqd$) where N is the number of atoms per volume, q is the nuclear charge and d is the electron-nuclear distance. The charge and electron-nuclear distance is the electric dipole that is formed as a result of the electric field. The induced dipole is parallel to the direction of propagation in the electric field. The induced dipole contains the total energy from the applied electric field that includes the unperturbed energy and the energy associated with the induced dipole.

A particle in the presence of the electric field will feel a potential related to its charge. The potential felt follows Maxwell's equations where the potential (D) is orthogonal to the electric and magnetic field.

$$B = \nabla \times D \tag{1.11a}$$

$$\nabla \times E = -\frac{\partial B}{\partial t} = -\nabla \times \dot{D} \qquad (1.11\text{b})$$

$$\nabla \times (E + \dot{D}) = 0 \qquad (1.11\text{c})$$

As a result of the electrostatic interactions E=-$\nabla\phi$ and if Maxwell's equation (1.11b) is obeyed then E=-$\nabla\phi$-$\frac{\partial D}{\partial t}$. The force experienced by the particle is dependent on the mass (m) and charge (e), where in terms of the potential D the force is described by eqn 1.12.

$$F = e[E + v \times B] = \frac{d}{dt}m\dot{x} \qquad (1.12\text{a})$$

$$F = e\left[-\nabla(\phi - v \cdot D) - \frac{\partial D}{\partial t}\right] = \frac{d}{dt}m\dot{x} \qquad (1.12\text{b})$$

The total energy felt will be proportional to the kinetic energy $(1/2m\dot{x}^2)$ of the particle minus the potential energy (V) applied.

$$\frac{d}{dt}\left(\frac{\partial(1/2m\dot{x}^2 - V)}{\partial \dot{x}}\right) - \frac{\partial(1/2m\dot{x}^2 - V)}{\partial x} = 0 \qquad (1.13)$$

$$\frac{d}{dt}(m\dot{x} + eD) - e\frac{\partial(v \cdot D - \phi)}{\partial x} = 0 \qquad (1.14)$$

If the total force of the system is conservative then a Lagrangian equation can generalize the conservative forces as it should equal zero. Substitution of the potential V for the force components in equation 1.12 one gets all the components for the formation of the electrostatic and dipole components for the Hamiltonian. The Lagrangian equation used to describe the potential is shown in equation 1.15.

$$L = \frac{1}{2}m\dot{x}^2 + e(v \cdot D) - e\phi \qquad (1.15)$$

The Hamiltonian in terms of conjugate momentum is the Legendre of the Lagrangian equation (1.15) written as equation for 3N coordinates yields

$$H = \sum_{i=1}^{3}\left(\frac{\partial L}{\partial \dot{x}}\right)\dot{x} - \frac{1}{2}m\dot{x}^2 - e(v \cdot D) + e\phi \qquad (1.16\text{a})$$

$$= \frac{1}{2m}(m\dot{x})^2 + e\phi \qquad (1.16\text{b})$$

$$m\dot{x} = p - eD \qquad (1.16\text{c})$$

$$\therefore H = \frac{1}{2m}(p - eD)^2 + e\phi \qquad (1.16\text{d})$$

13

where the electromagnetic field needs to have a restoring force that shows up as a potential added to the Hamiltonian. As mentioned above, the Hamiltonian needs to have the unperturbed energies of the particles ground state and the energy that arises from the interaction of an electric field with the particle. By separating the Hamiltonian components we can recover the interaction sought.

$$H = \left[-\frac{\hbar^2}{2m}\nabla^2 + V \right] + \left[\frac{e^2 D^2}{2m} - \frac{\hbar e}{im}(D \cdot \nabla) \right] \equiv \hat{H} + A \tag{1.17}$$

In the weak field limit $\frac{e^2 D^2}{2m}$ goes to zero and the only contribution to the interaction of the electric field is $\frac{i\hbar e}{m} D \cdot \nabla$. To observe a transition it is first assumed that the electric field is linearly polarized for simplicity. The groundstate time dependent wave function exists in its initial state. The function is operated on a coefficient that makes the wavefunction obey the initial conditions

$$|\Psi(r,t)\rangle = \sum_{i=1} c(t)|\Psi(r,t)\rangle \tag{1.18}$$

where c(t) exists in the groundstate and equal to one and that if integrated over infinity it will exist. The eigenvalues can then be calculated for a transition between two states when using the full Hamiltonian that includes the interaction with the electric field.

$$\langle m|[\hat{H}_o + A(t)] \sum_n c(t) e^{-iE_n t/\hbar}|n\rangle = \langle m|i\hbar \frac{\partial}{\partial t} \sum_n c_n(t) e^{-iE_n t/\hbar}|n\rangle \tag{1.19a}$$

$$= i\hbar e^{-iE_m t/\hbar} \frac{\partial c_m}{\partial t} \tag{1.19b}$$

$$\therefore \frac{d}{dt} = \frac{1}{i\hbar} \sum_n c_n(t) e^{-i(E_n - E_m)t/\hbar} \langle m|A(t)|n\rangle \tag{1.19c}$$

Solving for $c_m(t)$ one integrates from $-\infty$ to some time to get equation 1.20.

$$c_m(t) = \frac{1}{i\hbar} \int_{-\infty}^{t} e^{-i(E_n - E_m)t} \langle m|A(t)|n\rangle \, dt \tag{1.20}$$

where $\langle m|A(t)|n\rangle$ cannot equal zero for a single electron to be allowed. The instantaneous dipole ($A(t) = \mu \cdot E$) is the first nonzero interaction that results in an allowed transition.

1.3.2 Circular polarized spectroscopy

Under a circularly polarized electric field, the wave function needs to be adjusted to contain nonzero off diagonal terms to the transverse wave propagation.
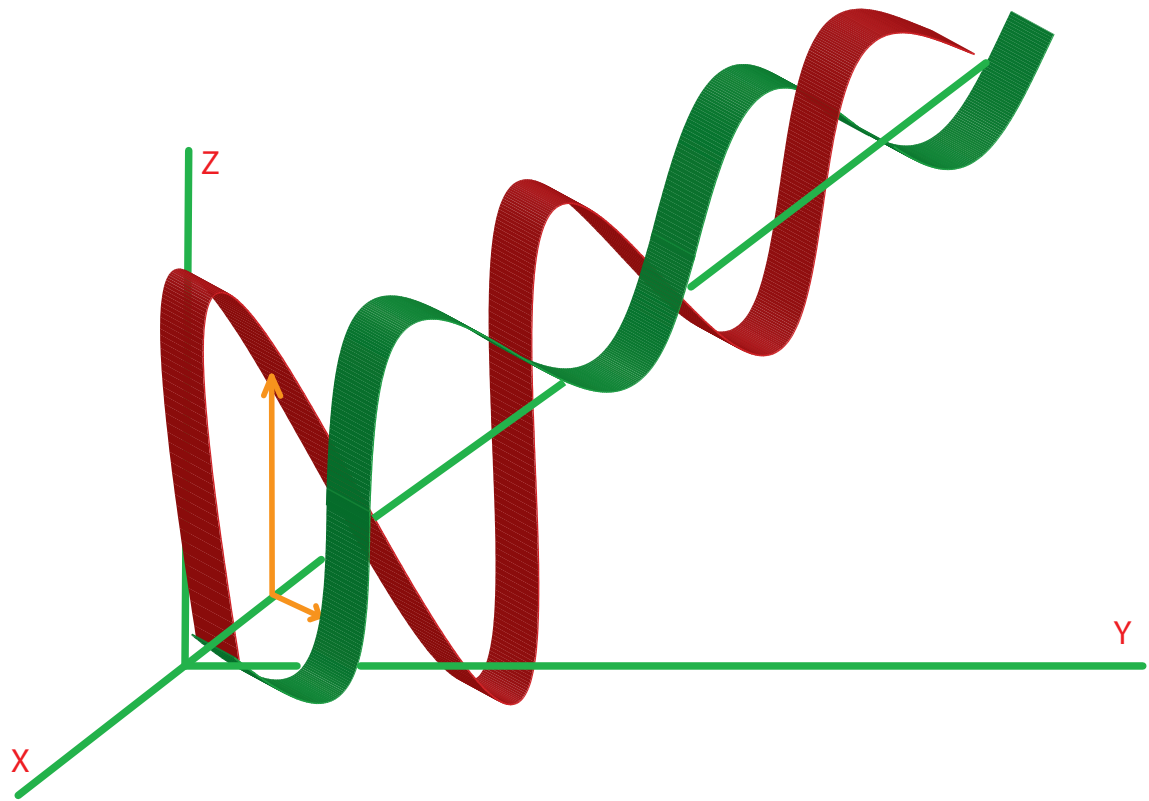
Figure 1.4: Linear polarized light that includes the electric and orthogonal magnetic component.

The two components of the field take the form for the wavefunction

$$\Psi_x = E_x = A_1 e^{i(\varphi)} \tag{1.21a}$$

$$\Psi_y = E_y = A_2 e^{i(\varphi+\delta)} \tag{1.21b}$$

and when passed through a linear polarizer the electric field remains unchanged in one direction. The use of Jones matrix for the polarizer shows the electric field having one transverse component.

$$\begin{bmatrix} E_x \\ E_y \end{bmatrix} = \begin{bmatrix} P_{11} & P_{12} \\ P_{21} & P_{22} \end{bmatrix} \begin{bmatrix} E_x \\ E_y \end{bmatrix} \tag{1.22}$$

For a linear polarizer the Jones matrix becomes

$$\begin{bmatrix} 1 & 0 \\ 0 & 0 \end{bmatrix} \tag{1.23}$$

where only one of the components of the electric field propagates through the polarizer. To circularly polarize the light a quarter-wave plate is added after the linear polarizer. The differences in the in-plane and out of plane index of refraction of the quarter waveplate creates a phase delay $(\eta_1\text{-}\eta_2)$ between the different components of the electric field. The total Jones matrix for the quarter-wave plate is

$$QW = e^{i\varphi} \begin{bmatrix} i & 0 \\ 0 & -i \end{bmatrix} \tag{1.24}$$

where a delay is created of $\pi/2$. The electric field under circular polarized light transforms (Fig.1.5) into

$$\begin{bmatrix} E_x \\ E_y \end{bmatrix} = \begin{bmatrix} Cos\theta & -Sin\theta \\ Sin\theta & Cos\theta \end{bmatrix} \begin{bmatrix} Cos\psi \\ iSin\psi \end{bmatrix} \tag{1.25}$$

where the transformation of the Jones matrix to the right and left circularly polarized field.

$$\frac{1}{\sqrt{2}} \begin{bmatrix} 1 \\ -i \end{bmatrix} \tag{1.26a}$$

$$\frac{1}{\sqrt{2}} \begin{bmatrix} 1 \\ i \end{bmatrix} \tag{1.26b}$$

where the linearly polarized field passed through a quarter wave plate transforms the field into the right and left circular polarizations, respectively.

16
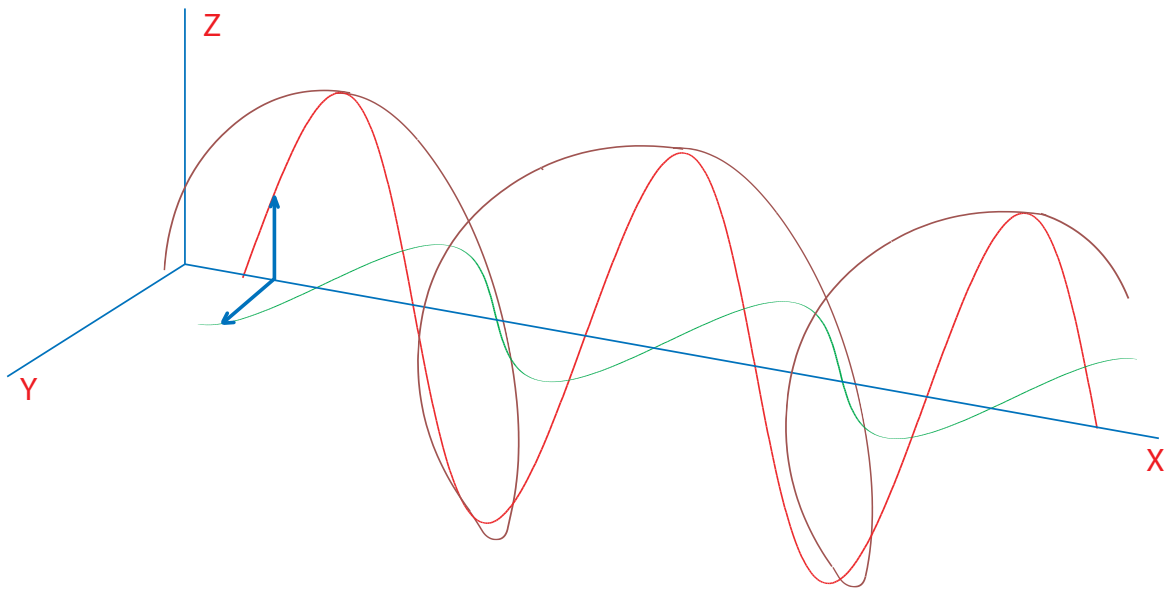
Figure 1.5: Circular polarized light that includes the electric and orthogonal magnetic component with the complex addition of both fields.

The electric field under left and right circularly polarized conditions has the form

$$E_+ = \frac{1}{\sqrt{2}} \begin{pmatrix} 1 \\ -i \end{pmatrix} e^{-i\omega(t-n_+ z/c)} \tag{1.27a}$$

$$E_- = \frac{1}{\sqrt{2}} \begin{pmatrix} 1 \\ i \end{pmatrix} e^{-i\omega(t-n_- z/c)} \tag{1.27b}$$

where the electric field is dependent on the complex refractive index (n) and the only direction that is important is the z-axis of the field. Because of the angular rotation of the field the magnetic component of the electromagnetic field that needs to be added.

$$H_+ = (n/\mu)E_0 \begin{pmatrix} 1 \\ -i \end{pmatrix} e^{-i\omega(t-n_+ z/c)} \tag{1.28a}$$

$$H_- = (n/\mu)E_0 \begin{pmatrix} 1 \\ i \end{pmatrix} e^{-i\omega(t-n_- z/c)} \tag{1.28b}$$

where the addition μ of the complex magnetic permeability gets added. The magnetic permeability is related to the magnetic susceptibility by the following equation $\mu = 1 + \frac{M}{H} = 1 + \chi$. The intensity will have both the refractive index and magnetic susceptibility inherent in the data. This gives rise to a energy level that is dependent on the angular momentum. By using this knowledge along with the single electron transitions one can make the prediction of the Zeeman splitting and the types of transition that become allowed under these conditions. For an interaction to occur between the circular polarized light and an electronic state, the state needs to contain a nonzero angular momentum. As observed in figure 1.6, circular polarized light separates the different spin orientations. This allows one the ability to determine information about the types of states involved in the electronic transitions.

1.3.3 Magnetic circular dichroism

In the interaction between an electric field and the electric dipole moment of a system, a spontaneous dipole is formed $< m|\mu \cdot E|n >$ where m is the ground state and n is the excited state, following the selection rules for a single photon allowed transition. The magnetic field interaction to the dipole adds the complex magnetic permeability. In addition under the magnetic field the states split following the electric $< m|\mu|n > \neq 0$ and magnetic dipole $(< m|\mathbf{L}|n > \neq 0)$ transition selection rules predicting transitions that follow $\Delta M_L = \pm 1$.
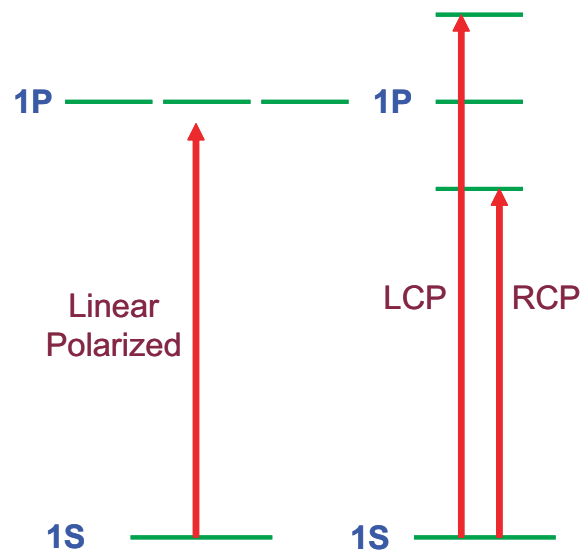
Figure 1.6: The allowed transitions under circular polarized light include only those states that contain a nonZero angular momentum.

The use of circular polarized electric field probes ΔM_L=+1 and ΔM_L=-1 independently where the difference in energy between the two transitions is equal to the Zeeman splitting (MCD A-term). As long as the splitting is greater than the linewidth, the transitions are resolved. As observed in figure 1.7 the spectrum obtained is a differential function of the difference between the polarization. The energy difference between right and left circularly polarized light is the Zeeman splitting. The Zeeman splitting is not dependent on temperature as long as the splittings $\ll k_B T$, but when they are on the same order there will be a dependence following a Boltzmann distribution

$$N_a = N \frac{e^{-\hbar \omega_q H / k_B T}}{\sum_q e^{-\hbar \omega_q H / k_B T}} \tag{1.29}$$

where N is the electron density per volume, ω_q is the splitting energy at the field H applied. This is especially true when spin orbit coupling (MCD B-term) is present, requiring an adjustment be made to the magnetic dipole to include the orbital contribution to the transitions ($< a|\mathbf{J}|b > \neq 0$). The mixing of states as a result of the orbital contribution induces changes in the population of each of the transition states as observed in figure 1.8. The ground state has a higher probability of being populated at lower temperature when the population of the state is dependent on the Boltzmann distribution (eqn 1.29). This causes a change in the population of each of the states where there is a ΔI increase in the intensity of the new split ground state and decrease in the higher energy ground state. When the the system contains a paramagnetic moment, the ground state population increases as 1/T (C-term) as observed in the MCD intensities.

1.3.4 Photoluminescence

In a molecule we can describe the absorption and re-emission of energy in a simple two- state picture. Recombination in semiconductors is more than a simple picture of two energy levels relaxing into the groundstate. As good guides the band diagram shows the allowed transition that occur typically with little interactions present from the lattice and defect sites. Many observables can exist of induced properties typically not intrinsic to the semiconductor. For this the power density is typically kept to one photon available per absorption event. As in absorbance the same selection rules apply which involve $\Delta m = \pm 1$ transitions.
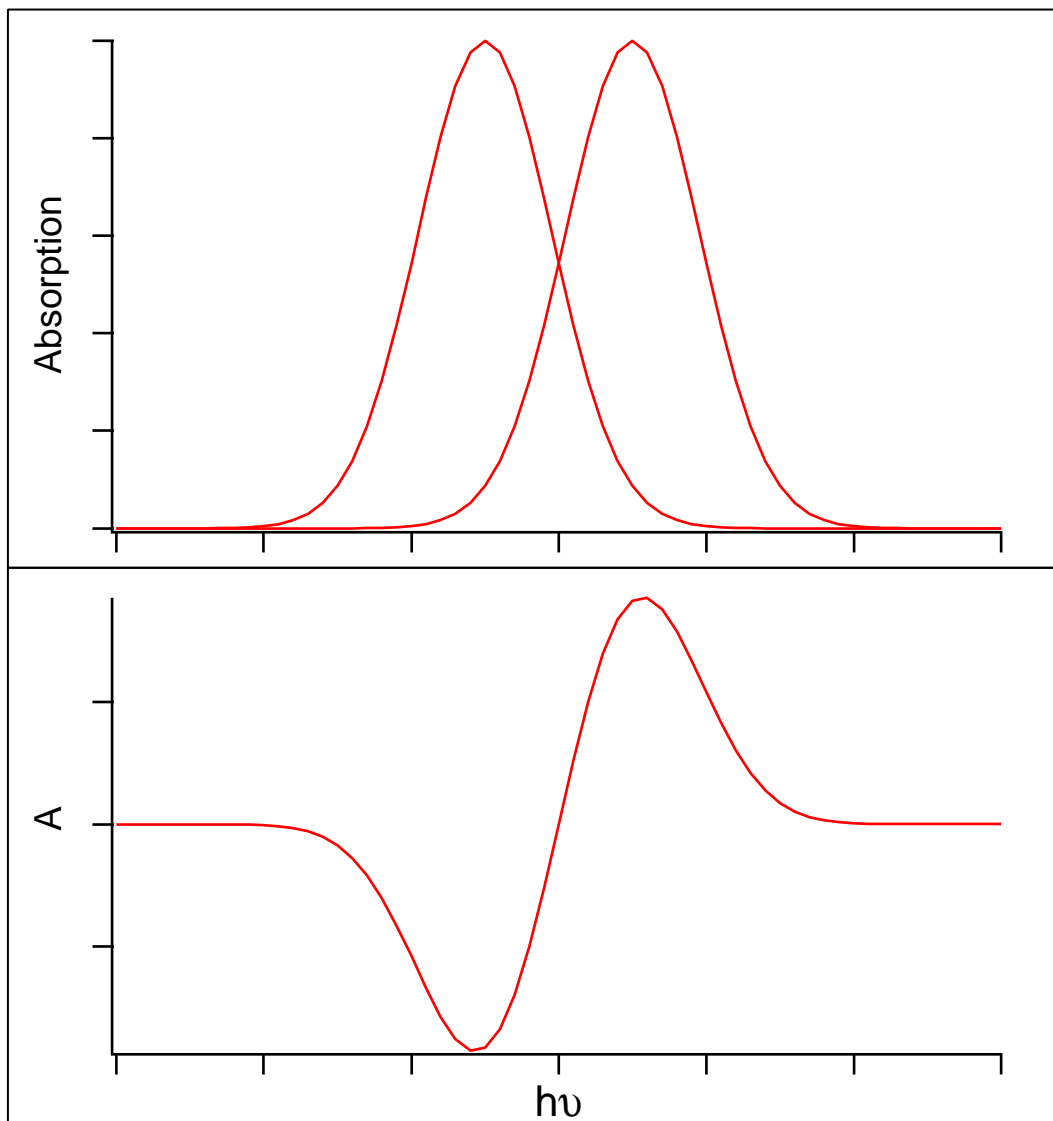
Figure 1.7: The expected absorption transitions and compilation of the two right and left circular polarized components.
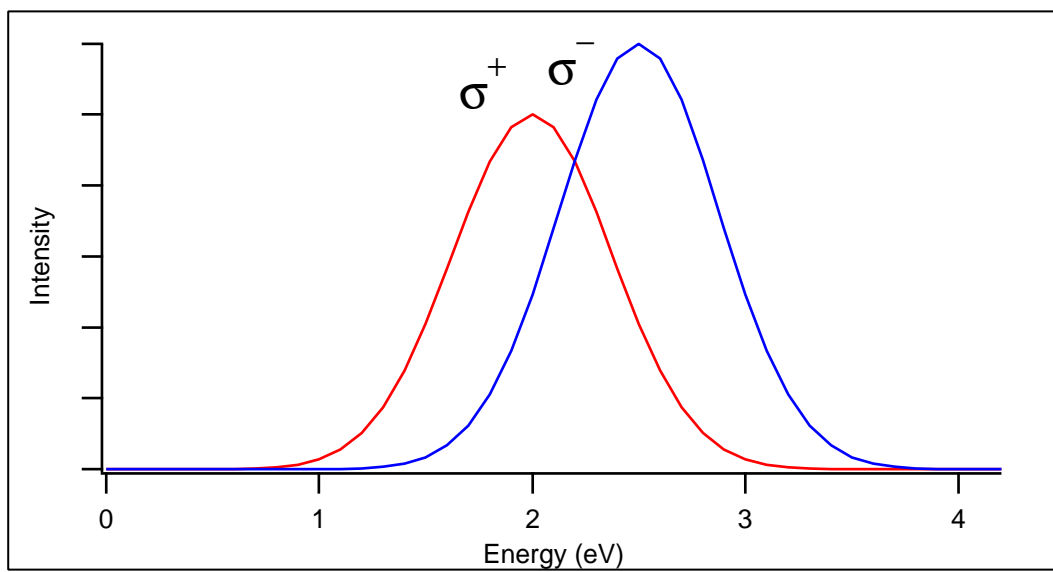
Figure 1.8: Intensity change in the right and left circular polarized intensity as a result of spin orbit coupling.

The transition between states of different quantum numbers are the primary observed transitions, while transitions that require a spin flip are only 1/3 allowed. To a first approximation these selection rules are followed to give rise to all of the main allowed transitions present in an intrinsic semiconductor. If phonons are included, through an electron phonon process, mixing can occur, where the effect is an observed emissive state that contains vibrational overtones in the photoluminescence. The frequency of the overtone is identical to the modes observed in resonance raman. Once phonons are involved in the absorption and relaxation to the emitting state an inexhaustible set of interactions can give rise to emission or lack of emission. The electron-phonon interaction can become one of the most important interactions that leads to an apparent bandgap change (photoluminescence emission) as a function of temperature due to population of nearby states, thus a distribution of emitting states is observable. To begin in a more or less ordered explanation we will take a perfect semiconductor and lower symmetry to show the observed properties.

The first dipole allowed transitions in our wurtzite CdSe case are the Γ^7 to Γ^9 (E_1) and Γ^7 to Γ^7 ($E_1 + \Delta$) where the primary transition is the E_1 resulting from the change in quantum number (Figure 1.9). The Delta represents the spin orbit term for a wurtzite semiconductor. To a first approximation the only expected transition is the E_1 if no thermal contribution influence state population. If the energy of separation of E_1 and $E_1 + \Delta$ is $< k_B T$, then $E_1 + \Delta$ may be observed.

It is easy to predict a lowered symmetry at the surface due to the surface atoms bound to say hydrogen or a ligand. The crystal field about the surface atoms is also going to be different due to changes in bonding and electron distribution. We can lower the symmetry of the surface and say its going to propagate the lowering of symmetry into the internal part of the particle. In a sense, this is an effective reconstruction of the core by the surface. For small nanocrystals where the surface to volume ratio is large, this is not unlikely and in fact has been observed in solid state NMR experiments[39]. We bring back the C_{6v}^4 irreducible representation (1.2) and take the valence band and conduction band symmetry levels to reduce symmetry of these states. We are only concerned with the $E_{3/2}$ and $E_{1/2}$ symmetry. The intention is to lower the symmetry to a C_{3v} which means that we can use the C_3 rotation and σ_v mirror plane. The result is the same character values of $E_{3/2}$ and $E_{1/2}$ where $E_{3/2}$ is a complex conjugate.
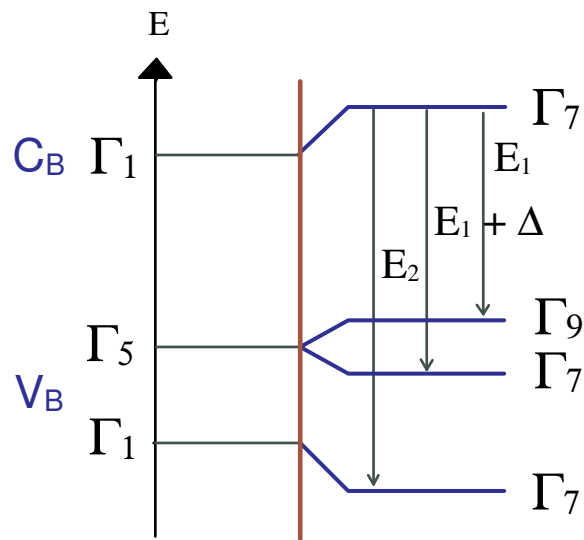
Figure 1.9: Schematic of the allowed optical transitions of a wurtzite crystal structure.

The exciton formation results from the cross product of these states where a quadruplely degenerate E+E state is produced. The reduction still gives rise to the same allowed states.

1.4   Magnetic ion incorporation

To achieve the set of magneto- optical experiments two setups were necessary, one for MCD (Fig. 1.10) and the second for MPL (Fig. 1.11). The MCD set up is a typical Faraday geometry excitation described in figure 1.10 where the circular polarized light is obtained from a commercial Jasco circular dichroism system. The circular polarized light from the Jasco system changes from right to left circular polarized light using an AOM (acousto-optic modulator) crystal that changes the polarization. The light passes through the sample inside the magnet and detected using a PMT (photo-multiplier tube). The right and left circular polarized light gets separated into positive and negative values by using a lock-in amplifier connected to the AOM crystal. A typical spectrum is as observed in figure 1.7 where the differential function is the combination of right and left circular polarized absorption. The simple use of a Voigt function enables one to fit the data and determine the Zeeman splitting from the change in position. The C-term can be determined using the phase intensity as a function of field or temperature. The addition of a magnetic ion changes the dynamics of the groundstate. Depending on the exchange interactions between the magnetic ion and the valence band of the semiconductor one can see changes in the C-term of the MCD. The interaction between the Mn(II) and the valence band of CdSe is expected to show a temperature dependence and therefore a C-term.

MPl is set up in reflection mode where the use of fiber optics enables one to excite the samples inside of a resistive magnet. The configuration is as shown in figure 1.11 where an argon ion laser is used to excite the sample. The laser travels through the fiber optic and into the magnet. Before the light gets to the sample, the light is circularly polarized by the use of a polarizer and quarter wave plate in that order. The light excites the sample in a circular polarized manner and the light collected is only that of the same polarization. The photoluminescence is then detected using a meter monochromator that uses a 600 mm/groove grating blaze in the visible. The photoluminescence spectra is then fit to a Voigt function to accommodate for the Lorentzian vibrational line width and gaussian particle size distribution.
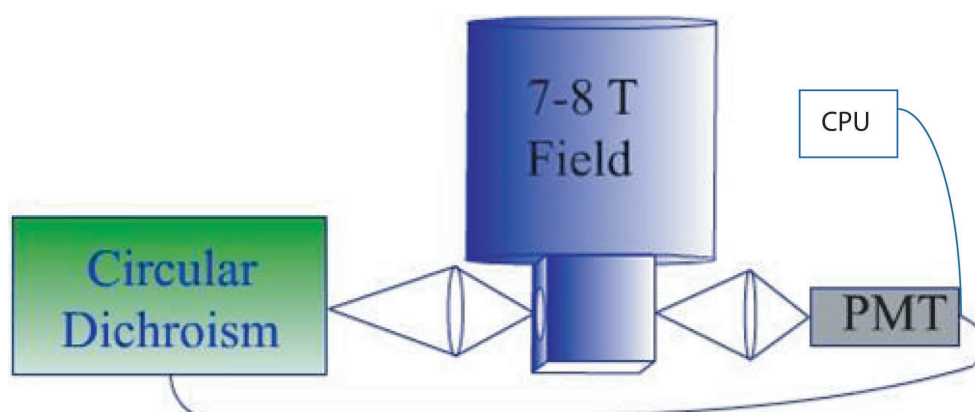
Figure 1.10: Diagram of the physical setup for the MCD.
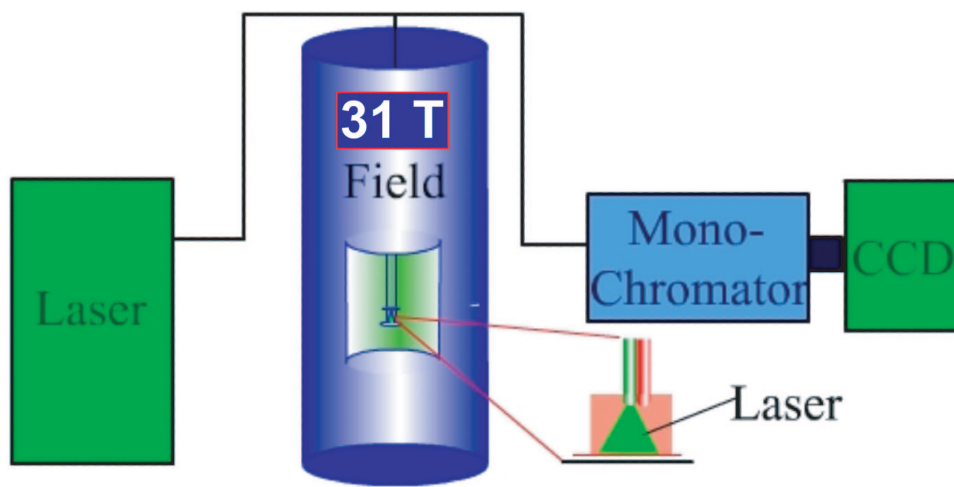
Figure 1.11: Diagram magneto-photoluminescence setup.

Both MCD and MPl techniques give information about the Zeeman splitting, g- value for the electron and hole, and as a function of temperature the phonon contribution. Mixing of states can be determined only if the states are optically allowed and have enough intensity to be detected. Properties like scattering due to impurities can be detected by the MCD if the impurity affects the formation of the exciton. In photoluminescence the presence of impurity ions can decrease the radiative pathways inhibiting the radiative pathways. Better physical techniques can detect the effect of impurities on the host lattice such as magnetization and heat capacity studies.

1.4.1 Heat capacity

The heat capacity is composed of vibrational, electronic and magnetic contributions. The presence of carriers can be detected by heat capacity measurements. To explain how the carriers are measured by heat capacity, development of the model is important. At a threshold temperature the thermally excited vibrations become significant in the lattice. Inter-atomic interactions (force constant) drive the energy of the the vibrations. In a classical sense, the number of vibrations are describable in terms of a temperature. In the nanoscale, the limited size should be observed in the frequency of the wave that can fit the size of the semiconductor.

As expected for a simple Hooke's law approximation, the Debye model is used to predict the heat capacity for a condensed phase material. The three dimensional wavevector used is

$$q = \left(\frac{(2\pi)^3}{V} \right) n \tag{1.30}$$

where V is the system volume and n is a mode integer. The number of modes can then be determined as a differential of n

$$d^3 q = \left(\frac{V}{(2\pi)^3} \right) d^3 n \tag{1.31a}$$

$$d^3 n = \left(\frac{V}{(2\pi)^3} \right) d^3 q \tag{1.31b}$$

$$= \left(\frac{4\pi V}{(2\pi)^3} \right) q^2 dq \tag{1.31c}$$

where equation 1.31c resembles that of an isotropic sample. The density of states for the three polarizations of energy between E and $E + dE$ needs the relationship between the

wavevector and momentum($\hbar = \frac{p}{q}$). The density then becomes

$$\rho(E)dE = 3\left(\frac{4\pi V}{(2\pi\hbar)^3}\right)p^2 dp \tag{1.32}$$

where $\hbar$ is Planck's constant and the three is for each of the polarizations for the single particle states. The density becomes

$$\rho(E) = \left(\frac{12\pi V}{(2\pi\hbar c)^3}\right)E^2 \tag{1.33}$$

where the density of phonons is adjusted by minimizing Helmholz free energy. For a Bose system the number of phonons in any state is

$$n(E) = \frac{1}{e^{E/k_B T} - 1} \tag{1.34}$$

where k_B is the Boltzmann constant. The thermal energy becomes

$$E_{thermal} = \int_0^{k_B \theta} E^2\, dE = 9Nk_B T\left(\frac{T}{\theta}\right)^3 \int_0^{\theta/T} \frac{x^3}{e^x - 1}\, dx \tag{1.35}$$

where the limits are set to have no boundaries up to the maximum allowed by the lattice spacing. Using Helmholz free energy one can arrive at the heat capacity following

$$E = F + TS \tag{1.36a}$$

$$C_v = \left(\frac{\partial E}{\partial T}\right)_v \tag{1.36b}$$

$$C_v = 9Nk_B \left(\frac{T}{\theta}\right)^3 \int_0^{\theta/T} \frac{x^3}{e^x - 1}\, dx \tag{1.36c}$$

where the heat capacity goes to zero at zero Kelvin. To properly describe the heat capacity of semiconductors an offset from the Debye model is added as a result of carriers present.

Electrons obey Fermi-Dirac statistics and only at very low temperature can the electronic contribution to the heat capacity be observed. The magnitude of the lattice heat capacity overshadows the electronic component. Using the Pauli exclusion principe, the number of particles in the state ϵ is

$$N = \frac{g}{e^{\frac{\epsilon - \epsilon_f}{k_B T}} + 1} \tag{1.37}$$

where ϵ_f is the Fermi energy which limits the occupation of states, and g is the number of particles with energy ϵ. The Fermi-Dirac distribution then becomes

$$f(\epsilon) = \frac{1}{e^{\frac{\epsilon - \epsilon_f}{k_B T}} + 1} \tag{1.38}$$

29

which is used in the calculation of the density states. Equation 1.32 can be used to determine the number of allowed states

$$\eta(\epsilon)d\epsilon = (2m)^{3/2}\frac{(2\pi)^4}{\hbar^3}\epsilon^{1/2}d\epsilon \tag{1.39}$$

where m is the mass of an electron. All of the components to determine the energy of the carriers are ready. The energy is then calculated in the same manner as for the phonons

$$E_{electron} = 2V \int_0^\infty \epsilon f(\epsilon)\eta(\epsilon)\,d\epsilon \tag{1.40}$$

where the heat capacity can finally be derived using the same relations as for the lattice heat capacity

$$C_{electronic} = \frac{2}{3}\pi^2 k_B^2 V\eta(\epsilon_f)T \tag{1.41}$$

For a nonmagnetic sample the heat capacity is then composed of two components, a lattice component (βT^3) and an electronic component (γT). The lattice component (β) as observed in equation 1.36C which contains a T^3 dependence easily observed at high temperatures. The electronic component (γ) is only linearly dependent on temperature but can be observed at low temperature when the lattice component is on the same order as the electronic.

1.4.2 Magnetic exchange

Two main types of interactions can be present in the semiconductor, the localized superexchange interaction and the indirect exchange interaction. The approximation used involves the magnetic spin interactions to determine whether they exist parallel or antiparallel to each other. For this the exchange of interest is the interaction between the two spins

$$H_{ij} = J(R)S_i \cdot S_j \tag{1.42}$$

where J is the exchange interaction that is distance dependent. The exchange interaction is dependent on the susceptibility of the host material. As an approximation one electron is assumed to be present per unit cell[40]. The wavevector then becomes

$$k_f = \left(\frac{12\pi^2}{a^3}\right)^{1/3} \tag{1.43}$$

where a is the lattice constant. A free-electron approximation is then used to describe the exchange interaction[40]

$$J(R) = \frac{4A^2 m k_f^4}{2\pi^3\hbar^2}\frac{2k_f R cos(2k_f R) - sin(2k_f R)}{(2k_f R)^4} \tag{1.44}$$

where A is a normalization constant, m is the mass of an electron, and R is the distance between the Mn. Using the lattice constant for CdSe of 4.29 Å, the nearest neighbor Mn would be antiferromagnetic (negative) as shown in figure 1.12 as a negative value. It is not until the next nearest neighbors that ferromagnetic interactions are predicted. The delocalization of the carriers is rather important in the manifestation of observed superparamagnetism.

For II-VI and III-V semiconductors the main interaction is described by a RKKY type of interaction, where, depending on the material, carriers can play a role in the delocalization of the spin within the confined volume size. Superexchange interactions are much stronger than the indirect although in the nanoscale where domain formation is not favored there is a fine line in the exchange observed, where superexchange interactions in a diluted system approach that of the indirect exchange interactions. To explain the diluted superexchange interactions, RKKY is used to help explain the type of exchange present between spins using conduction electrons as intermediate spin polarizers.

The strength of the p-d exchange interaction between Mn ions is well known in semiconductors. One can apply a simple RKKY type of interaction and attain the first interaction to be antiferromangetic. The important components are the spins associated with the valence band (hole). This interaction is guided by the difference in energy between both the magnetic ion and the valence band. This hybridization is changed by the presence of carriers which fine tune the Fermi energy and therefore exhibit an overall change in the overlap energy. This is only speculation until one observes ferromagnetism for a system that is expected to have a very strong antiferromagnetic interaction. It is hard to judge the magnitude of exchange that occurs upon addition of carriers specially if we don't know the energy difference between the two. In addition at the nanoscale the bands shift energy as a result of the hard walls of the nanoparticle and, if significant, the exchange integral must change. The expected p-d exchange for bulk MnCdSe is -1.11 eV where more covalent systems like MnCdTe have a p-d exchange of -0.88 eV and ionic semiconductors such as MnCdS the exchange increases to -1.80 eV [41].

1.4.3   Dilute magnetic semiconductors

Dilute magnetic semiconductors have been created in bulk semiconductors for nearly three decades with systems such as Mn doped CdS[7], CdSe[7], CdTe, HgS, and many others.
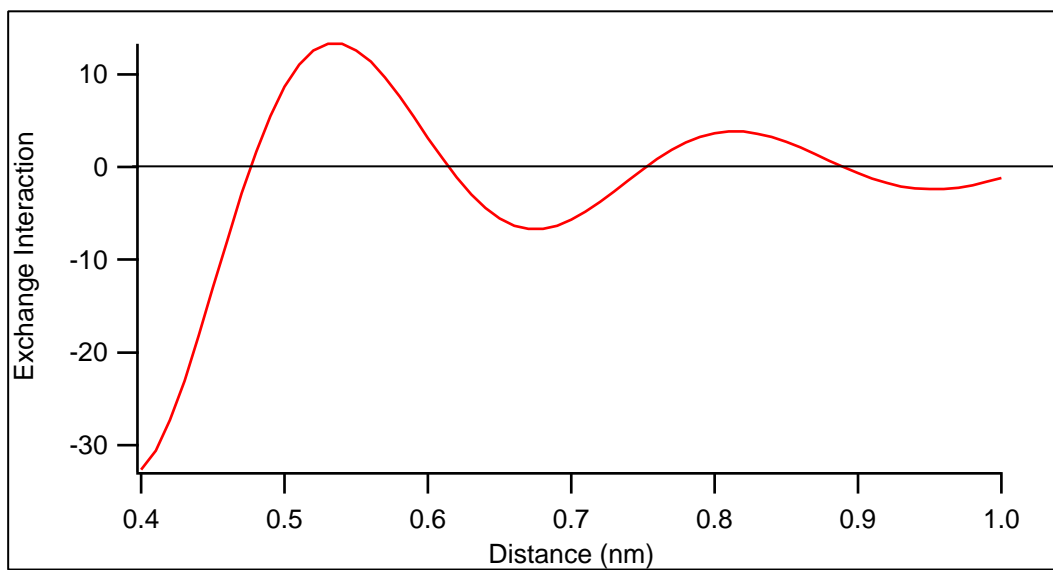
Figure 1.12: Plot of the exchange interaction with respect to the distance from the central Manganese.

Carriers have been observed to play an important role in the exchange interactions that drive the properties of DMS. These materials have been limited to weak ferromagnetic and antiferromagnetic interactions.

When the free carriers are taken into account in the interaction as an ensemble, the exchange interaction of interest is as follows

$$J \sum_{i,I} S_I \cdot h_i^+ \delta(r_i - R_I) \tag{1.45}$$

where the interaction of interest is the p-d interaction that determines the magnitude of the exchange, observed as a change in the Curie temperature. The interplay between the carriers and concentration determines the Curie temperature. Following a mean-field approximation[42]

$$T_c = \frac{[Mn]S(S+1)}{3k_B} \frac{J_{pd}^2}{(g^*\mu_B)^2} \frac{3N(\frac{g\mu_B}{2})^2}{2(\frac{\hbar^2}{2m}(3\pi^2 N)^{2/3})} \tag{1.46}$$

where $[Mn]$ is the molar concentration of the dopant with spin S, J_{pd} the bulk p-d exchange interaction (-1.1 eV) [43], g^*, the carrier g factor (1.6) [43], g is the Mn g factor (g = 2), m the effective hole mass of CdSe lattice, and N the hole concentration. For this to work a significant number of carriers need to be present (Fig. 1.13). CdSe in the bulk would be an unlikely candidate for this theory to be applicable since it contains 10^{18} carriers per cm^3. The observable Tc doesn't begin until one achieves a carrier density of $>10^{19}$ (figure 1.13). A solution would be to significantly increase the concentration of the dopant ion, but many difficulties occur such as phase segregation and clustering that becomes prevalent as the concentration increases as a result of the poisson cluster statistics as shown in figure 1.14. The statistics can be calculated depending on the lattice atomic density where the probability for the formation of a pair of ions increases with increasing concentration. This can be analyzed by using eqn 2.1

$$P_1 = (1 - 12x)^{12} \tag{1.47a}$$

$$P_2 = 12x(1 - x)^{18} \tag{1.47b}$$

$$P_{3OT} = 18x^2(1 - x)^{23}(7 - 5x) \tag{1.47c}$$

33
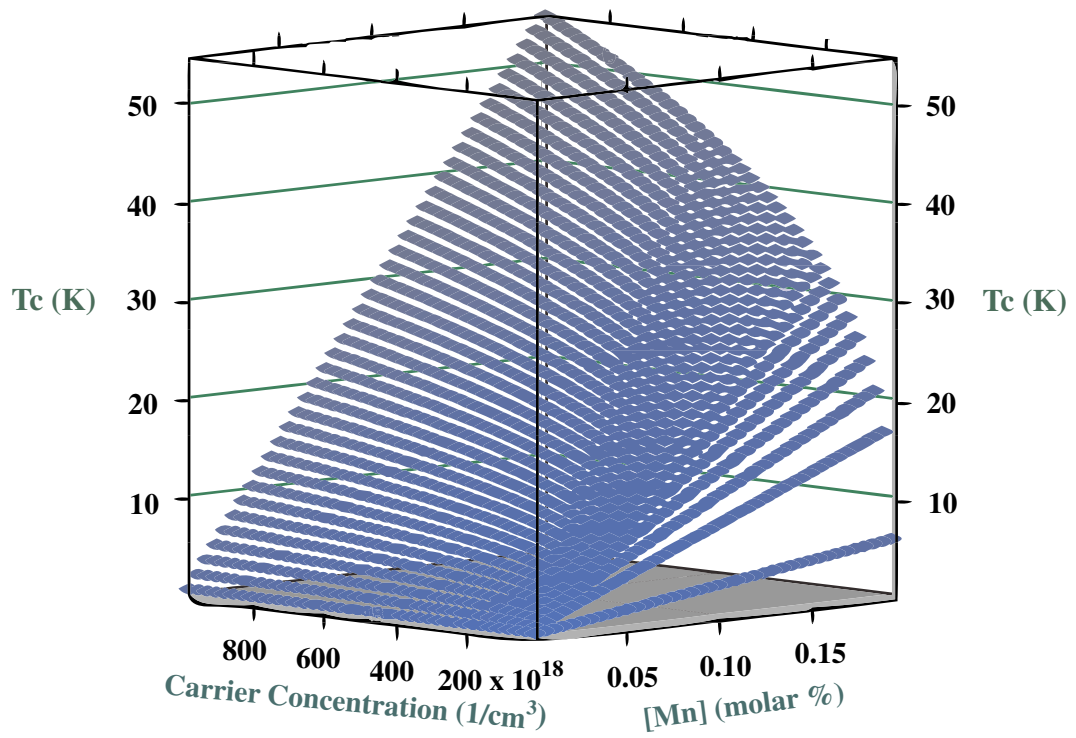
Figure 1.13: 3DPlot of the Tc for MnCdSe as a function Mn and carrier concentration.
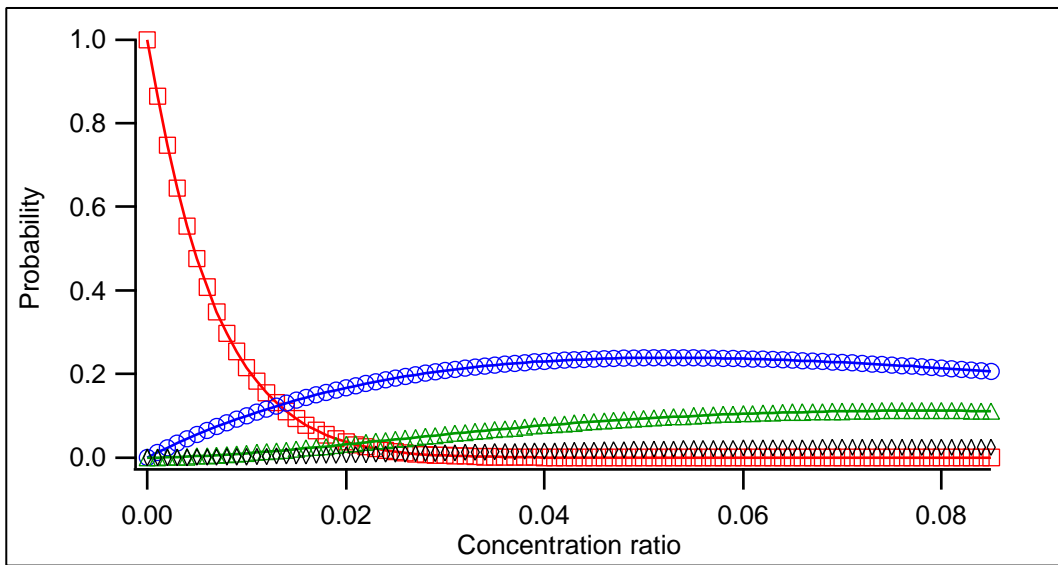
Figure 1.14: Poisson statistics for clustering of ions in a hexagonal lattice. The probability for single ions (O), pairs (□), open triangles (△), and closed triangles (◇).

$$P_{3CT} = 24x^2(1-x)^{22} \qquad (1.47d)$$

where the probability for single ions (P_1) is greatest at low concentrations. As the concentration increases the formation of pairs (P_2), open triangles (P_3), and closed triangles (P_3) increases respectively.

Knowledge about carrier concentrations is critical in the analysis and interpretation of carrier induced magnetism. The origin of carriers can result from intrinsic vacancies and impurities. Vacancies are expected to be present in a nanoparticle because of how fast the particles grow. Cadmium vacancies result in an acceptor state that is 0.6 eV above the valence band[44]. This acceptor state can result in carriers where the concentration of vacancies determines the carrier concentration. It is unfortunately difficult to determine the single particle carrier concentration, which has limited the ability to accurately determine the intrinsic carrier concentration.

In analogy to color-centers in Quartz, a neutral vacancy can be considered as an isoelectronic impurity if it localizes electrons resulting in lattice charge compensation which delocalizes electron (donor) or holes (acceptors)[45]. To identify this acceptor level is difficult in that the optical processes are in the infrared. The only successful detection has been of donor states when induced by surface reduction[46]. The impurity induced carrier origin is the more quantitative since it can be controlled by the addition of an impurity. Special attention is to isoelectronic impurities that have a much higher binding energy, which results in the same effect as vacancies. Based on the electronegativity for CdSe would suggest that oxygen impurities give rise to impurity states more easily than sulfur. A study on a set of CdSe single crystals[47], Cd-annealed crystals showed little photoluminescence due to the nonradiative recombinations from the acceptor states induced from the excess Cd. The surface atoms must form different energy states than the core as a result of the bonding to ligands and therefore produce states that do not contribute to the band formations. The surface states show up as intra-gap transitions. In a study of nanocrystalline layers through the use of photoconductivity and thermally stimulated current measuremets, it was found that CdSe contains holes from an acceptor state at $\backsim$ 0.6 eV[48] consistent with a cadmium vacancy which produces a vacancy at 0.6 eV[44] above the valence band leading to the conclusion that CdSe has significantly more holes than electrons. The most likely origin of

such carriers can be reasoned to be induced by the surface.

1.5 Quantum confinement effect on the properties

If we were to begin to describe nanoscale materials the assumption of an infinite lattices begins to break down and the influence of surface states, reconstruction and vacancies become critical in understanding the physics of these materials. For a spherically confined system, the periodicity of the lattice can breakdown due to reconstruction, particularly in materials < 3 nm where the surface to volume ratio is large (Fig. 1.15). This will be an important finding to the properties observed. To realize the effect it is worthwhile to project the periodic problem first.

The challenge and interest lies in materials that have a short periodicity of the lattice where the surface potential is dependent on the type of material, ligand type, and crystal structure, as observed in a quantum dot. In a simplistic square potential there is a change that introduces an uncertainty in the periodicity producing changes to the energy of the system projected as an energy dispersion. The limitations lie in the uncertainty principle where the periodic lattice is limited by the size of the material. This results in a deformation potential that induces an increase in the electron-phonon coupling with decreasing size (Figure 1.16).

1.5.1 Size effect on optical properties

In semiconductors a special interest arises when the size of the semiconductor approaches the electron-hole distance (Bohr radius). Classically, the exciton is treated as a particle in a box (hydrogen model). As in the hydrogen model the energy is dependent on the effective mass of the electron and hole, the Coulombic interaction between the electron- hole and the size of the particle. When the size of the semiconductor approaches the size of the exciton, the energy becomes size dependent. For a spherical system the energy (E_n) can be expressed as $E_n = \frac{\hbar^2 \pi^2 n^2}{2mR^2}$[19] where n is the quantum number, m is the effective mass and R is the size of the sphere. The size dependent gap then becomes

$$E_n = \frac{\hbar^2 \pi^2 n^2}{2R^2} \left[\frac{1}{m_e} + \frac{1}{m_h} \right] - \frac{1.8 e^2}{\epsilon R} \tag{1.48}$$
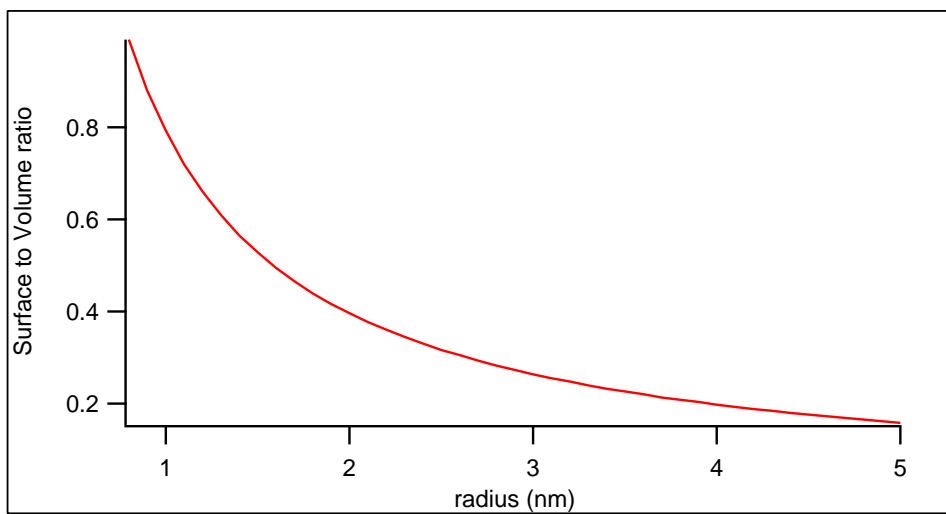
Figure 1.15: Surface to volume ratio for CdSe assuming a covalent radii of 1.48 $\mathring{A}$ for the Cd and 1.16 $\mathring{A}$ for Se.
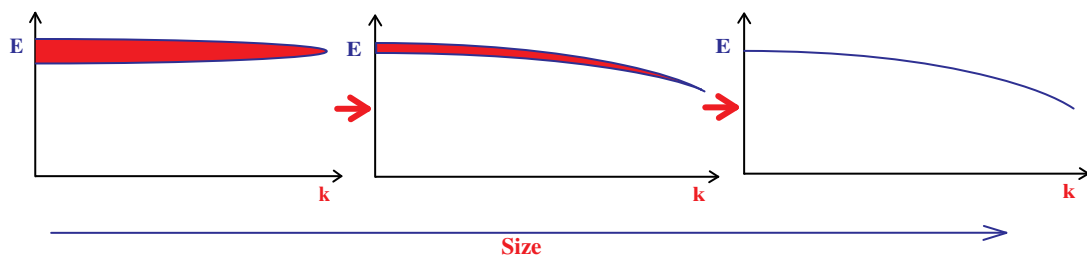
Figure 1.16: Energy dispersion evolution as the size of the nanomaterials increase in size.

, where n is the quantum number, R is the size of the semiconductor, m_e is the mass of the electron, m_h is the mass of the hole, e is the Coulombic charge of an electron, and ϵ is the dielectric constant. At small sizes (< 3 nm) a repulsive Coulombic interaction is added to offset the strong electron hole interaction. To see the effect of the size in CdSe the bulk effective electron (0.13) and hole mass (0.45) along with the dielectric constant of 6.1 can be used to plot the quantum confined bandgap as shown in figure 1.17 assuming a bulk band gap energy of 1.74 eV. This is for a system that contains no vacancies or defect ions. As a function of size the quantum dot will begin to delocalize the hole and approach the natural hole mass. For a system that contains vacancies or dopant ions a more reliable model is the localized exciton where phonons play a role in the recombination.

1.5.2 Size effect on the magnetic properties

The magnetic interaction in dilute magnetic semiconductors have been of great interest for the last decade for the use in spintronics. The detailed balance in the interactions of DMS are of great interest for the complexity of the environment that induce a magnetism not observed in the bulk[5, 7]. At the nanoscale single domain magnetism (superparamagnetism) is more easily observed as a result of the lack of domain formation. Domain formation results from the minimization of entropy arising from the surface magneto-static energy. When the size of the system decreases to a few nanometers the domain wall formation cannot be supported as a result of the large anisotropy energy. Simply put it is of lower energy to align all of the spins in one direction changing the internal energy and complicating the interactions. As a single domain, the uniform magnetization is expected to fit a Brillouin function and therefore a spin. As the interactions are diluted as in a semiconductor or as the size is decreased the superparamagnetic phase can be observed where the thermal fluctuations make the remanence go to zero. The region between the superparamagnet and the multi domain systems is of great interest. This is the region of anomalous behavior making this field a great curiosity.
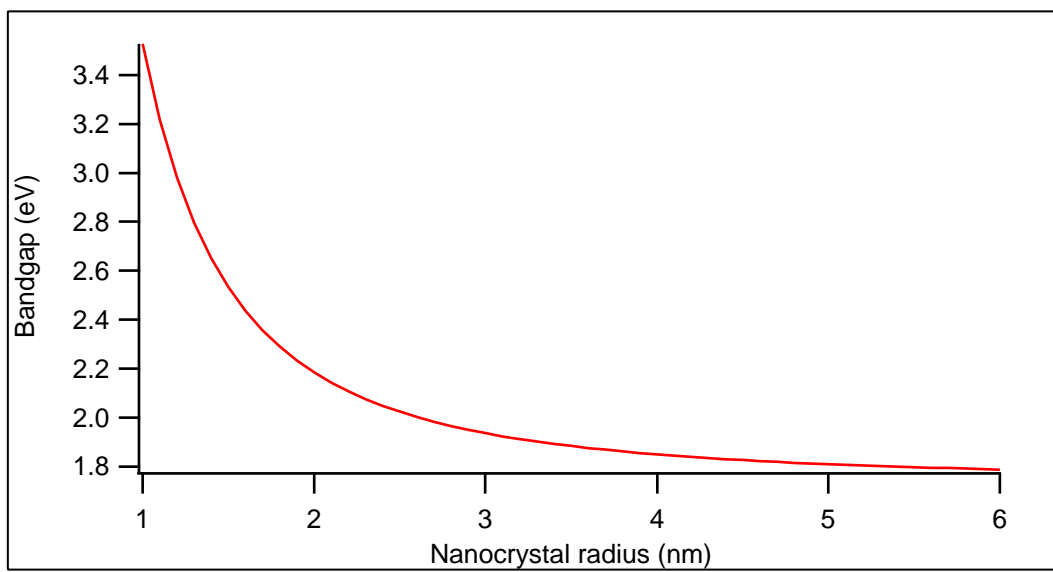
Figure 1.17: Theoretical prediction of the band gap of CdSe using eqn 1.48 as a function of size.

CHAPTER 2

1% Mn:CdSe

Mn ion doping of CdSe and other semi-magnetic quantum dot alloys has been an area of active speculation for over a decade. We report evidence of Mn(II) doping of CdSe grown from a cubic single source precursor that is superparamagnetic (SPM) with a blocking temperature of 40 K following thermal annealing. Prior to thermal annealing the 4 nm Mn:CdSe (1 % Mn) QDs exhibit paramagnetic behavior between 300 K and 2 K, with a weak antiferromagnetic exchange. Following thermal annealing of the sample, high temperature ferromagnetic exchange is observed in the magnetization data with the onset of a superparamagnetic phase (SPM) at 40 K that exhibits a coercivity of 0.1 T at 2 K. The switching-on of SPM behavior is believed to be linked to ion migration with formation of $(Se-Mn-Se-Mn-Se-Mn)_n$ centers within the nanocrystal that exhibit coupled magnetic moments. Electron Paramagnetic Resonance (EPR) provides evidence of two distorted T_d Mn core sites, a clustered site (dipolar broadened) and a localized Mn site (hyperfine-split). The ratio of the EPR signature for the dipolar broadened site increases following annealing and shows a hysteretic response around the blocking temperature. These observations suggest that thermal annealing results in enhanced cluster formation explaining the onset of the SPM phase in these nano-scale materials. Evidence of SPM behavior is evident in the field-dependent non-Langevin magnetization with a tangential loss in the magnetic ac-susceptibility, and the Mydosh parameter ($\varphi = 0.16$).

2.0.3   1% Mn:CdSe Introduction

Quantum confined magnetic materials with predictable size dependent properties, including ion-doped semi-magnetic semiconductors and molecular magnets, are one of the holy grails for spin-related applications at the nanoscale.[49, 22, 50, 7, 27] While ferromagnetism has

been observed for bulk Mn doped CdSe semi-magnetic semiconductors, the reason for the observation remains an area of speculation and is attributed to ion clustering within the lattice.[7, 20] Efforts on nanocrystalline Mn doped II-VI semi-magnetic quantum dots have also produced conflicting findings in their magnetic characterization depending on the nature of preparation and type of quantum dot.[22, 27, 25, 20, 51] While it was generally accepted that the conflicting results arose from lack of ion doping due to self-annealing leading to loss of the Mn ions for wurtzite CdSe,[22] in a recent paper by Efros et al. Mn doping was attributed to thermodynamic limitations for Mn ions to add to the growing faces of the wurtzite structure of CdSe.[20] The magnitude of ferromagnetic exchange in ion doped semi-magnetic semiconductor quantum dots will be dependent on the clustering of ions, the size of the cluster, the site occupation of the ion, the size of the quantum dot, and changes in the nature of the bonding in the host lattice in quantum confined materials.

This manuscript discusses the emergence of ferromagnetic exchange in 4 nm 1% Mn:CdSe nanocrytals with a wurtzite crystal lattice. Mn(II) ion doping is achieved using a single source precursor route based on a cubic cluster which seeds the growth of the Mn:CdSe quantum dots. These semi-magnetic quantum dots transform into wurtzite lattices as the particle grows, leaving the Mn incorporated in the lattice.[20, 52, 24, 53, 28] Intriguingly, upon thermal annealing of the Mn:CdSe quantum dot, a magnetic transition temperature is observed with a coercive field. The SPM behavior arises from enhanced ferromagnetic exchange between Mn ions clustered in the dimensionally confined lattice. Thermally-driven clustering of Mn into larger domains in the CdSe host lattice is believed to give rise to the observed SPM phenomenon. Magnetic susceptibility, magnetization studies, and EPR measurements confirm that the magnetic effects can be explained in terms of a doubling of the Mn cluster domain content. The presence of an exchange interation ($J_{ij}\vec{S}_i \cdot \vec{S}_j$) between two magnetic spins($\vec{S}_i, \vec{S}_j$) is evidence of the clustering of Mn(II) ions. The exchange interaction is evident in the magnetic susceptibility as a deviation from the Curie law, in which the Curie-Weiss constant is necessary to fit the beginning of the magnetic phase. The Curie temperature is proportional to the exchange interaction present in the system ($T_c = \frac{J_{ij}s(s+1)}{3k_B}$)[35], where J_{ij} is the exchange energy, s the spin of the interacting ion, and k_B is the Boltzmann's constant. No evidence for loss of Mn(II) or change in nanoparticle size is observed following chemical treatment, suggesting the ion clusters exist within the nanoparticle, although the exact location within the quantum dot is not discernable.

In doped nanomaterials[24, 23, 54, 26] the influence of clustering in chemically prepared systems has been speculated to influence the magnetic behavior in Co:CdSe nanoparticles at high concentrations of Co (>20%).[24] Thermally driven ion clustering in bulk materials is a known phenomenon that tailors the formation of magnetic, structural, and electronic domains.[17, 55, 54] Mullin and co-workers have observed ion migration effects for a series of single crystal Mn:HgSe samples.[13] Mullin observed changes in magnetism following thermal annealing (230 °C) of samples with <1 % Mn which he correlated with the change in cluster content following thermal annealing. This was also observed by Galazka[10] and Oseroff[11] where the amount of clustering was twice that predicted for the working concentration. This is also evident from the EPR and magnetic susceptibility in other systems such as Mn:CdS where the manganese interactions are evident from the dipolar (electron-electron) broadened EPR data[56, 51] and a magnetic susceptibility that includes clusters was added to fit the observations.[13, 10, 11] Using clustering statistics to predict the probability of finding different sized cluster domains within the lattice, the onset of magnetism was related to the concentration of 2 or more localized Mn clusters in the lattice. The probability for observation of clusters in a wurtzite lattice is

$$P_1 = (1 - 12x)^{12} \tag{2.1a}$$

$$P_2 = 12x(1 - x)^{18} \tag{2.1b}$$

$$P_{3OT} = 18x^2(1 - x)^{23}(7 - 5x) \tag{2.1c}$$

$$P_{3CT} = 24x^2(1 - x)^{22} \tag{2.1d}$$

where x is the dopant molar ion concentration for a substitutional ion and three ions can be along the same plane (P_{3CT}) or different crystallographic planes (P_{3OT}).[13] This predicts for x = 0.01, P_1 = 89% for isolated Mn ions, P_2 = 10% for ion pairs, and P_3 = P_{3OT} + P_{3CT} = 1% for n = 3 clusters statistically clustered in the lattice. From the bulk using EPR lineshape arguments and susceptibility fit were shown to prove that formation of larger clusters than statistically predicted was shown by Mullin[13], Galazka[10], and Oseroff.[11] Within the nanocrystal lattice, each domain will have a magnetic moment and the interaction

of those moments will induce a net magnetic moment for the individual nanocrystal (intra-dot). If the nanocrystal net magnetic moment is large enough, inter-dot (dipolar) coupling may lead to the observation of RT ferromagnetism. The observation of ferromagnetism in bulk Mn doped II-VI semiconductors requires the inclusion of interacting magnetic moments of clustered Mn centers within the lattice and the magnetic response is dependent on the size and concentration of clusters in the lattice.[13] Due to the size constraint of the system the observed transition is that of the single domain characteristic transition, expected for nano-sized particles. The influence of inter-dot coupling will not be observed in a bulk system where the cluster interactions are already inclusive and are considered domain interactions.

In nanoparticles, since the same probability for clustering of the ions exists as for systems, annealing should induce enhanced ferromagnetic exchange by inducing cluster formation. The clustering is a result of the strain relief when there are vacancies which can raise the energy potential of its environment totaling in electron traps. The vacancies are evident from fluorescence spectra of small nanoparticles where trap state emission is the dominant form of photoluminescence.[57] The nature of the migration is dependent on the reaction rates of formation, the nature of the defect ion, and the host lattice.[58, 59]In addition, the high surface area and high strain of the nanoparticle system may influence the nature of doping and may enhance clustering to relieve strain and thus be critical in understanding the magnetic response.[22]

2.1   1% Mn:CdSe Experimental

The synthesis of the 1% doped 4.0 nm Mn:CdSe was carried out by reaction of $Li_4[Cd_{10}Se_4-(SC_6H_5)_{16}]$ (Cd_{10}) and $MnCl_2$ in hexadecylamine analogous to earlier studies.[27, 52, 24, 53, 28] The reaction was carried out at 120 °C to allow Mn ion exchange with the Cd ions in the Cd_{10} cluster. Exchange of metal ions into the clusters has been observed previously.[60] Growth of the nanoparticle was conducted at 230 °C for 3 h and isolation of a 4 nm particle was achieved by precipitation of the nanoparticle from a toluene solution through the addition of MeOH. The product was cleaned three times using toluene/methanol, followed by three sequential pyridine ligand exchanges at 70°C in order to remove unincorporated Mn ions. For the experimental studies, the isolated sample was divided into two parts, a pre-annealed and a post annealed sample.

Li$_4$[Cd$_{10}$Se$_4$(SPh)$_{16}$]   Hexadecylamine   Toluene/Methanol
          + $\rightarrow$ @ 120 ^{o}C 3 hr $\rightarrow$ 230 ^{o}C 3 hr $\rightarrow$ 3X $\rightarrow$
       MnCl$_2$

                                                                                                    $\rightarrow$ analyzed
Pyridine
3X @ 70 ^{o}C

                    annealed   Toluene/Methanol   Pyridine
        $\rightarrow$ 210 ^{o}C 46 hr $\rightarrow$ 3X $\rightarrow$ 3X @ 70 ^{o}C $\rightarrow$ analyzed
                in Hexadecylamine
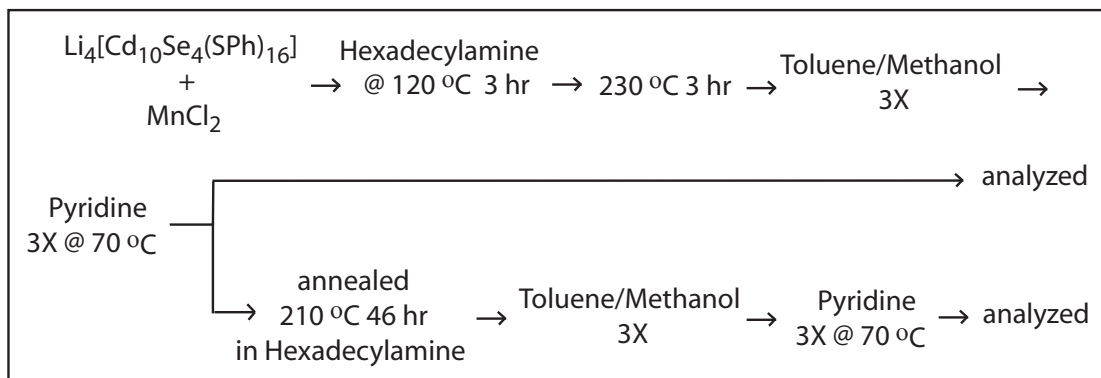
Figure 2.1: Flow chart of the synthesis and annealing procedure.

The post annealed sample was generated by dissolution of the pyridine capped Mn:CdSe sample in hexadecylamine at 210°C for 46h and isolation as described above.

2.2   1% Mn:CdSe Discussion

UV-visible, powder X-ray diffraction, and TEM were obtained for the pre and post annealed sample to verify no significant change in particle diameter or structure occurs. The first exciton in the absorption spectroscopy for the pre-annealed sample is at 2.30 eV corresponding to a 3.7 nm nanoparticle and is found to shift 21 meV to lower energy following annealing, suggesting growth by approximately a single lattice plane (3.8 nm). Size distribution for these samples is 10% based on the FWHM of the first excitonic feature. Powder XRD identifies a wurtzite crystal structure for both the pre and post annealed sample with an average size of 4.6 nm based on a Scherrer broadening analysis of the <110>, <103>, and <112> reflections (Table 2.1). The PXRD (4.6 nm), absorption (3.7 nm), and TEM (3.9 nm) are in reasonable agreement, with the larger value from PXRD suggesting the materials are highly crystalline.

The shifts in the pXRD lattice constants relative to a 4 nm CdSe sample isolated identically to the Mn:CdSe samples are summarized in Table 2.2. The pXRD reflections exhibit a compression between the pre and post annealed samples of 0.014 Å, which is larger than the expected 0.0012 Å for a 1 % Mn(II) doping on the Cd(II) site. While pXRD can provide evidence of doping, the observation can be skewed by internal clustering within the lattice leading to a non-linear deviation. Thermal ion migration of the Mn ions in the wurtzite CdSe quantum dot into small cluster domains is expected to relieve strain induced by the ~6 % lattice contraction about the Mn ion. The larger observed compression in the pXRD data suggests clustering may be present in these materials and larger than theoretically predicted. Following annealing the increased compression may suggest increased clustering by ion migration is occurring.

Enhanced clustering in these materials following annealing is further evident upon inspection of the magnetic data. The magnetic behavior of the pre and post annealed samples in solution and as powders are dramatically different (Figure 2.2). For the post-annealed powder sample, the magnetic susceptibility under zero field cooled and field cooling at 100, 200, 400, and 600 G is shown (Figure 2.2A).

Table 2.1: Size comparison in pre- and post- annealed nanoparticles using Scherrer broadening and TEM measurements

pre-annealed		post-annealed	
$2\theta < hkl >$	Size (Å)	$2\theta < hkl >$	Size (Å)
41.91	48.7	42.05	48.48
45.51	43.88	45.65	42.81
49.33	44.93	49.54	45.46
TEM size	39	TEM size	39

Table 2.2: Wurtzite lattice constants of CdSe and pre and post annealed Mn:CdSe.

	a (Å)	c (Å)	c/a
CdSe	4.299	7.011	1.631
Mn:CdSe pre-annealing	4.310	7.071	1.641
Mn:CdSe post-annealing	4.296	7.051	1.641

Figure 2.2D show magnetic susceptibility of the powdered post annealed sample at 100 G field cooled with a Brillouin function fit to the high temperature portion of the data. The data for the pre-annealed sample at zero field cooled (ZFC) fit to a Brillouin function over the complete temperature range is shown in Figure 2.2C. Field cooling of the pre-annealed sample does not influence the magnetic data.

In the pre-annealed sample the solution and powder data is a classical paramagnet. The data for the post-annealed sample at zero field exhibits a peak at 11 K, while the powdered pre annealed sample lacks such a peak. In the solution data for the post annealed sample (Figure 2.2B), the feature is shifted to lower temperature, occurring at 4 K. Inspection of the temperature dependent deviation of the magnetic susceptibility trace observed at 100 G compared to ZFC for the powdered post annealed sample suggests that the sample has a blocking temperature (T_B) of 40 K (Figure 2.2A). Alternatively, the 40K transition may be due to spin glass behavior. *ac*-susceptibility measurements, as detailed below, suggest this is not a classic spin glass. The observation of the magnetic feature 30 deg below TB can be attributed to a distribution in exchange energies for different sized clusters within the nanoparticles or nanoparticles- nanoparticle interactions (inter-dot). This means that the moments of the individual clusters within a given nanocrystal will freeze at different temperatures and only the average freezing point of the ensemble of intra-dot and inter-dot interactions will appear as a feature in the susceptibility curves. Consistent with this observation the 11 K feature is observable even at 100 G. The low temperature transition is due to the inter-dot interactions of superexchange between the Mn ions.

One possible method to analyze the inter-dot contributions to this feature is dilution experiments. Upon dilution the 11K feature disappears in the susceptibility traces (Figure 2.2). The loss of the 11 K feature upon dilution of the post-annealed sample into octylamine (Figure 2.2B) may be due to loss of intraparticle magnetic exchange; however a more likely cause is a change in the inter-particle interactions while the solvent causes a large diamagnetic background that inhibits the ability to see any evidence of the higher transition.

Inter-dot coupling effects have been observed to contribute the magnetic susceptibility by Rotello[61], with a change in the blocking temperature upon dilution of Fe_2O_3. The results of the dilution experiment are suggestive of inter-particle interactions in the Mn:CdSe system.
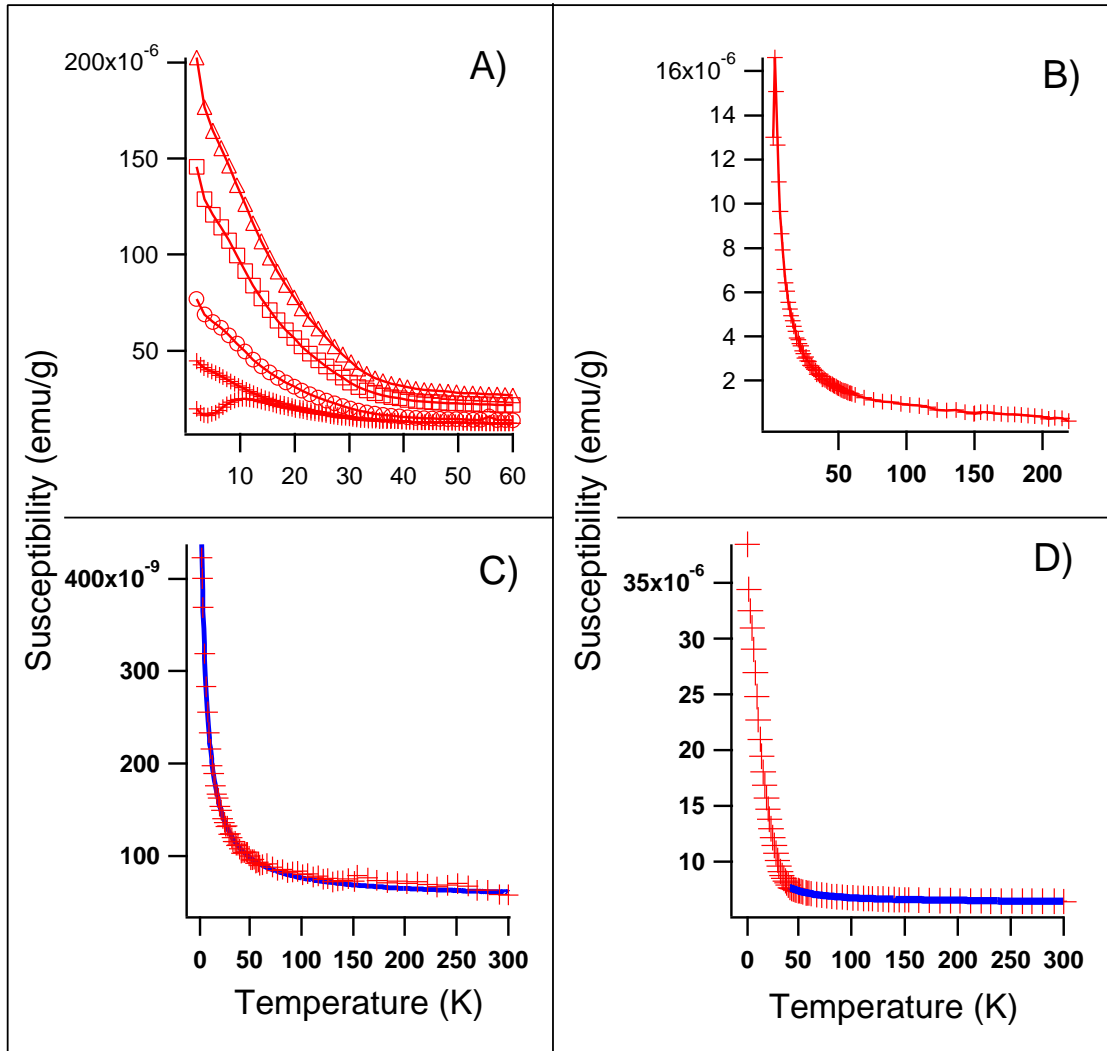
Figure 2.2: Magnetic susceptibility of pre and post annealed 1% Mn:CdSe. A) Post-annealed zero field cooled (bottom curve) and field cooled at 100 (+), 200 (○), 400 (□), and 600 G (△). B) Post-annealed field-cooled in Trioctyl amine. C) Pre-annealed field-cooled. D) Post-annealed field-cooled with a Brillouin function fit.

This is probable if the individual magnetic moments of the clusters within the dot couple to give rise to a large magnetic moment for the single domain like nanocrystal. The powder samples show high temperature paramagnetism with differences in the contribution of exchange following annealing. This can be analyzed by fitting the temperature dependent magnetic susceptibility data for the powder samples to a Langevin (eq 2.2a) and Brillouin function (eq 2.2b).[35]

$$\chi = \frac{N_0 g \mu_B J B_j(\eta)}{H} \tag{2.2a}$$

$$B_j(\eta) = \frac{2J+1}{2J} \coth(\frac{2J+1}{2J}\eta) - \frac{1}{2J} \coth(\frac{1}{2J}\eta) \tag{2.2b}$$

$$\eta = \frac{gJH}{k_B(T-\theta)} \tag{2.2c}$$

Equation 2.2a is fit by allowing the values for N_o, J, and θ to float and the best fit parameters analyzed by non-linear regression. Prior to fitting the magnetic susceptibility data, the diamagnetic contribution from the host lattice is subtracted using the measured susceptibility on a 4 nm CdSe sample treated identically to the Mn:CdSe samples. In the equations, N_o is the molar volume, g is the Landé g-factor, μ_B is the Bohr magneton, J is the spin, and H is the applied magnetic field. The g value used (2.004) is obtained from EPR, as described below. To fit the susceptibility, the Brillouin function (eqn 2.2b) is used with η (eqn 2.2c) being equal to the ratio between the spin components and the thermal energy, where k_B is Boltzmann constant and θ is the experimental Curie temperature.

The pre-annealed sample can be fit over all temperature ranges as a paramagnet. The post-annealed sample can only be fit at high temperature to the Brillouin function due to increased exchange interactions below 40 K. For the pre and post annealed sample a value of J = 5/2 is measured using the Curie-Weiss equations (eq 2.2) as expected for Mn(II). The Curie temperature calculated for the pre (-0.23 K) and post (20 K) annealed sample are dramatically different indicating a switch from AFM to FM exchange following annealing. At low concentrations this is expected from the observations gathered from Oseroff.[11] The larger Curie temperature for the post-annealed sample is due to increased Mn ion clustering in the quantum dot lattice. In this size regime, the onset of ferromagnetic exchange should lead to SPM, which is confirmed by frequency dependent experiments on the post-annealed sample between 8-850 Hz (Figure 2.3).
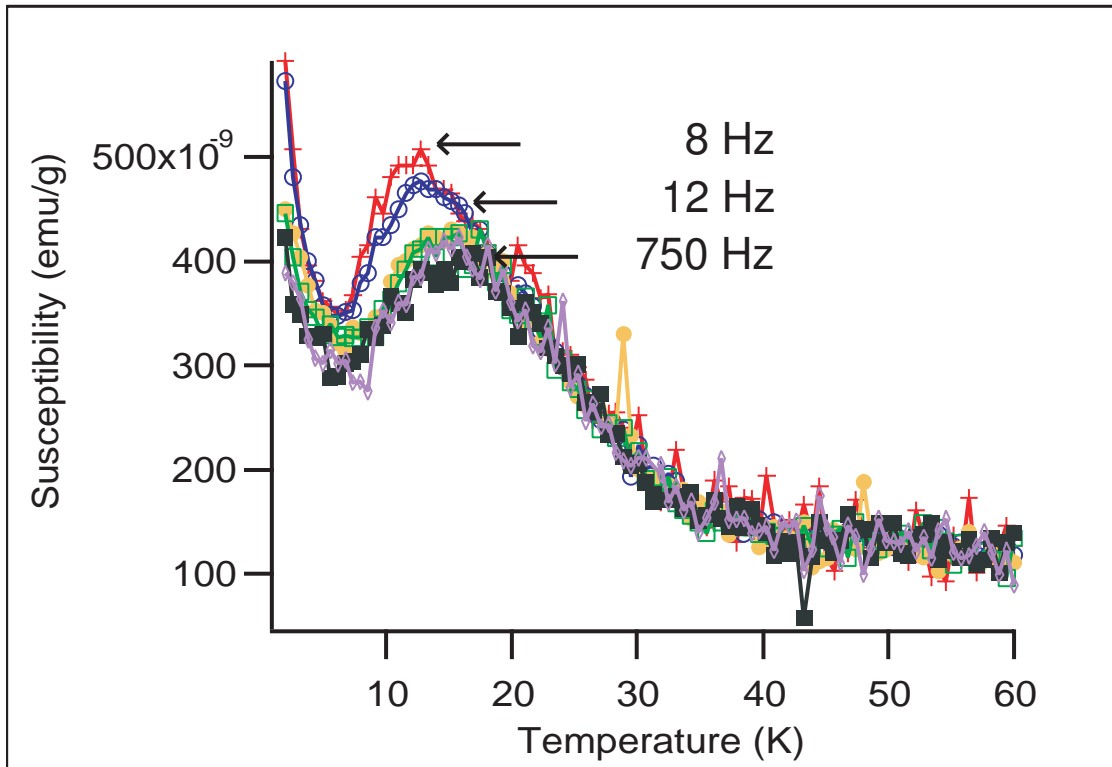
Figure 2.3: ac magnetic susceptibility of post annealed Mn:CdSe with a 4 Oe oscillating field at (+) 8 Hz, (○) 12 Hz, (●) 250 Hz, (□) 350 Hz, (■) 750 Hz, (◇) 850 Hz.

As seen in the ac-magnetic susceptibility, the largest tangential loss occurs for the data collection at 8 Hz at 10 K with no detectable loss at 40 K.

The lack of a detectable transition at 40 K in figure 2.3 does not indicate spin-glass behavior, but rather a slow magnetization occurs in these materials with formation of a SPM based on the ac results. Assignment of SPM rather than spin glass in this sample is obtained by using the criterion introduced by Mydosh, where the value of φ ($\varphi = \frac{\Delta T}{T_f \Delta(\log \omega)}$).[62]

For a spin glass the value is typically on the order of 10^{-2} while for a SPM the φ range is 10^{-1}-10^{-2}.[62] Using this convention, the post annealed sample exhibits a value of 0.16 consistent with the individual quantum dots being SPM. EPR can provide evidence of the degree of Mn clustering, as well as discrete information of the Mn doping site, and the Mn oxidation state. Mn (II) clustering will lead to dipolar broadening with loss of hyperfine structure. Q-band EPR measurements were performed at room temperature on powdered Mn:CdSe samples (Figure 2.4). Mn(III) an s = 2 Jahn-Teller ion is not observed in the EPR data for either sample and would give an EPR signature at a lower field (higher g-value) if present with much wider linewidth due to zero-field splitting. Assignment of the two contributions to the EPR spectra is gained by inspection of Q-band and X-band data, as well as power dependent measurements.[63]

There are two observable contributions to the EPR spectra, an exchange broadened (clustered Mn) term and a hyperfine split (isolated sites) term. The g-value for both samples are identical within experimental error (g = 2.004). The calculated g value is well within the literature range of 2.001-2.006 for Mn(II) doped II-VI semiconductors.[64]

The EPR data (Figure 2.4) for the pre and post annealed samples are similar at room temperature with a strong hyperfine feature (6-line pattern) for Mn(II) and a broad dipolar term. The dipolar term is increased in relative magnitude in the post-annealed sample. Lowering the temperature facilitates the observation of the broad dipolar component in both samples which is correlated to the onset of magnetic exchange observed in Figure 2.2. At 5 K the difference is more dramatic with pre annealed sample being composed primarily of isolated manganese with a small dipolar contribution, while the post annealed sample contains less than a percent of isolated manganese and is dominated by the dipolar term. The larger ferromagnetic exchange constant in the post annealed sample observed in the temperature dependent magnetization plots suggests the dipolar term should saturate at low T.
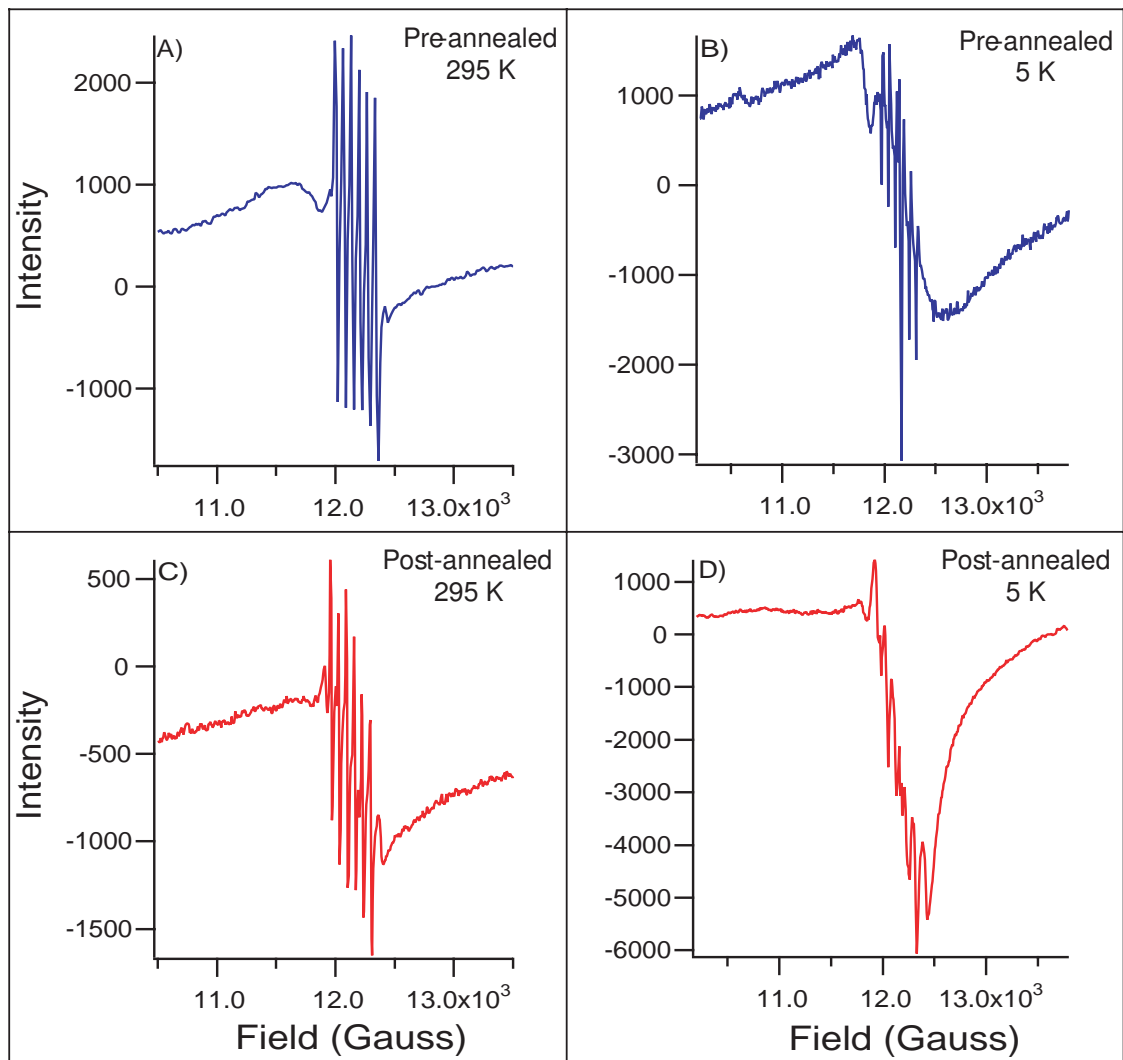
Figure 2.4: Room temperature and 5K Q-band EPR of pre and post annealed Mn:CdSe. A) Pre annealed at room temperature. B) Pre annealed at 5 K. C) Post annealed at room temperature. D) Post annealed at 5 K.

In the post annealed sample saturation of the dipolar signal is observed below the blocking temperature (Figure 3D).

Analysis of the hyperfine structure in Figure 3 provides insight into the site occupation of the Mn. The smaller Mn ion is expected to distort in the CdSe lattice, which his observable in the EPR data (Figure 2.4). The EPR data suggest the Mn site is a trigonally or tetragonally distorted Td which leads to the observation of forbidden EPR transitions attributed to a stronger spin-orbit term arising from symmetry breaking and is assigned to the $-1/2 \rightarrow 1/2$ [65]. Van Wierengen demonstrated the magnitude of the Mn^{2+} hyperfine splitting constant is dependent on the covalency of the site occupied by the manganese ion with more ionic sites exhibiting larger hyperfine constants. This empirical observation allows insight into the location of the manganese to be gained with respect to the different possible sites present in a nanoparticle (core or surface). One expects the surface sites to be more ionic than the more bulk-like core and therefore surface Mn ions should exhibit a larger hyperfine splitting than internal Mn ions. Consistent with this assumption, values for the hyperfine constant of 62 - 65 x 10^{-4} cm^{-1} are observed for internal Mn ions in bulk Mn:CdSe[64], and larger hyperfine splittings (85 x 10^{-4} cm^{-1}) were observed for Mn ions isolated on the surface of CdSe.[25] The measured hyperfine splitting constant in both the pre and post annealed sample is 62.0 x 10^{-4} cm^{-1}. This allows assignment of core doping of the Mn into the CdSe in these materials.

Perhaps the most significant observation in the EPR is the ratio of the two EPR absorptions in both samples. Inspection of the ratio of the EPR signatures indicates the dipolar term for both samples contributes $\sim$ 80-90% of the EPR signature, inconsistent with statistical doping value of 1% predicted by the probability functions in eqn 1. By integrating the EPR signals, the hyperfine term accounts for 24% of the signal in the pre-annealed sample, but only about half (12%) in the post annealed sample. The drop in the hyperfine component following annealing correlates with the observed onset of ferromagnetism in the post-annealed sample. This result supports the earlier assumption of thermal annealing leading to increased Mn ion clustering in the CdSe quantum dot; and to the onset of ferromagnetic exchange following annealing. The observation of intra-dot and inter-dot interactions contributing to the onset of SPM behavior in the post-annealed sample can be verified by inspection of the field dependent magnetization plots in Figure 2.5. Following annealing, a coercive field of 95 mT (Figure 2.5A and Figure 2.6A) with magnetic saturation

at 2 T (M_{sat} = 3600 emu/mol of Mn) is observed at 2 K (Figure 2.5A). The pre-annealed sample at 2 K shows no field dependent magnetization and can be fit to a purely paramagnetic exchange interaction consistent with a low concentration of Mn clusters being present in the pre-annealed sample. In solution no observable coercivity is evident at any temperature (Figure 2.5 B and D) due to the large diamagnetic contributions to the signal and loss of inter-dot interactions. In the post-annealed powdered sample the coercivity is reduced as the temperature increases with a coercivity of 0.006T at 20 K (Figure 2.5 C) and a loss of saturation above the blocking temperature (Figure 2.6B) due to thermalization of the spins. Surprisingly, above 20 K the coercivity (0.001 T) saturates and remains constant up to 250 K (Figure 2.6C).

It is not well understood why the ferromagnetism continues as far as it does. The saturation at 20 K rather than at the blocking temperature implies two competing interactions determine the observed magnetic behavior. The observation of high temperature coercivity suggests the second ferromagnetic interaction persists at temperatures approaching RT, while the SPM phase has diminishing contributions to the total magnetic behavior as the blocking temperature of 40 K is approached. In order to verify that this second magnetization feature arises from the material rather than the cavity, the magnetization of the pre-annealed sample and non-doped CdSe was measured and no magnetization transition was observed for these samples. In addition, the SQUID response was check with an empty capsule to make sure that the signal was not from the magnet hysteresis. Evidence of the second magnetic transition in the post-annealed sample is apparent in the field dependent magnetization plots between 2 K and 65 K (Figure 2.7). The observed behavior as a function of temperature requires fitting to the superposition of two separate magnetization functions, whose contribution varies independently with temperature. Although the fit to a superposition of two ferromagnetic transitions is not entirely correct since the Brillouin magnetization function requires no spin interactions to be present, it is still empirically useful in interpreting the presence of the secondary magnetic dipolar interaction. At 2 K and 5 K, the field dependent data is dominated by the low temperature magnetization term and can be approximately fit to a single magnetization event using the Brillouin function, $M(H) = N\mu_0 gJB_J(\frac{gH\mu_0}{2k_BT})$, where N is the molar volume, μ_0 is the Bohr magneton, g is the free electron Landé g-value, J is the spin.
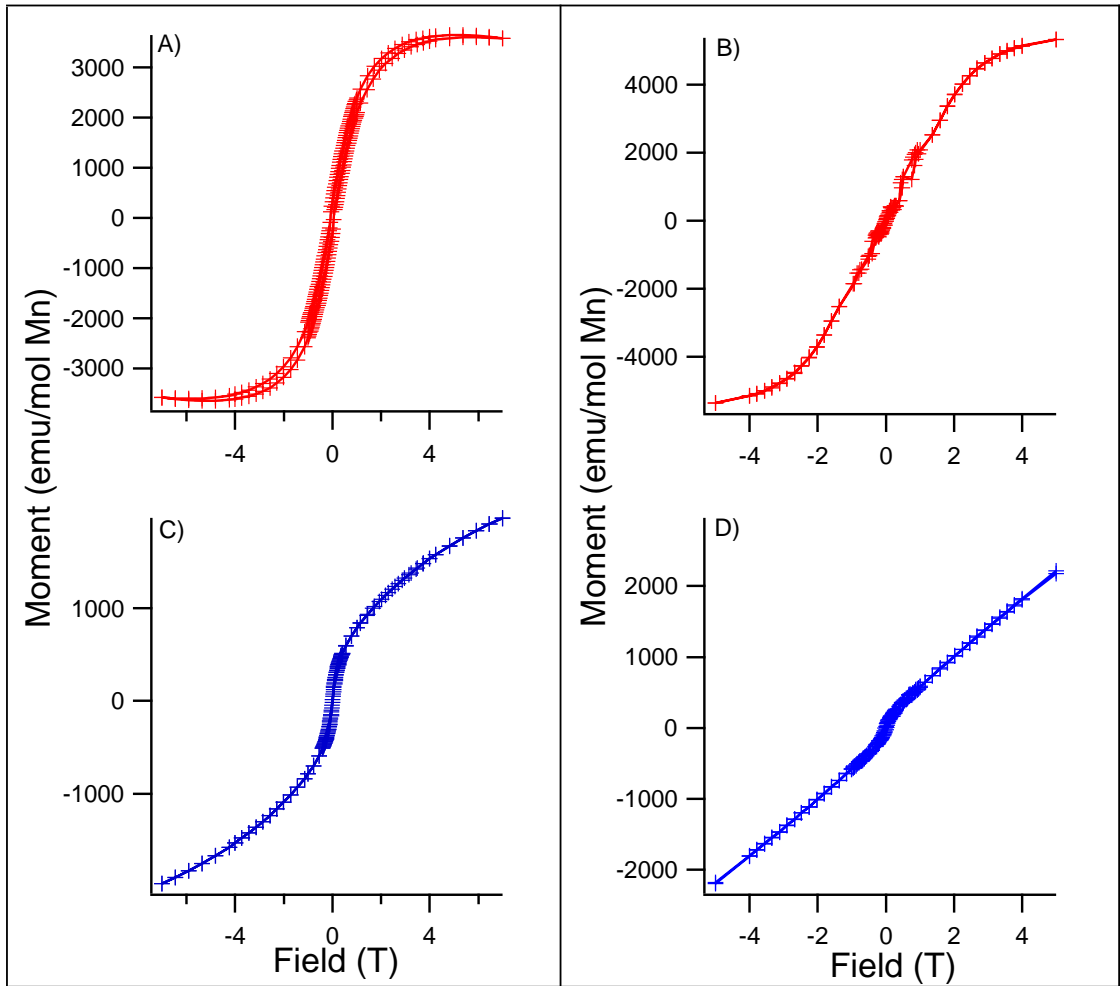
Figure 2.5: Magnetization of the post annealed Mn:CdSe sample at A) 2 K powder B) 2 K in Trioctylamine. C) 20 K powder. D) 20 K in Trioctylamine.
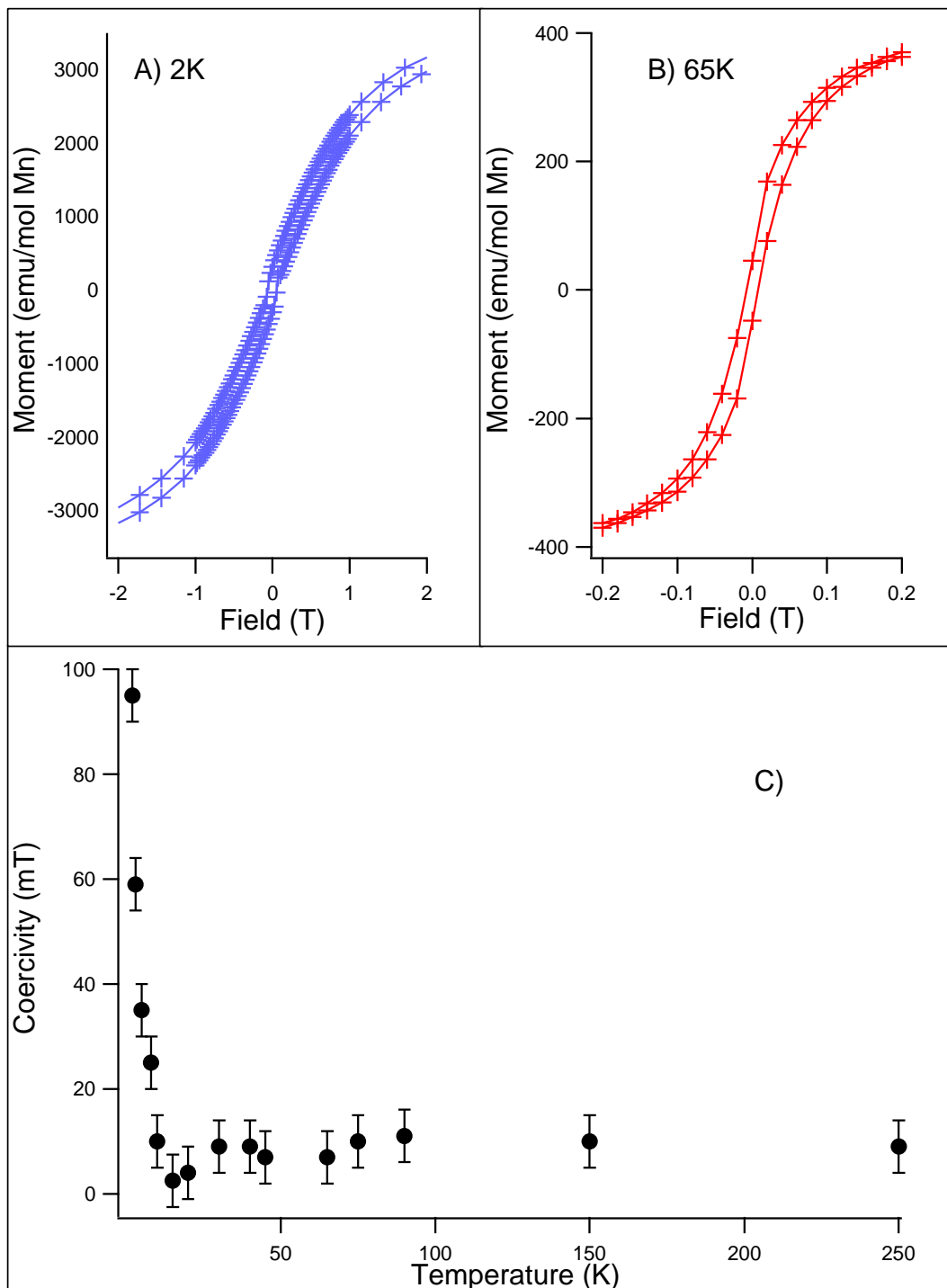
Figure 2.6: Magnetization of the post annealed Mn:CdSe sample at A) 2 K and B) 65 K. C) Plot of the coercive field as a function of temperature.
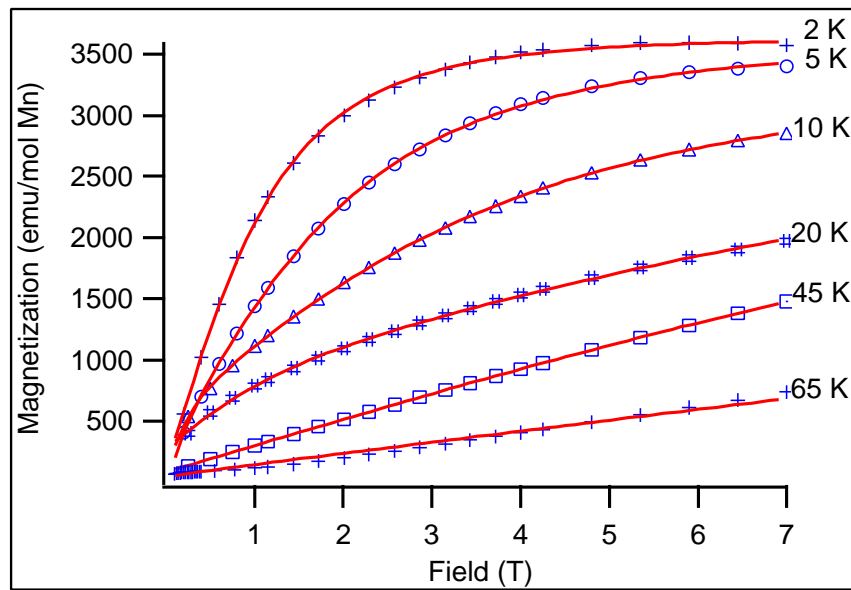
Figure 2.7: Magnetization of the post annealed Mn:CdSe at 2 K, 5 K, 10 K, 20 K, 45 K, and 65 K where the fit is represented by the solid line.

60

Fitting of the magnetization Brillouin function indicates the spin at 2 K and 5 K are higher than expected with values of $J_{2K} = 2.7$ and $J_{5K} = 3.0$. As the temperature is increased, the magnetic data requires a superposition of the two species, with the first component becoming paramagnetic above the blocking temperature. At 65 K, the magnetic data is cleanly fit to two contributions with the second term exhibiting magnetization saturation at lower field, ~ 0.2T, and a small value for magnetization saturation (3 emu/mol of Mn). The secondary (high temperature) magnetization is believed to be dominated by inter-dot coupling due to remnant magnetization moments of the internal clusters producing a net dot moment, while the low T magnetization event reflects the onset of a single domain SPM phase in the total ensemble of nanocrystals (Figure 2.8). Evidence of a long-range inter-dot coupling process is gained by analyzing the spin (J) of the susceptibility data using the magnetization Brillouin function. The first magnetic contribution was calculated to have a value of $J_1 = 3.8$ ($N_1 = 99.4\%$ molar contribution) and the second term $J_2 = 110$ ($N_2 = 0.6\%$ molar contribution) at all temperatures. The high spin value for the second species implies that this can not be accounted for by simply assuming large magnetic clusters being present in the lattice. The small total contribution to the magnetic moment of the second magnetization event indicates that this is most likely due to inter-dot coupling as suggested above, rather than an intra-dot magnetic transition. This is supported by the dilution experiments in Figure 1. The onset of the SPM behavior in these materials arises from sample annealing, which induces the Mn ions to migrate within the lattice and begin to form n > 2 ion clusters (Figure 2.8a). The Mn-Mn-Mn interactions give rise to a magnetic moment that form single-domain like quantum dots in the powdered ensemble. While ion-migration processes in CdSe are bulk are small (10^{-2} m²/s) for hexagonally lattices, the observation of annealing effects in these materials suggest the Mn ions have enhanced diffusion rates or the ion diffusion may occur along vacancies present in the growing particle to relieve strain. The change in magnetic behavior following annealing allows a model to be developed that explains the magnetization and EPR results. The SPM phase below 40K is due both to intra- and inter-dot coupling events arising from freezing of the spin of the clusters within a given nanocrystal.

This results in a large magnetic moment producing the single domain like quantum dot that can then couple the ensemble of dots producing a coercive field (Figure 2.6 and Figure 2.8b).
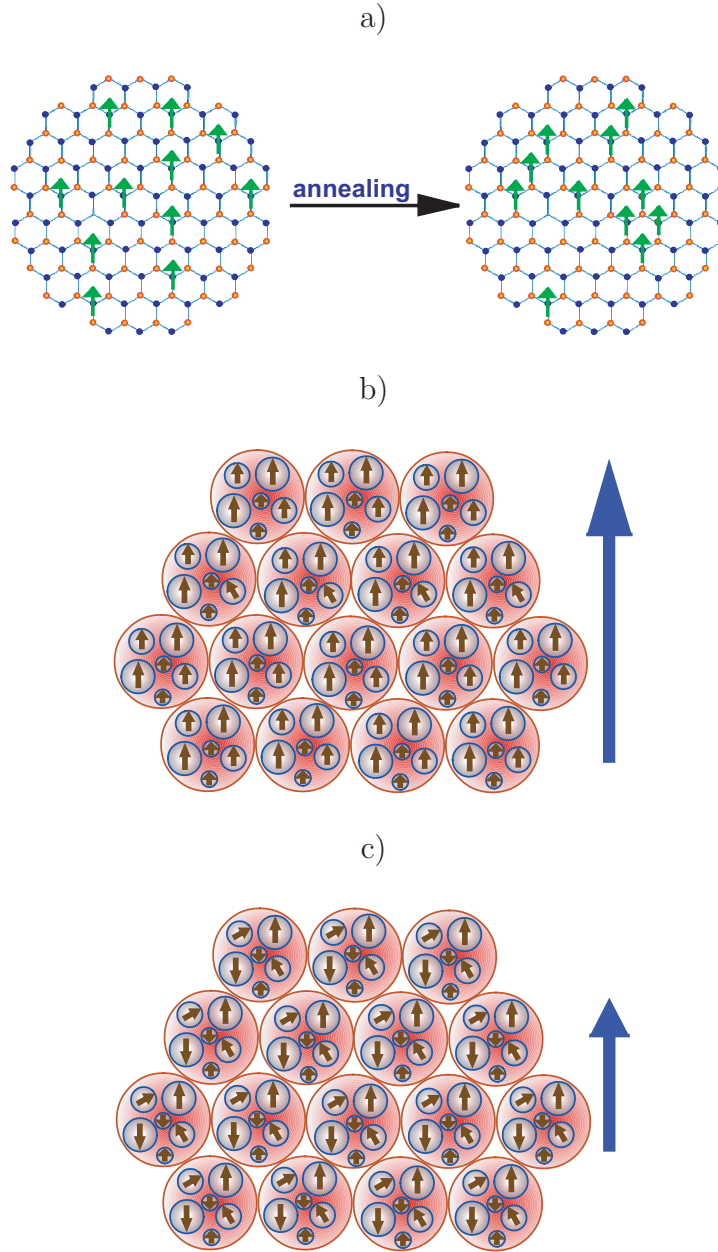
Figure 2.8: a) Intra-dot interactions of the Mn spins in a hexagonal (wurtzite) lattice where the cadmium, selenium, and manganese atoms are represented by dots that are blue, red, and green, respectively. Upon annealing the Mn(II) ions tend to cluster giving rise to ferromagnetic interactions leading to a larger magnetic moment. b) Magnetization below 40 K with the slow onset of the superparamagnetic phase with formation of single-domain quantum dots. c) Magnetization above 40 K arising from weak inter-dot interactions of remnant spin on larger clusters within the individual quantum dot.

Above 40 K, the nearly constant coercivity is assigned to inter-dot interactions arising from the remnant weak magnetic moments of the larger clusters within the quantum dot (Figure 2.8c). The inter-dot magnetization is expected for pyridine passivated nanocrystalline samples due to their propensity for agglomeration into larger superlattices when precipitated from solution. It is known that the agglomeration for CdSe materials has a high likelihood to form with conservation of crystallographic faces, which would enhance the probability of these interactions.[66] Similar observations of inter-dot coupling have been suggested to account for the observed magnetic anomalies in superparamagnet Fe_2O_3 nanoparticles isolated as powders from solution.[61]

2.3   1% Mn:CdSe Conclusion

Thermal annealing with formation of paramagnetic ion domains provides a mechanism to manipulate ferromagnetic exchange in semi-magnetic quantum dot systems. The magnitude of the exchange interaction between the Mn^{2+} ions in Mn:CdSe quantum dots is dictated by the position and number of Mn in the cluster and accounts for the observed magnetization for the Mn:CdSe samples studied. The assignment of the 40 K blocking temperature rather than at the observed anomaly at 11 K is accounted for by the distribution of cluster sizes and separation distances for the clusters within an individual quantum dot. The temperature dependent EPR spectrum, which is a convenient probe for measuring the magnitude of clustering in these materials, exhibits an increase in the broad component below the blocking temperature suggesting that this term is coupled to the ferromagnetic onset in the post-annealed Mn:CdSe sample in line with the proposed model. In conclusion, this study demonstrates that enhancing clustering in the lattice by thermal annealing can switch on ferromagnetism in doped semiconductors, pointing to an intriguing method to tailor the magnetic properties in quantum dot semi-magnetic systems.

CHAPTER 3

6.5% Mn:CdSe Spinwave

Nanocrystalline 6.5% Mn:CdSe 4 nm exhibits a Curie temperature of 51 K and coercivity of 0.94 T at 2 K. The magnetic exchange arises from coupling of intrinsic hole carriers in the lattice to Mn(II) spins where the result is a spin wave with an exchange predicted by the VCA-RKKY model. Spin wave behavior is observed in the heat capacity and magnetization data for the nanocrystals. The large, intrinsic, carrier concentration is unanticipated and ascribed to cadmium vacancies producing a 600 meV intra-gap state.

3.1   6.5% MnCdSe Introduction

In nanocrystalline DMS materials, the incorporation of paramagnetic ions into semiconductor host lattices can lead to the observation of rich magnetic phases. Antiferromagnetic (AFM) and ferromagnetic (FM) exchange have been observed between randomly substituted magnetic ions on the cation site depending on the ion concentration and intrinsic carrier densities. [4, 7, 15, 10, 11, 18, 67, 68]. In an earlier study, we observed switching from paramagnetic to superparamagnetic behavior in 1% doped Mn:CdSe (4 nm) following thermal annealing of lyothermally grown nanomaterials[69]. The onset of FM exchange was initially believed to be solely attributed to clustering of Mn (II) within the nanocrystal in analogy to onset of clustering induced FM exchange previously reported in bulk materials[69, 12]. While clustering of the Mn in the II-VI lattice by vacancy driven annealing explained the onset of ferromagnetic exchange, the magnitude of the spin, as estimated by spin counting, could not be described purely by a clustering only mechanism.
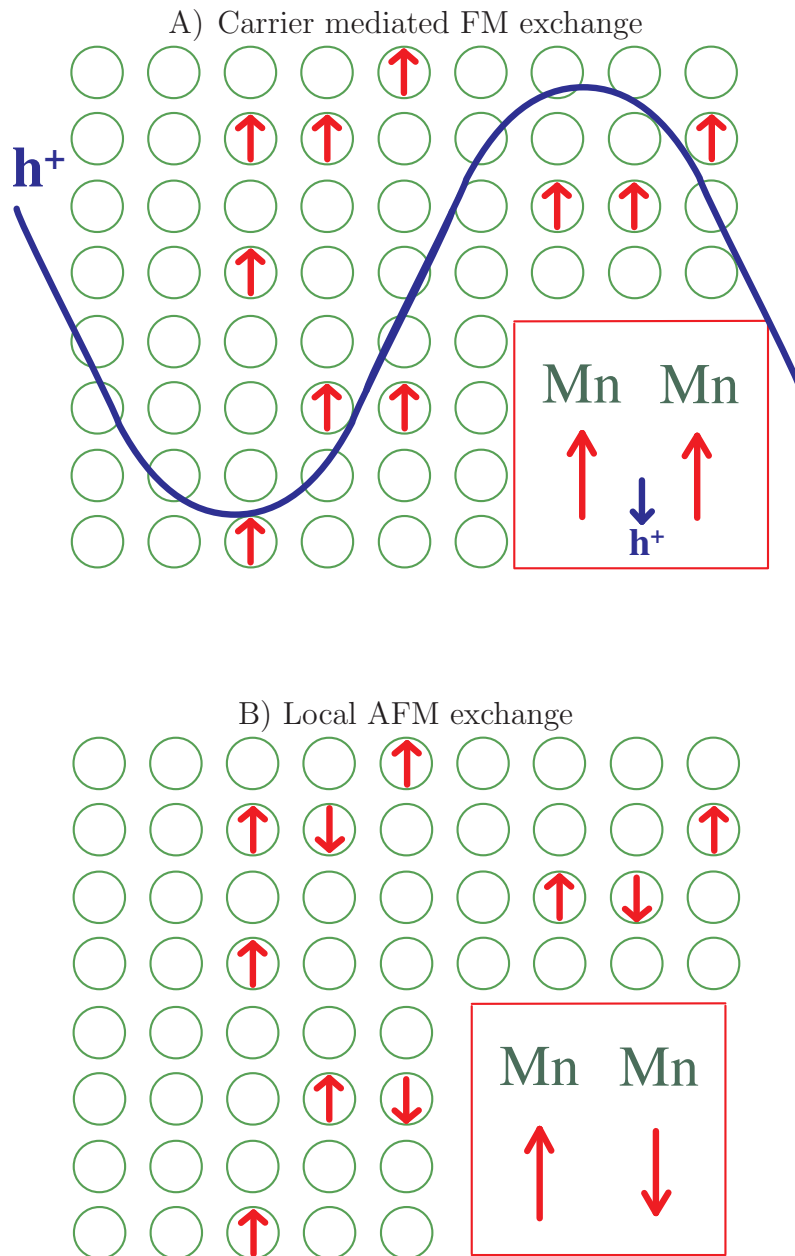
Figure 3.1: A) The polarization of the carriers in the virtual crystal approximation of RKKY where the exchange interaction is described as a propagating wave (spin wave) formed from the mobile intrinsic hole carriers leading to ferromagnetism. B) Magnetic exchange interaction between magnetic ions in a RKKY model with local couplings between nearest neighbor ions, cluster of ions or individual ions, where no spin wave is present and paramagnetism or antiferromagnetism prevails.

In the present manuscript, we observe formation of a superparamagnet in unannealed 6.5% Mn:CdSe (4 nm) isolated directly from the reaction without a thermal annealing step. Analysis of the field dependent and temperature dependent magnetization data shows a Tc = 51 K with a 0.94 T coercivity at 2 K. The magnitude of the coercivity and Tc is larger than expected for a random clustering model. This suggests some other mechanism is involved. Understanding the nature of magnetic exchange in nanocrystalline dilute magnetic semiconductors (DMS) remains an important if not controversial issue [70, 2, 20]. In these materials the interplay between lattice, spin and electronic contributions must play a role.

If ferromagnetism does not arise as a result of a clustering only mechanism, another contribution must be present to explain the magnetic properties observed in the 6.5 % Mn:CdSe. Theoretically, FM exchange in doped II-VI materials has been predicted to be achievable in the presence of intrinsic hole carriers (10^{20}) in the lattice[42], which delocalize over the entire Brillouin zone generating a spin wave as a result of the coupled dopant spins. Application of the virtual crystal approximation RKKY (VCA-RKKY) model allows formation of a superparamagnet through the antiferromagnetic coupling between the local Mn ion and delocalized intrinsic carriers (Fig. 3.1). While this has not been experimentally demonstrated on Mn (II) doped II-VI materials, examples have been reported in a range of the other dilute magnetic semiconductors, both in bulk and nanoscale[71, 7, 70, 72, 73, 74, 54, 67].

Historically, it has been postulated that carriers are not present in lyothermally grown nanomaterials, although a growing II-VI body of evidence suggests that carrier participation may be important to explain the magnetic exchange in these materials.[48, 75]. The onset of FM exchange induced by the presence of intrinsic carriers would give rise to an observable spin-wave with Bloch law temperature dependence ($T^{3/2}$), which will be confined to the volume of the nanocrystal. Therefore, the spinwave's wavevector (q_o) and the nanocrystal dimensions should correlate [76]. If the FM exchange in the Mn:CdSe nanocrystal only arose from clustering, the spin wave would be absent.

3.2 Experimental

CdSe and 6.5% Mn:CdSe nanocrystal samples were prepared as pyridine-capped, 4 nm spherical particles with wurtzite symmetry, as previously described[69].
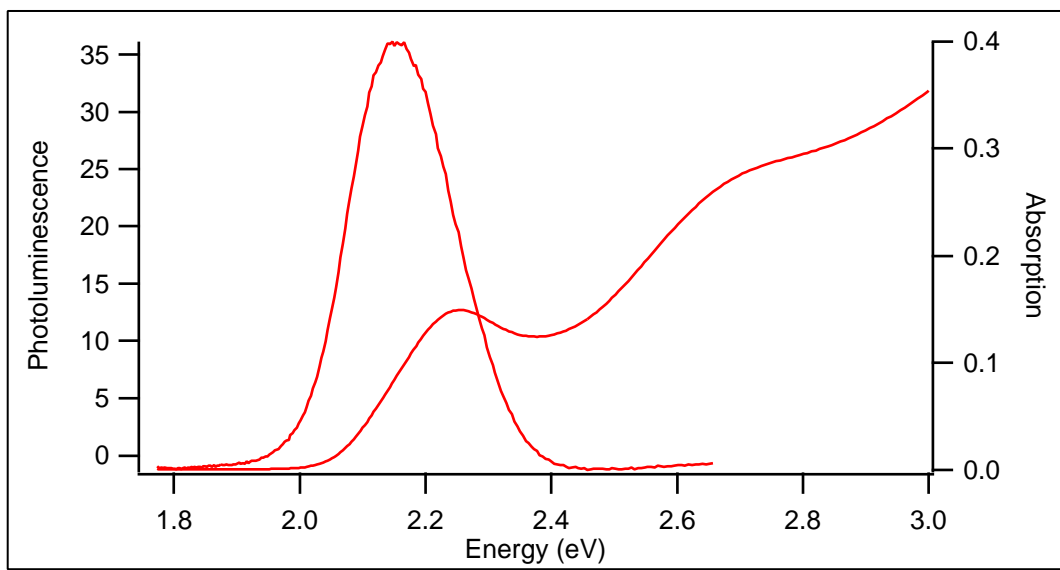
Figure 3.2: Absorption and photoluminescence of MnCdSe in a toluene solution.
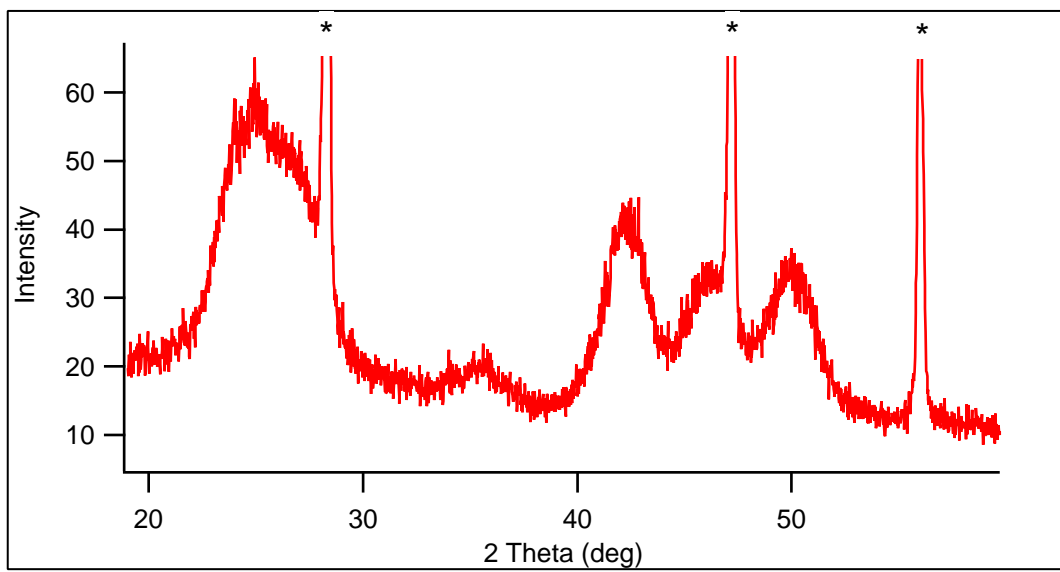
Figure 3.3: Powder XRD of MnCdSe.

To remove excess Mn and hexadecylamine, the samples were precipitated (3X) using hexane/methanol followed by pyridine stripping (3X) by treatment of the nanocrystals in pyridine at 343 K for 12 h followed by hexane precipitation (3X). The effectiveness of this process to eliminate excess Mn and ligand from the isolated materials has previously been demonstrated by our group and others with no change in metal ion content following the second pyridine stripping step[69, 25]. Using standard protocols, optical absorption and photoluminescence (Fig. 3.2), transmission electron microscopy, X-ray diffraction (Fig. 3.3), and atomic emission spectroscopy were used to confirm the nanocrystal size, shape, and the average Mn(II) ion concentration. All magnetic and heat capacity measurements were performed on pyridine stripped Mn:CdSe and CdSe vacuumed dried powdered samples. The magnetic susceptibility and magnetization was performed on a 7 Tesla Quantum Design MPMS XL system. The heat capacity was performed on a 9 Tesla Quantum Design PPMS performing an background measurement before each run using the same amount of points as the measurement. The ac susceptibility was performed using the Quantum Design PPMS coupled to a signal generator to provide the 10 kHz ac signal (supplemental Fig. 3.5).

3.3 Results and Discussion

Evidence of the superparamagnetic magnetization and magnetic coercivity for the 6.5% Mn:CdSe (4 nm) sample can be observed by inspection of the temperature and field dependent SQUID data. Comparison of the zero-field-cooled and field-cooled magnetic susceptibility data (Fig. 3.4A), shows a Curie temperature at 51 K and a lower blocking temperature at 41 K for the powdered isotropic sample of pyridine capped 4 nm 6.5% Mn:CdSe. Tc is assigned to 51 K, rather than 41 K based upon the observed deviation in the magnetic susceptibility between the field cooled and zero field cooled susceptibility data. Consistent with the assignment of T_B arising from superparamagnetic (SPM) behavior, the coercivity approaches zero at the blocking temperature with a slope of 0.2 Tesla/K. The blocking behavior at 41 K can be assigned as a classical superparamagnet using the Mydosh[62] criterion applied to the ac-susceptibility measurements. φ becomes a measure of the relaxation affected by the groundstate of the system. In the ac-susceptibility measurements over the frequency range of 1-10 KHz yield a value of $\varphi = 0.2$ which is in the range for a superparamagnet (Fig. 3.5).
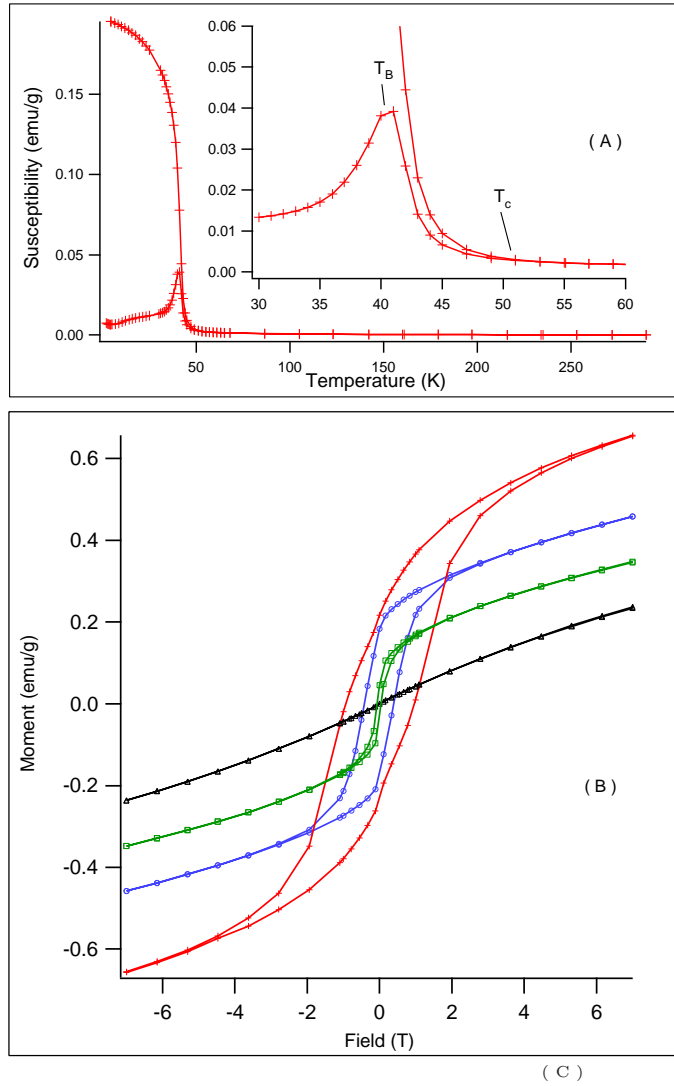
Temp. (K)	Coercivity (T)	Mag. Sat. (emu/g of material)	Mag. Sat. (emu/$\mu_B$mol of Mn)
2.0	0.937	0.6558	1.956
25.0	0.421	0.4583	1.367
41.0	0.067	0.3449	1.09
50.0	0.0041	0.2342	0.698

Figure 3.4: A) Field-cooled (0.05 T) and zero-field-cooled magnetic susceptibility of 6.5% Mn:CdSe powder. inset: Closeup of the transition. B) Hysteresis at 2 K (+), 25 K (∘), 41 K (□), and 50 K (△). C) Detailed temperature dependent coercivity and magnetization data for 6.5% Mn:CdSe (4 nm).
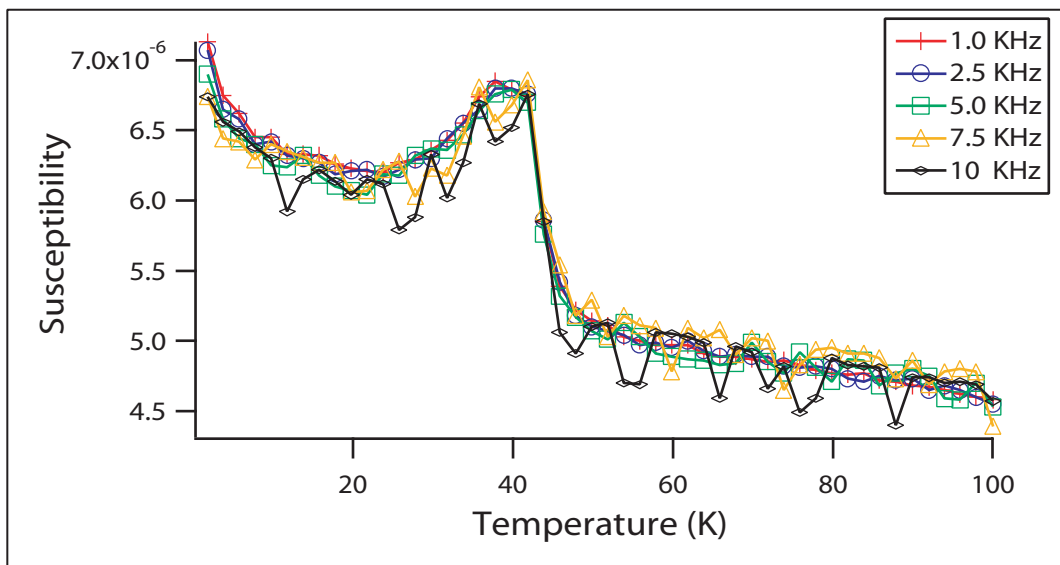
Figure 3.5: ac suscuptility of MnCdSe.

The onset of FM exchange is evidenced in the field dependent SQUID data, where a hysterisis is observed (Fig. 3.4B). The hysteresis plot does not exhibit complete saturation at 2 K. The coercive field at 2 K is ~0.94 T and a lower coercive field of 0.421 T is measured at 25 K (Fig. 3.4B). The lack of high field saturation at low temperature is not surprising due to the possibility of dipolar coupling, the variability of the doping levels per nanocrystal, the nanocrystal size variances (5% RMS), and the likely participation of Mn ions on the surface of the nanocrystal that differ from internally incorporated Mn ions due to the nature of the surface reconstruction. This would be expected to lead to a distribution in the onset of FM exchange.

If we assume the magnitude of the ferromagnetic exchange is near saturation at 7 T, the parentage of the observed magnetic moment can be assigned using a Langevin fit of the initial sweep of the magnetization at 2 K. Although the use of the Langevin function under unsaturated conditions is not entirely valid, it allows the relative number of spins per atom in the lattice to be calculated. Spin-counting at 2 K (7 T) yields a value of 1.96 moments per Mn(II) in the 6.5 % Mn:CdSe samples. This value is lower than the predicted value of 2.5 moments per Mn(II), suggesting that 22 % of the Mn are not accounted for in the total FM moment at 7 T. The missing 22 % of Mn spin can be accounted by considering the Mn centers are not coupled to the onset of the magnetic phase. If we assume the magnetism arises from only spins in the core of the nanocrystal (approximately 88-90 % of total ions for a wurtzite 4 nm nanocrystal), than the missing 22 % of Mn(II) can be assigned to non-participating Mn(II) on reconstructed lattice sites at or near the surface of the nanocrystal. The surface atoms are not expected to contribute to the magnetization because surface reconstruction gives rise to decoupled donor states that lie in the gap and would exhibit weak orbital coupling. This allows complete spin counting with the lower measured spin attributed to the lack of exchange coupling of the Mn at the surface layers, and therefore they contribute only as a paramagnetic perturbation to the total moment. In fact, assignment of the missing 22 % of spins to surface Mn ions would be consistent with the observation of a lack of saturation at 7 T (2 K) arising from the slow magnetization of Mn ions at the surface observed in the field dependent magnetization data.

3.3.1 Understanding the onset of FM

While fitting the field dependent magnetic data to a Langevin function allows the parentage of the magnetization to be accounted for, the observation of FM exchange can not be explained based on a classical RKKY model that accounts only for Mn-Mn interactions, which will be AFM in the nearest neighbor range[40, 24] or clustering of Mn ions[69], which leads to a weak, spin frustrated ferromagnetism. The presence of intrinsic hole carriers in the lattice may explain the observation of ferromagnetism. This may lead to a net FM exchange for the entire nanocrystal as predicted by the VCA-RKKY model. The VCA-RKKY model averages the total Mn spins over the entire Brillouin zone by coupling to intrinsic hole carriers in the lattice. At low concentrations (<10%) of dopant where correlation effects are small, the VCA-RKKY model predicts that the magnetization is dynamic and described as a spin wave (Fig. 3.1). Ferromagnetic exchange will be observed when the magnetic spins couple to free carriers in the lattice in which the exchange interaction is $JS_I \cdot S_{h+}$, where S_I and S_{h+} are the spins on the Ith Mn atom and a hole carrier, respectively.

$$[Mn]J_{pd}\sum_{i,I}\overrightarrow{S}_I \cdot \overrightarrow{s}_i \tag{3.1}$$

For systems where the VCA-RKKY model can be applied, a prediction of the carrier density necessary to produce the observed Tc[42] can be approximated by assuming a bulk p-d exchange energy,

$$T_c = \frac{[Mn]S(S+1)}{3k_B}\frac{J_{pd}^2}{(g^*\mu_B)^2}\frac{3N(\frac{g\mu_B}{2})^2}{2(E_f)} \tag{3.2}$$

where $[Mn]$ is the manganese molar concentration, S is the Mn spin (S= 5/2), J_{pd} the bulk p-d exchange interaction (-1.1 eV) [41], g^*, the carrier g factor (1.6) [43], g the Mn g factor (g = 2), E_f, the Fermi energy, and N the hole concentration (Fig. 3.6). Solving eqn 3.2 gives a carrier density of 1.8 X 10^{20} cm^{-3} for the 6.5 % 4 nm Mn:CdSe sample using the experimentally measured 51 K Tc (3.4). The prediction of 10^{20} carriers is surprising for nanocrystalline CdSe.

Although the VCA-RKKY predicts carrier concentration, measurement of holes is critical to justify its application in the present system. In bulk CdSe, carriers are present at low concentration due to vaccancy formation in the lattice[47]. The likely presence of vacancies, which can give rise to carriers, was suggested in our earlier study on clustering induced FM in 1% Mn:CdSe[69].
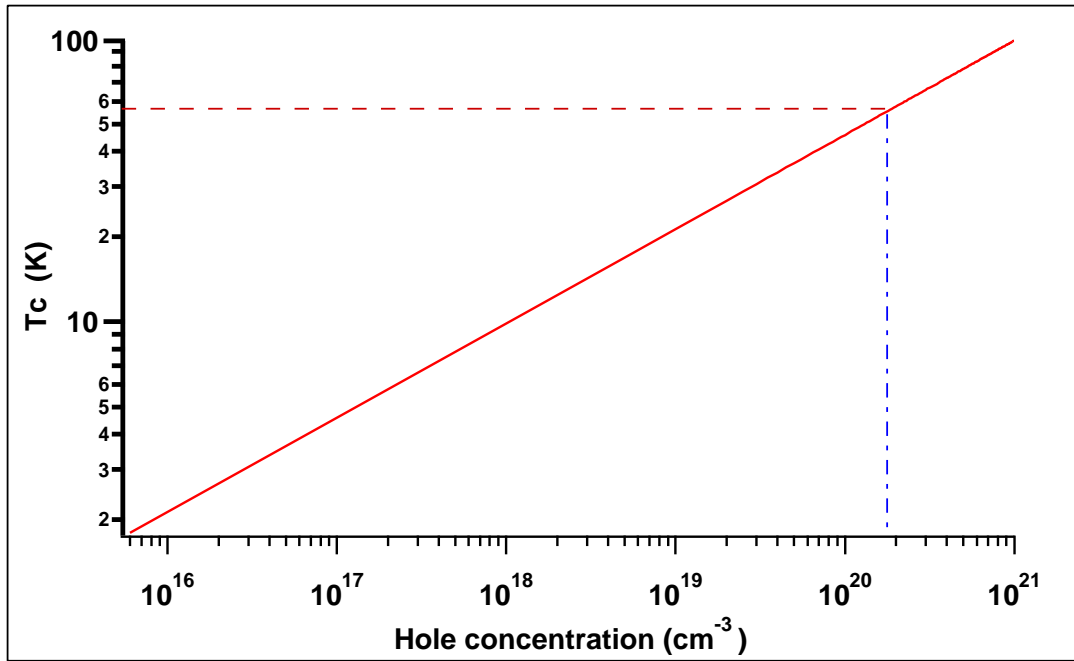
Figure 3.6: Predicted Curie temperature with respect to hole carrier concentration using VCA-RKKY for 6.5% Mn:CdSe. The lines represent the theoretical Tc at a value of 10^{20} cm^{-3} carriers. The dashed line represents the theoretical value for hole carriers at the experimentally determined Curie temperature.

Similarly carriers have been observed in nanocrystalline films where an acceptor state of 0.6 eV[48] is present, attributed to the bulk cadmium vacancy acceptor state[44]. To date, only chemically induced electron carriers have been measured by IR spectroscopy for lyothermally grown CdSe, following intentional injection of carriers (either chemically or electrochemically)[46].

The appearance of carriers in this study are believed to arise from the nature of the synthetic method which utilizes a molecular precursor to nucleate Mn:CdSe nanocrystal formation. Experimental attempts to quantify hole carriers using infrared spectroscopy have failed to produce an infrared signature that is detectable, consistent with our observations of a lack of IR signatures in these materials[46]. The presence of a high carrier concentration in nanocrystalline materials most likely can be attributed to contributions of surface species and internal vacancies in the lattice due to the rapid growth conditions for lyothermally grown materials. If compensation occurs at the surface, reconstruction can decouple these levels leading to formation of intrinsic carriers.

A technique employed for measurement of carrier density in bulk materials is low temperature heat capacity (C_p), where the Cp/T response at temperatures below 10 K can be attributed to electronic (C_E) contributions arising from free-carriers, thus providing the carrier density. By invoking a collective oscillation model, the total heat capacity of a semiconductor (C_p) can be fit to contributions arising from the lattice heat capacity (C_L, β) and carrier contributions (C_E, γ), of which the magnitude of the contribution depends upon the nature of the system. The electronic term is defined by Fermi-Dirac statistics and is attributable to the presence of carriers in a semiconductor lattice resulting in a linear temperature dependence[36].

$$C_p = C_L + C_E = \beta T^3 + \gamma T \tag{3.3}$$

For all materials, at higher temperature the heat capacity is dominated by the lattice following a T^3 dependence. For systems where carriers are present, the electronic term (C_E) is important below 10 K, where thermal population of the phonons is minimized. This leads to a non-zero intercept (γ) as T$\to$ 0 K when graphed as C_p/T vs T. Although the measurement of heat capacity below 2 K is difficult, the trend is useful in interpreting the presence of carriers.
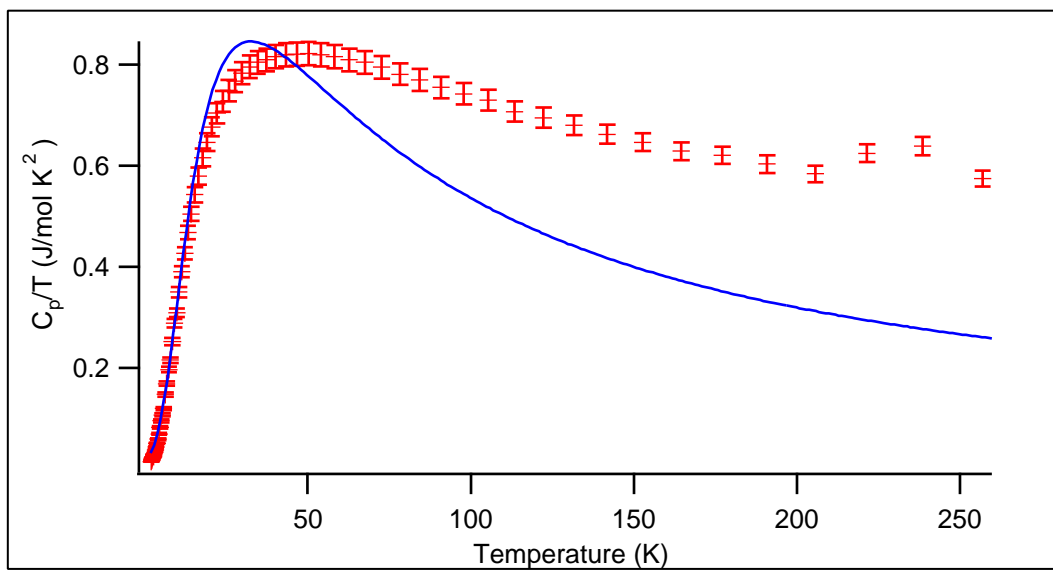
Figure 3.7: Heat capacity (Cp/T) of 4 nm CdSe at 0T (+) and theoretical fit to eqn 3.3 for lattice contributions contribution.

A plot of the field dependent heat capacity under zero magnetic field (C_P/T) vs T for 4 nm CdSe is shown in figure 3.7. Fitting the C_P/T spectra to contributions from the Debye (β) term (eqn 3.3) reveals that the Debye contribution is 3.54 ± 0.01 X 10^{-2} $\frac{J}{molK^2}$ for nanocrystalline CdSe and Mn:CdSe. This value is an order of magnitude larger than measured for bulk CdSe (3.2 ± 0.1 X 10^{-3} $\frac{J}{molK^2}$). The failure to fit Cp/T above 50 K is believed to arise from the passivating ligand contribution to the total Cp. The larger Debye term results in a lowering of the Debye temperature from 183 K for bulk CdSe to 84 K for 4 nm nanocrystalline CdSe using eqn 3.4.

$$C_v = 9Nk_B \left(\frac{T}{\theta}\right)^3 \int_0^{\theta/T} \frac{x^3}{e^x - 1} \, dx \tag{3.4}$$

The change in the Debye temperature from bulk to nanocrystalline CdSe is not surprising when contributions from phonon confinement, which is expected to play a role in 3-D confined nanomaterials, are considered[77].

At low temperature (<4 K) the C_L lattice (Debye) only fit (dashed line in Fig. 3.8) deviates from the experimental data and an electronic contribution must be included to account for the low temperature deviation (solid line), allowing γ to be extracted (Fig. 3.8). The magnitude of the electronic term increases by several orders of magnitude from 1.4 ± 0.1 X 10^{-4} ($\frac{J}{molK^2}$) for bulk CdSe to a value of 4.63 ± 0.01 X 10^{-3} ($\frac{J}{molK^2}$) for the 4 nm CdSe and Mn:CdSe. The non-zero intercept in the C_P/T plot is consistent with intrinsic carriers existing in the semiconductor lattices, with a larger carrier concentration in the nanoscale materials compared to the bulk materials (Fig. 3.8). The carrier density for the samples can be calculated from the electronic heat capacity (C_E) by assuming bulk values for the electron mass (m), carrier molar density (N), and molar density (V).

$$C_e/T = \frac{4\pi^3 m k_B^2}{3h^2} \left(\frac{3NV^2}{\pi}\right)^{1/3} \tag{3.5}$$

Fitting the expression yields a three order increase in the carrier density for nanocrystalline CdSe and Mn:CdSe (10^{20} cm^{-3}) when compared to bulk CdSe (10^{17} cm^{-3}). This value is in good agreement with the prediction using the VCA-RKKY model based on the experimentally measured Tc in Mn:CdSe.
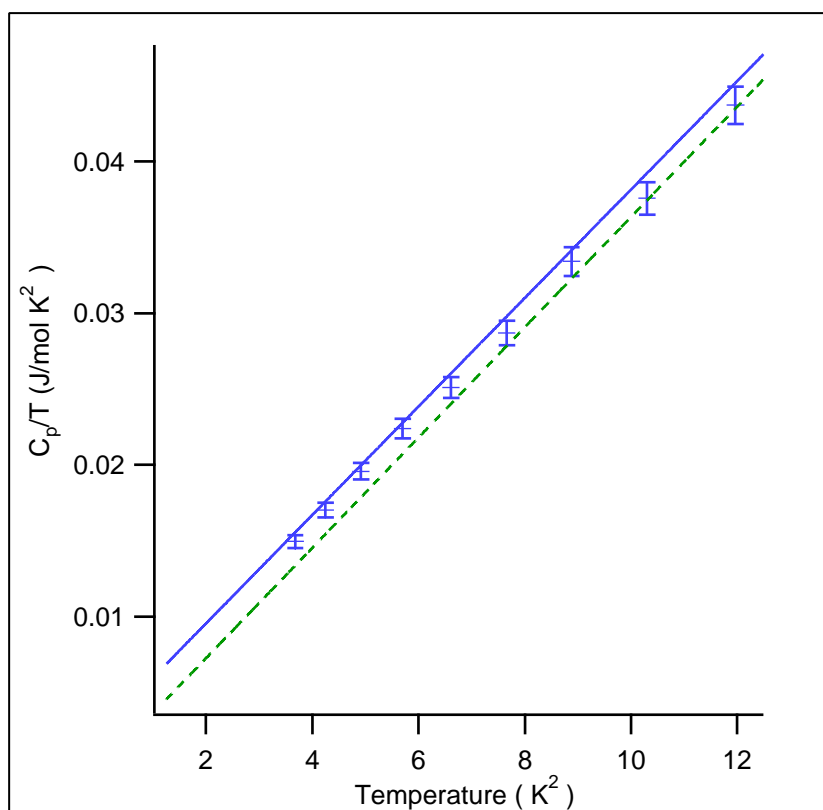
Figure 3.8: CdSe Cp/T at 0T (+), theoretical fit to lattice (Debye) contribution only (dashed), and fit (line) including electronic contributions.

3.3.2 Spin wave confinement

While in the absence of carriers, a PM or AFM magnetic signature is expected, the presence of carriers, while enticing, does not prove the onset of FM exchange in these materials arises from coupling to delocalized carriers (spin wave) in the lattice. Evidence of the presence of a spin wave can be provided by analysis of the magnetic heat capacity term that is predicted to follow Bloch law behavior as T approaches 0 K[76]. This contribution is significant only near 0 K and will give rise to a $T^{3/2}$ dependence if a spin wave is formed, as predicted by the Bloch equation [36]. Above 0 K, the magnetic contribution is small, but can be extracted by subtracting the electronic and lattice components from the Mn doped nanocrystal heat capacity data where the interpretation of the data is limited by the low temperature limitations of the system used. This allows an estimate of the magnetic term by fitting the Mn:CdSe (Fig. 3.9B) C_M/T using the 4 nm CdSe (Fig. 3.9A) Debye and electronic values and adding a Bloch dependence for the FM component $T^{3/2}$.

$$C_p = C_L + C_E + C_M = \beta T^3 + \gamma T + \delta T^{3/2} + \delta_o \tag{3.6}$$

Inspection of figure 3.9 shows the experimental data is in agreement with the fit for equation 3.6.

Using the fit to eqn 3.6 the magnetic component δ (3.96×10^{-2} (J/molK^2)) including the magnetic gap δ_o (6.50×10^{-2} (J/molK^2)) can be analyzed as T $\rightarrow$ 0 K. The magnetic term temperature dependence arises from the formation of low-lying excited state of the induced spin-wave and is expected to have a frequency that tracks the square of the wavevector. Formation of a spinwave in conjunction is strong evidence of a ferromagnetic nanocrystalline Mn:CdSe.

The observation of a Bloch law magnetic ($C_M\alpha$ $T^{3/2}$) heat capacity supports spin wave formation and therefore a delocalized carrier mediated FM exchange. The observed spin wave frequency (and therefore its size) is predicted to be confined to the nanocrystal size and should by consistent with the size of the nanocrystal. The spin-wave size is in effect the wavevector (q_o), where the energy gap induced by formation of the spin wave and can be expressed in terms of the magnetic exchange stiffness (D) and wavevector, $E = Dq_o^2$ [76]. The exchange stiffness can be calculated from either the magnetization data or the heat capacity, providing an internal calibration of the two experimental methods.
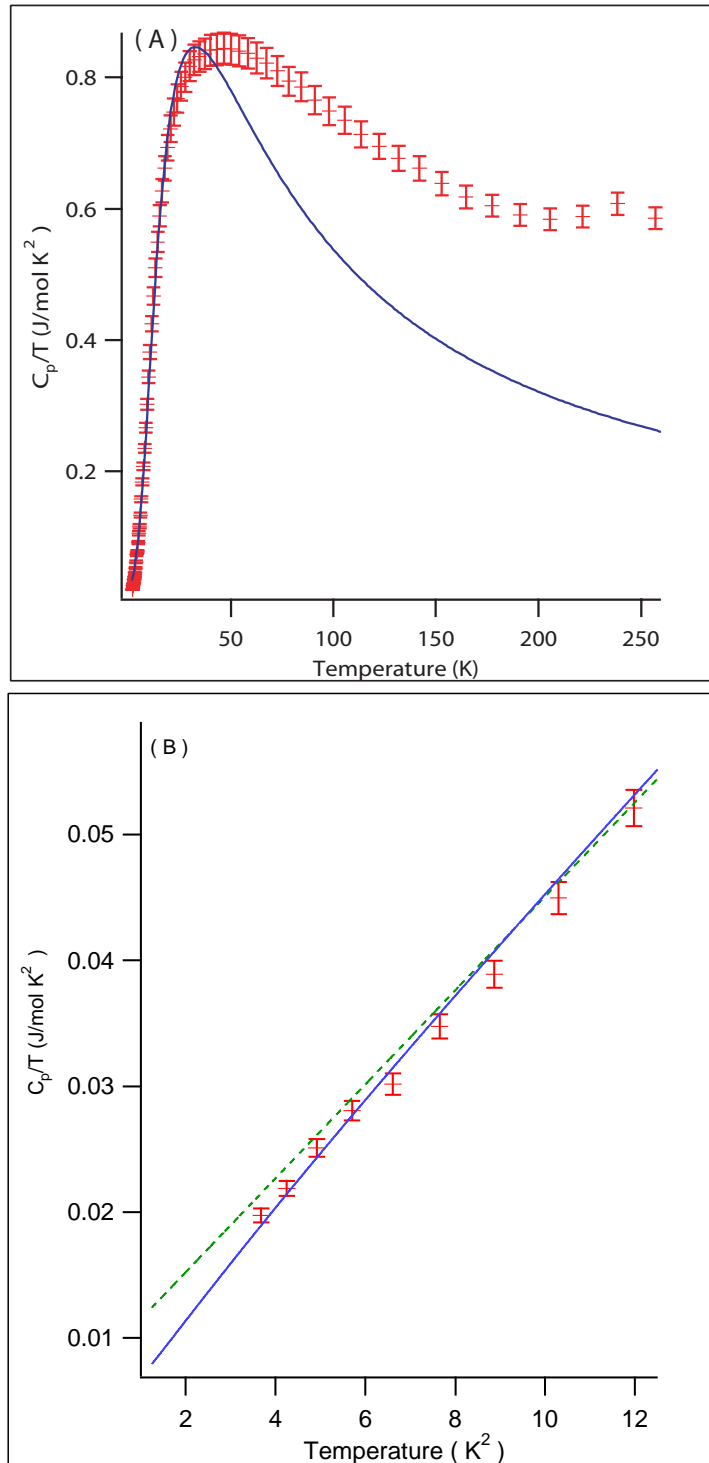
Figure 3.9: A) 6.5% Mn:CdSe Cp/T at 0T (+) and theoretical fit to electronic, magnetic, and lattice contributions (line). B) Heat capacity (Cp/T) for 6.5 % Mn:CdSe (+) and fit to eqn 3.6 including the presence (solid) and absence (dashed) of the magnetic contribution.

Estimating the exchange stiffness using the Tc calculated from the magnetization data [73]

$$D_{calc} = \frac{6k_B T_c}{(2S+1)(6\pi^2 N_{Mn})^{2/3}} \qquad (3.7)$$

where S is the spin, k_B is the Boltzmann constant, N_{Mn} is the Mn concentration, and T_c is the observed Curie temperature. Solving eqn 3.7 yields a value for $D_{calc} = 4.877 \times 10^{-30}$ erg·cm^2. As a comparison, using the calculated magnetic heat capacity, the exchange stiffness can be calculated from the magnetic contribution to the heat capacity (C_m),

$$C_m = \delta T^{3/2} + \delta_o = 0.113 V k_B (\frac{k_B T}{D})^{3/2} - 0.17 V k_B (\frac{E_o}{D})^{3/2} \qquad (3.8)$$

where V, the molar volume, D, the exchange stiffness which is a measure of the spin coupling, and E_o, the energy gap below which spin-waves cannot be supported. The calculated exchange stiffness from C_M for the 4.0 nm Mn:CdSe sample is $D = 1.672 \times 10^{-30}$ erg·cm^2, which is well within experimental error of the Tc derived value thus providing support for the interpretation of the Cp/T data in figure 3.9.

Using D, the energy gap can be solved for from the C_M data, yielding a value for E_o=1.06 K, allowing the wavevector for the spin wave to be solved. Using the value of E and D yields a spin wave size of 6.7 nm (based on C_M). Based on the experimental Tc for the 4 nm nanocrystal a ferromagnetic gap of 8.71 K is calculated from the energy gap and wavevector relation. All of these values are in surprisingly good agreement with the observed 4 nm particle size and indicates that the magnetic interactions occur over the entire volume of the nanocrystal consistent with the onset of a ferromagnetic spin-wave.

3.3.3   Conclusion

The observation of ferromagnetism in un-annealed samples of 4nm Mn:CdSe (6.5 %) is fully explained using a carrier induced VCA-RKKY model. The level of agreement between heat capacity and magnetic susceptibility supports the conclusion of intrinsic carriers which induce stable long range magnetic exchange below Tc. The presence of carriers is supported by the Cp data, although infrared spectral evidence could not be obtained on the nanocrystal samples, as previously observed. Understanding whether the carriers arise from the synthetic method or are present ina all nanocrystalline samples is underway. This gives rise to Bloch law behavior in the heat capacity, allowing an accurate prediction of the particle domain

size, magnetic entropy, and the Tc's. The presence of similar high carriers density (10^{20} cm^{-3}) in both doped and undoped nanocrystal samples indicate the carriers are intrinsic, rather than arising from Mn(II) substitution. This opens up new potentials in the design of spintronic materials, where tunable FM exchange in nanocrystalline materials may be readily achievable if the carrier concentrations can be controlled.

CHAPTER 4

6.5% Mn:CdSe Magnetic Circular Dichroism

The characterization of materials such as Mn:CdSSe for spintronics have received much attention as a result of the advancement in synthetic and theoretical techniques. Four nanometer (6.5 %) Mn:CdSSe was synthesized and characterized using MCD. A magnetic groundstate is observed upon doping Mn into CdSSe nanocrystals.

4.1 Introduction

The introduction of Mn(II) into nonmagnetic nanocrystalline CdSSe leads to an onset of magnetic interactions at low temperature. The theoretical explanation for this has been controversial for some time since Mn-Se-Mn interactions are antiferromagnetic. Much of the confusion can be traced to a successful doping strategies for nanocrystalline semiconductors. In a recent publication we observed the onset of spin-wave behavior which proves the presence of ferromagnetic interactions in lyothermally prepared CdSSe nanocrystals prepared by our single source method[78]. Ferromagnetic exchange in 1% Mn:CdSe is observed below 50 K and readily explained by a virtual crystal RKKY model which requires free carriers be present. For exchange coupling between carriers and the local magnetic ions to occur, an overlap between the valence band and the manganese d-levels must exist via a p-d exchange ($N_o\beta$) interaction. The splitting of the valence band and p-d exchange interaction leads to both a Zeeman splitting and exchange favorable for long range interaction between the Mn and hole carriers. While the p-d exchange can be theoretically postulated, evidence of the exchange interactions is directly observable under circularly polarized, magnetic field dependent absorption spectroscopy; often referred to as magnetic circular dichroism (MCD). The MCD data provides a direct measure of the Zeeman splitting, of the excitonic levels,[79, 7, 22] and contributions for paramagnetic ions through C term via fitting.

In CdSSe we expect only an A- term, while for the MnCdSSe A and C term will play a major role. In a quantum confined system the splitting of the valence states is pronounced especially in the strongly confined regime as a result of electrostatic interaction between the cation and anion relating their non-spherical crystal field interaction. In a CdSSe homogeneous alloy the symmetry is lowered from C_{6v}^4 to C'_{3v} by loss of the S_6 symmetry. The crystal field levels in Mn:CdSSe are also influenced by the Mn levels if p-d exchange and length of exchange coupling is present.

The allowed circularly polarized transitions split by the lowered symmetry are shown in figure 4.1. The magnetic field results in the split spinor levels which will exhibit a field dependent splitting. In the MCD, the principal observed transition will be the E_1 transition since it follows the conservation of angular momentum and requires no spin flip. The E_2 and E_3 transitions will be thermally activated and therefore the polarization will be lost due to a spinflip.

4.2   Synthesis

In this paper we report field dependent MCD measurements on 3.5 nm CdSSe and 4.0 nm 6.5% Mn:CdSSe nanoparticles with a 5 % size distribution as estimated from TEM. The fit of the XRD confirms the size of the particle in addition to the wurtzite structure. Inductively coupled plasma atomic emission spectrometry (ICP-AES) was used to calculate the ratio of manganese to cadmium resulting in $\sim$ 6.5%. The materials are prepared by the method used by Magana et al[69, 78] utilizing $[Cd_{10}Se_4(SPh)_{16}]$ and $MnCl_2$ in hexadecylamine (HDA). To ensure no free Mn is present in the prepared nanocrystals the surfaces are stripped using a series of chloroform/methanol precipitation steps, followed by 70°C pyridine/hexane precipitation[69]. Although it has been suggested that pyridine may not remove all Mn(II), we observe no change in manganese concentration following the second stripping step suggesting its adequate for removing Mn(II). For the MCD measurements, thin films are prepared by dissolving the sample in pyridine and adding with N-(3-(trimethoxisilyl)-propyl)EthyleneDiamine. The sample was allowed to condense into a cross-linked amorphous organosilane glass. The films are prepared as $\sim$ 10 μM concentrations. The MCD was measured using an Oxford 7 T optical magnet attached to a Jasco 810 circular dichroism spectrometer (300- 4 K).
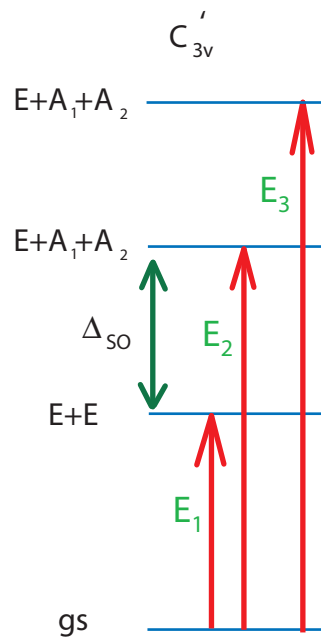
Figure 4.1: Allowed transitions in C_{3v} lowered wurtzite structure. The symmetry allowed E_1, E_2, and E_3 continue to be allowed under circularly polarized excitation and under a magnetic field.

4.3 Discussion

The optical data for linear and circular absorption for CdSSe Mn:CdSSe are shown in figure 4.3. Comparison of the linear and MCD data allow the individual transitions to be identified (E_1, E_2, and E_3) The MCD spectra can be fit to the differential of a pseudo-Voigt function to allow thermal and distribution contributions to the MCD signature to be included as shown in Fig 4.3B and C for the 7.0 T (4.2 K) MCD spectra.

$$f'(E) = A[(1 - a_1)e^{-ln(2)(\frac{E-E_o}{FWHM})^2} + \frac{a_1}{1 + (\frac{E-E_o}{FWHM})^2}] \tag{4.1}$$

where A is the amplitude, a_1 is the Lorentzian to Gaussian ratio, FWHM is the Gaussian full width half maximum, and E_o is the energy maximum.

Using the field dependent spectra, the splitting of the E_1 and E_2 states can be differentiated. The splitting for CdSSe and MnCdSSe is 370 and 240 meV, respectively as observed in figure 4.4C and D. This is the average splitting of the crystal field and spin orbit combined. MnCdSSe is the only one that is field dependent which decreases with increasing field. The observation of the two states in Mn:CdSSe can be better observed in the spectra of the full width half maximum of the Mn:CdSSe. As a function of temperature the FWHM decreases with increasing temperature signifying that there is another state. The state disappears with temperatures above 40 K. Using the FWHM one can determine the Zeeman splitting since the increase is due to the change in the splitting of the states. As observed the FWHM shows an increase of 65 meV which is the Zeeman increase with the addition of Mn. This value is much larger than that previously 9 meV observed for a 1 % sample[80] and Zeeman shift of 10 meV in 5% Mn:CdSe quantum well[81].

4.3.1 Electron phonon coupling

The temperature dependent energy and intensity of the different excitons contain information about the degree of electron-phonon coupling in the Mn:CdSSe and CdSSe systems. The phonons allow the lowest energy E_1 and E_2 levels to equilibrate at room temperature. As observed in figure 4.4 the first exciton for CdSSe decreases with increasing temperature. For the case of the Mn:CdSSe, there is little temperature dependence as observed in figure 4.4B. For a wurtzite structure the available phonons for coupling to the exciton include three optical (A_1, E_1, E_2) and 2 acoustic (A_1, E_1) modes.
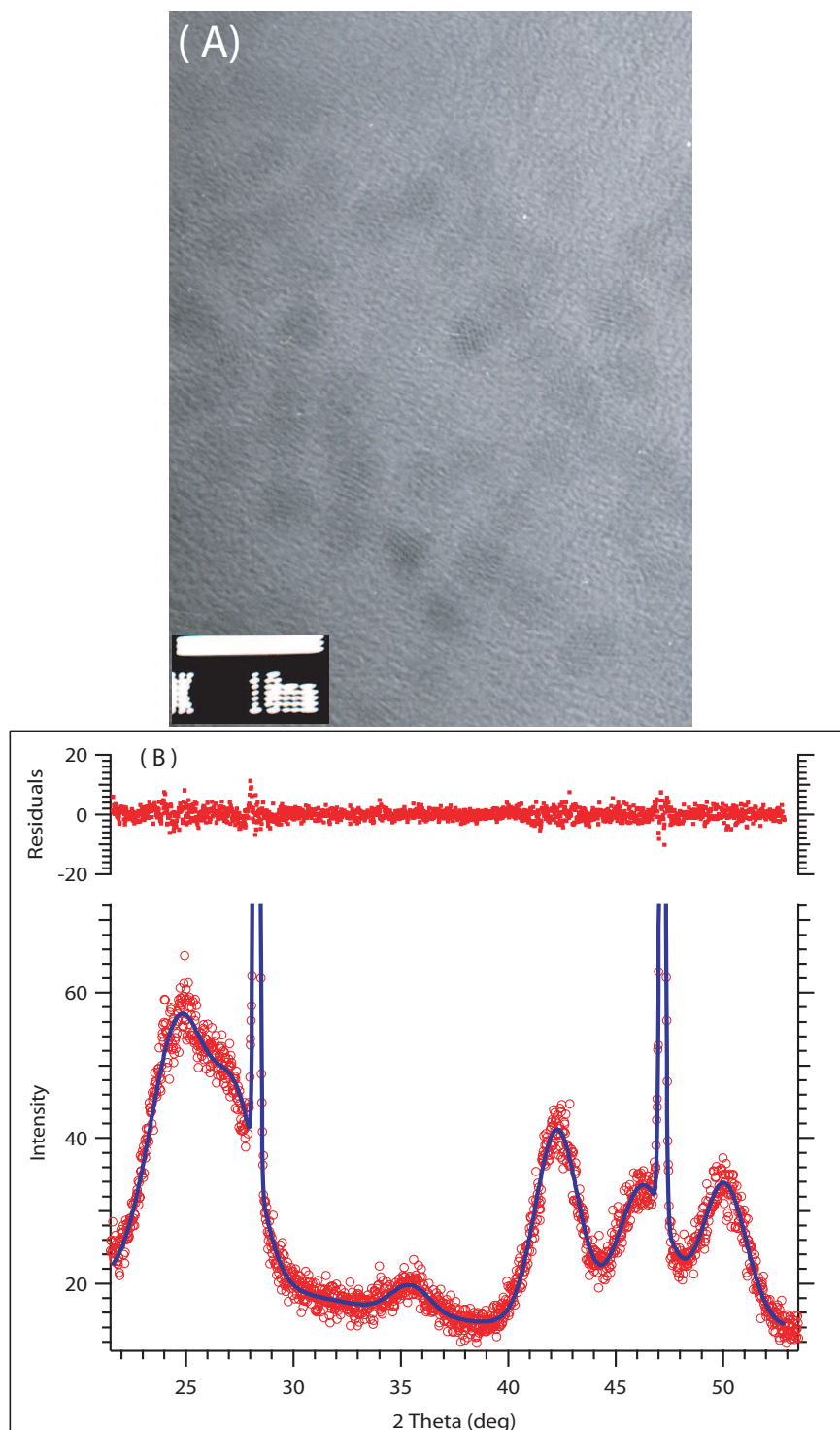
Figure 4.2: The TEM shows an average of 3.8 nm. XRD of the wurtzite MnCdSSe where the a axis is equal to 4.274 $\mathring{A}$ and Scherrer size of 3.9 nm calculated by fitting the spectrum to gaussian functions and calibrating to silicon.
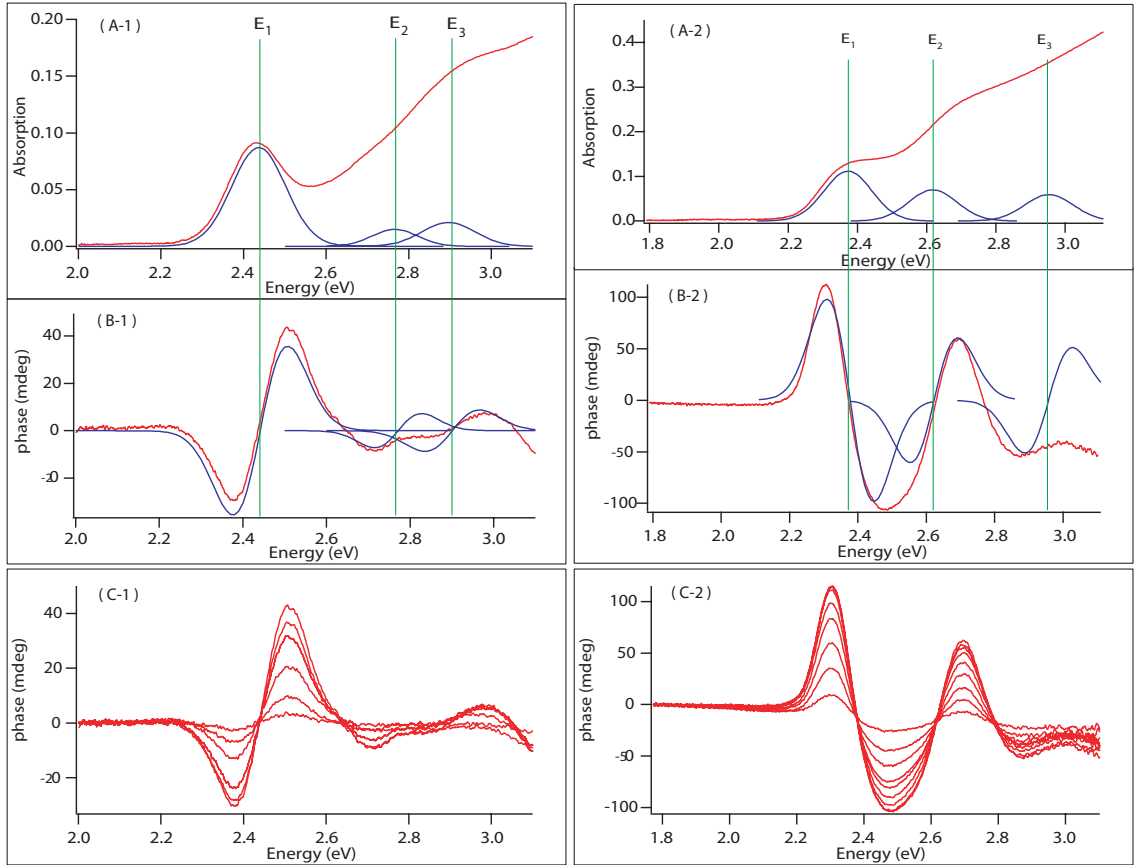
Figure 4.3: A) Absorption and MCD transitions of CdSSe (1) and 6 % Mn:CdSSe (2) in toluene as a solvent. The three main transitions are labeled E_1, E_2, and E_3. B) 4.7 K MCD of CdSSe (1) and Mn:CdSSe (2) at 7.0 T with the Voigt fit components. C) CdSSe (1) at 4.2 K with a field of 0.5, 1.5, 3, 4, 5, 6, and 7 T. Mn:CdSSe (2) MCD at 4.2 K of 0.4, 1.0, 1.6, 2.4, 3.0, 4.0, 5.0, 6.0, 7.0 T.

Assuming a classical phonon bath an approximation can be used to describe the electron phonon coupling for the exciton following that of O'Donnell et al[82],

$$E_g = E_g(0) - A < E_{phonon} > (Coth(\frac{< E_{phonon} >}{2k_B T}) - 1) \quad (4.2)$$

where the two terms are included E_o, the zero K bandgap, $< E_{phonon} >$, the phonon energy for the average phonon frequency, and A, a normalization constant. When the temperature data is fit for CdSSe using equation 4.2 the average phonon involved in the electron phonon coupling has a temperature of 115 K. This temperature corresponds to the average energy between the E_2 and A_1 phonons subsequently they are the primary contributors. This suggests a state that does not have enough thermal energy to be influenced by the phonons involved.

From the Zeeman splitting (A-term) of the MCD, $N_o\beta$ (p-d) and $N_o\alpha$ (s-d) exchange constant can be derived[16]

$$\Delta E = E_{1-} - E_{1+} = (\beta - \alpha)N_o x < S_z > \quad (4.3)$$

where β is the valence band exchange, α is the conduction band exchange, No is the number of unit cells per volume, x is the manganese mole fraction, and $< S_z >$ is the manganese spin (s=5/2). Using the splitting in E_1 $(\beta - \alpha)$=1.07 eV which is in agreement with the reported exchange constant for Mn:CdTe bulk [16].

4.4 Magneto-optical

Unlike the cobalt charge transfer transitions typically observed for the cobalt in CdSe, the manganese transitions lie at the valence band inhibiting their observation. The effects observe are those expected for a p-d exchange between the exciton and the magnetic Mn(II) ions incorporated.

4.4.1 Properties of CdSSe

Inspection of the temperature and magnetic field dependent MCD for the CdSSe and Mn:CdSSe samples fit to eqn 4.1 yield the change in phase intensity as a function of temperature and field.
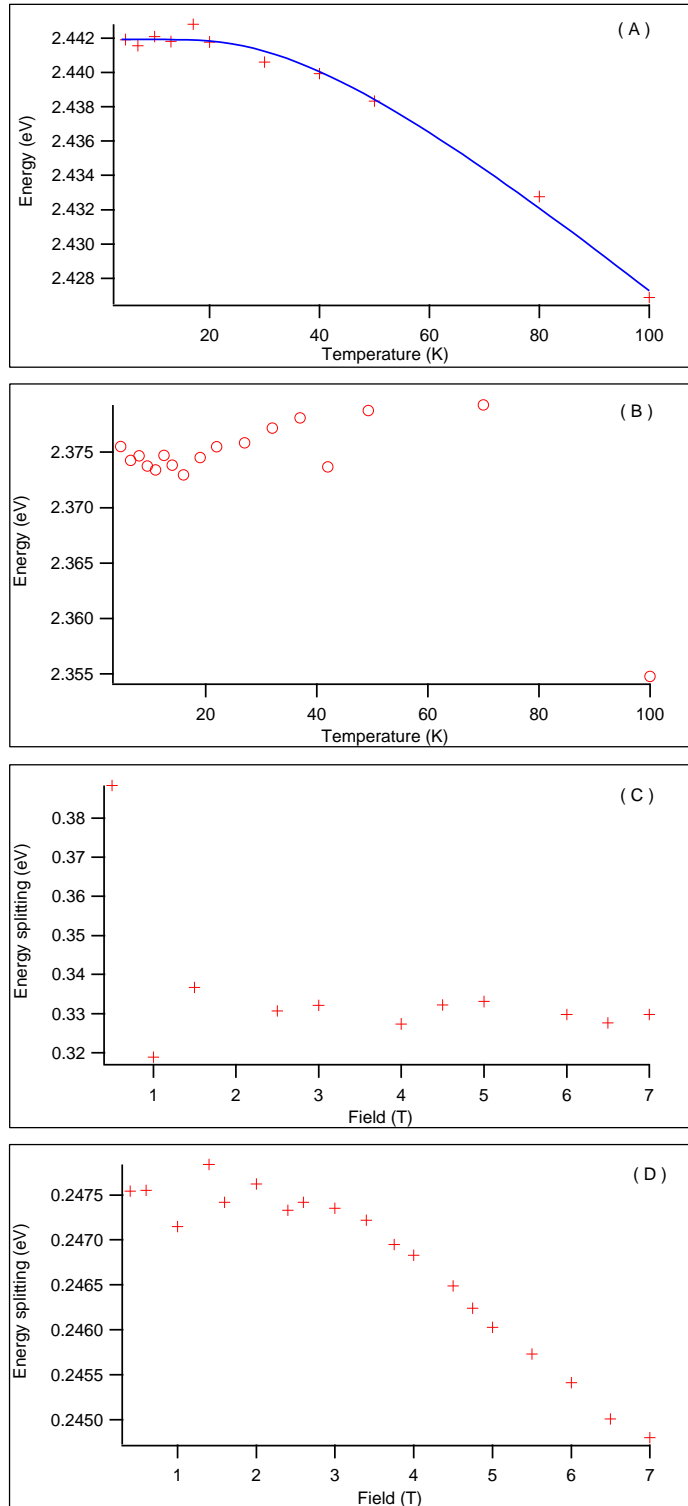
Figure 4.4: A) Temperature dependent E_1 exciton at 1.0 T of CdSSe. B) Temperature dependent E_1 exciton at 1.0 T of Mn:CdSSe. C) Energy difference between the first two excitons of CdSSe as a function of field. D) Energy difference between the first two excitons of MnCdSSe as a function of field .
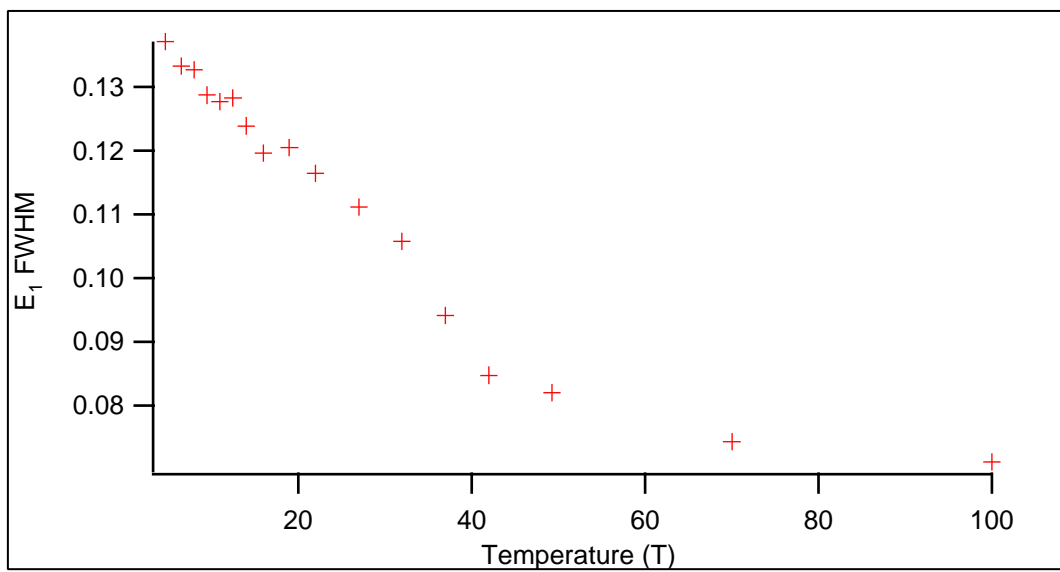
Figure 4.5: Temperature dependent FWHM of MnCdSSe at 0.5 T.
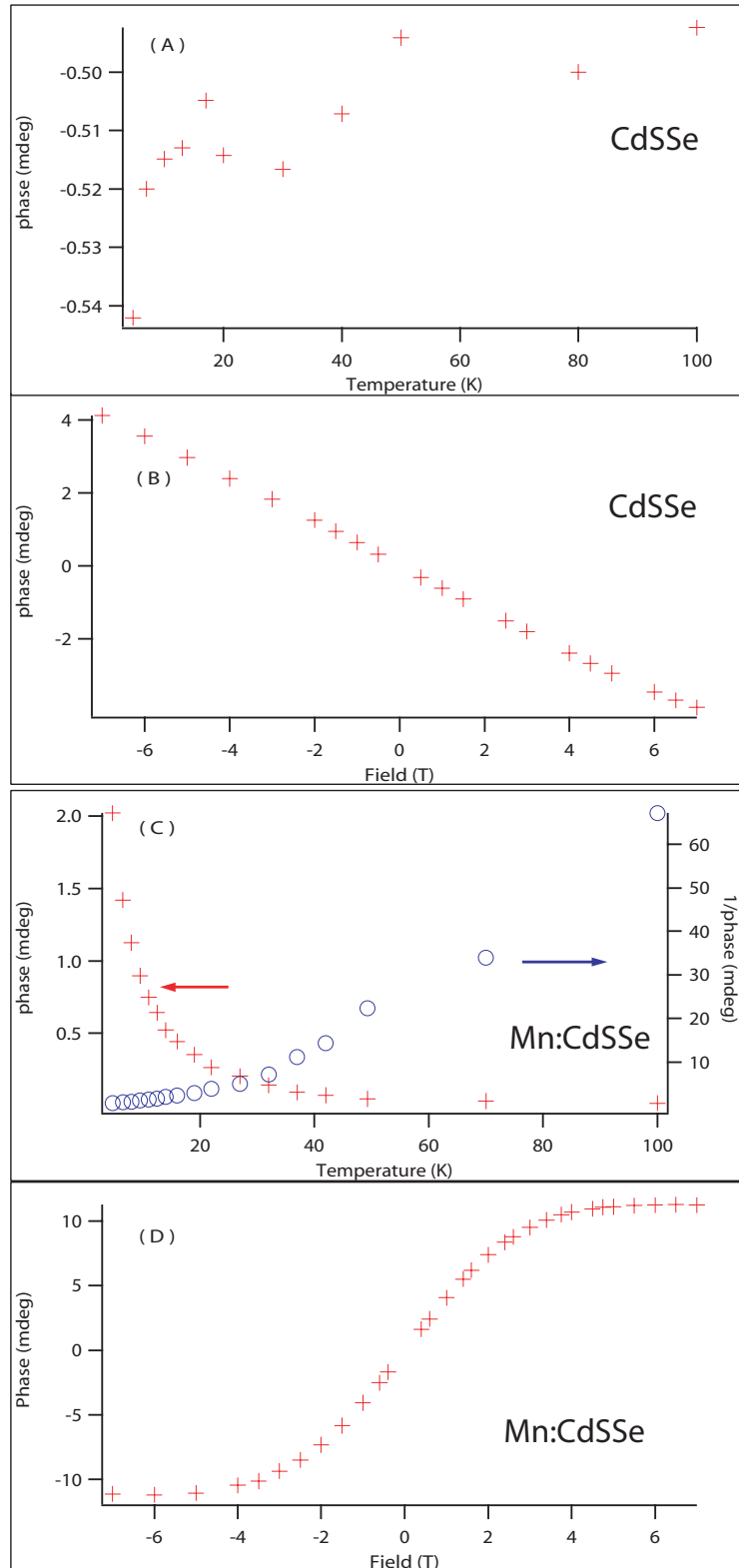
Figure 4.6: A) MCD spectra intensity of 3.5 nm CdSSe for E_1 transition taken at 1.0 T. B) Magnetic field dependent CdSSe at 4.7 K. C) Intensity of 3.9 nm Mn:CdSSe for E_1 transition taken at 0.5 T. B) Magnetic field dependent Mn:CdSSe at 4.7 K.
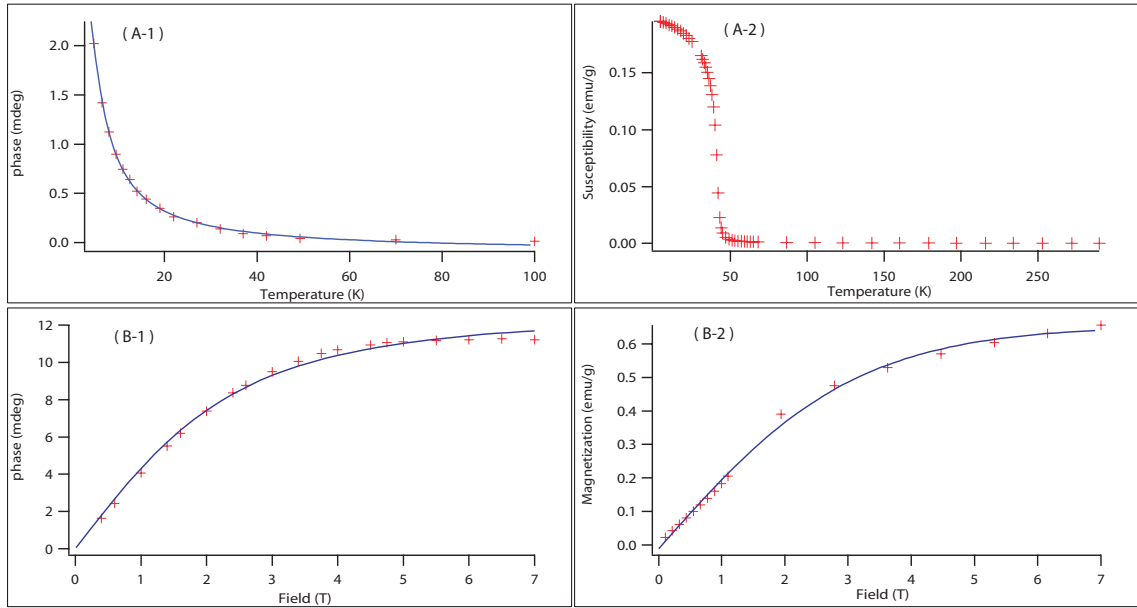
Figure 4.7: A) Temperature dependent phase intensity (1) of Mn:CdSSe at 0.5 T (+) and fit to the Brillouin function (solid). Magnetic susceptibility (2) of Mn:CdSSe at 0.05T under field cooled conditions. B) Field dependent phase intensity (1) of Mn:CdSSe at 4.7 K (+) and fit to the Brillouin magnetization function. Magnetization at 2.0 K for Mn:CdSSe and fit to Brillouin function.

The CdSSe (fig. 4.6A) is found to be constant at 0.5 and 1 T as a function of temperature and linear as a function of field as expected for a diamagnetic material. When Mn is added to the CdSSe p-d exchange is expected to change the nature of the transitions. This is observed in the intensity of the MCD plot for the E_1 exciton (Fig. 4.7). At 0.5 T the temperature dependence of the first CdSSe exciton follows a 1/T as predicted for the C-Term when a paramagnetic ion is incorporated into the CdSSe lattice (Fig. 4.7A-1), implying the existent coupling of the groundstate to the Mn states. When the phase is plotted as 1/phase the high temperature exchange can be fit where a 2.0 meV exchange energy is calculated from the slope intercept. The positive exchange gives the same information as expected from a Curie-Weiss plot where ferromagnetic exchange is observed in a positive intercept. If Mn resides at the surface no influence on the MCD signal is expected. This is perhaps strong evidence for successful Mn incorporation by the single source route. The magnetic susceptibility only shows information about the transition at 41 K where the ferromagnetic exchange begins in the system (Fig. 4.7A-2). This can be further observed with the field dependent spectra at 4.7 K where the E_1 intensity saturates above 3.0 T compared to the 4.0 T in the magnetization experiments.

To better understand the interactions in the Mn:CdSe spectra the data is fit to a Brillouin function as shown in figure 4.7B, using the temperature dependent Brillouin expression.

$$B_j(\eta) = \frac{2j+1}{2j} Coth\left(\frac{(2j+1)\eta}{2j}\right) - \frac{1}{2j} Coth\left(\frac{\eta}{2j}\right) \qquad (4.4a)$$

$$\eta = \frac{gj\mu_B H}{k_B(t)} \qquad (4.4b)$$

$$M = Ngj\mu_B B_j(\eta) \qquad (4.4c)$$

$$\chi = M/H \qquad (4.4d)$$

, where N is the molar volume, j is the spin and angular momentum, μ_B is the Bohr magneton, g is the landé splitting factor, and H is the magnetic field. When the susceptibility function is fit (fig. 4.7A) to the intensity of the MnCdSSe MCD data, the ordering temperature can be calculated to be 2.5 K. Using equation 4.4c the field dependent data can be fit to obtain the spin for the CdSSe exciton by fitting the MnCdSSe intensity of the E_1 exciton (fig. 4.7B). If Mn(II) is couple to exciton the spin should reflect a S=5/2 spin. The spin fits to a value of S= 2.1, which is within expected error of the Mn spin (S=5/2). The surprising spin value

for the exciton strongly implies state coupling exists between the d-levels of Mn and the s and p levels of the CdSe by a p-d exchange mechanism. In the magnetization plot the spin is fit using eqn 4.4 where a g value of 2 is used and the spin fits to 1.97.

4.5 conclusion

Evidence of the phonon assisted absorption is observed in the temperature dependent band gap. The thermalization of the spins destroy the Zeeman increase observed in the FWHM of the first exciton of 4 nm 6.5 % MnCdSSe. The crystal field and spin orbit energies as calculated using the fit of the MCD to a Voigt function. The difference between the Mn:CdSSe and CdSSe for the same size is in the magnitude of the crystal field concluding an exchange interaction between the Mn levels and the valence band of CdSSe.

CHAPTER 5

CdSSe Field Dependent Magneto-photoluminescence

Alloy formation can strongly perturb the excited state dynamics of a nanocrystalline semiconductor via symmetry breaking resulting in loss of the forbidden character of the excitonic transitions and subsequent state mixing. Evidence of state mixing is observed in the field dependent polarization and energy shifts of the circular polarized photoluminescence for CdSSe probed by Zeeman spectroscopy. Mixing of states results in loss of spin polarization for the CdSSe alloy. The mixing of the exciton levels is probed by circularly polarized photoluminescence in a magnetic field (0-31T) and fit using a second order perturbation of Zeeman theory to account for the formation of a self-trapped exciton polaron.

5.1   Introduction

In nanocrystalline CdSe prepared by colloidal methods, evidence of a spin flip transition has been observed in the magneto photoluminescence data resulting in loss of spin coherence. While the data fits to the spin flip model, the observed Zeeman fitting is poorly fit by the first order Zeeman expression, although an attempt to model the observed state splitting in terms of random nanocrystal orientation and exciton state mixing of the 'Dark' (J = 2) and 'Bright' (J=1) excitons has qualitatively reproduced the data [83, 84, 85, 86, 87, 88, 89]. A plausible explanation is the presence of donor states in chemically grown nanocrystals arising from vacancies, unintentional incorporation of impurities, or reconstruction, which are known to play a critical role in the photoluminescence properties. In fact, trapping of the exciton at donor states with subsequent excitonic polaron formation has been experimentally observed.

In an attempt to sort out the potential contributions arising from impurity states, we have probed the magnetic field dependent exciton splitting behavior for an intentional

homogeneous nanocrystalline alloy, CdSSe. Use of a homogenous alloy allows intentional acceptor states to be incorporated into the nanocrystal. The MPL data for the CdSSe alloy can be explicitly fit using a second order perturbation to account for state mixing. In addition, the symmetry breaking of the spin levels can be treated using double group symmetry allowing correlation between the intensity, energy, and polarization behavior for this intentional alloy. The lowered symmetry of the alloy reduces the Δ_{bd} which allows mixing to arise between states. Intriguingly, as the sulfur content is increased the energy of separation between the bright and the formally dark exciton is reduced, suggesting that level reversal may occur.

An interesting question is the impact on the exciton splitting by the formation of a CdSSe alloy. The CdSSe alloy is an example of a solid solution with the S distributed statistically throughout the lattice. This results in changes of E_g with minimal perturbation of the Brillouin zone [7, 90]. The exciton model and recombination dynamics however will be influenced by the change in symmetry that arises within the Bravais cell. In a magneto-photoluminescence experiment, the changes in the exciton splitting and the presence of state mixing can be directly followed by analyzing the change in the spinor energies, and the polarization intensity ratio of the right and left circular polarized emission as a function of magnetic field. State mixing presents itself in the loss of polarization integrity, requiring a more complex fitting to account for the presence of states that are thermally equilibrated. A second order Zeeman expression coupled to independent contributions for the two lowest lying excitons in CdSSe allow the projection of the band to properly by interpreted.

5.2 Synthesis

Magnetophotoluminescence (MPL) studies were carried out on $\sim 10~\mu M$ NC CdSSe samples doped at $4 \pm 1~\%$ S (3.0 nm diameter CdSSe) and $8 \pm 1\%$ S (3.2 nm diameter CdSSe) based on X-ray fluorescence spectroscopy. TEM analysis shows a 5% size distribution, which is confirmed by the narrow PL FWHM (70 meV). The nanocrystals were embedded in an amorphous silane glass generated by dissolving the NC-CdSSe in pyridine, adding N-(3-(trimethoxisilyl)-propyl)EthyleneDiamine, and allowing the sample to condense for 12h. The materials were prepared as homogeneous alloys by a modification of the method used by Cumberland, et al utilizing $Li_2[Cd_{10}Se_4(SPh)_{16}]$.[52]
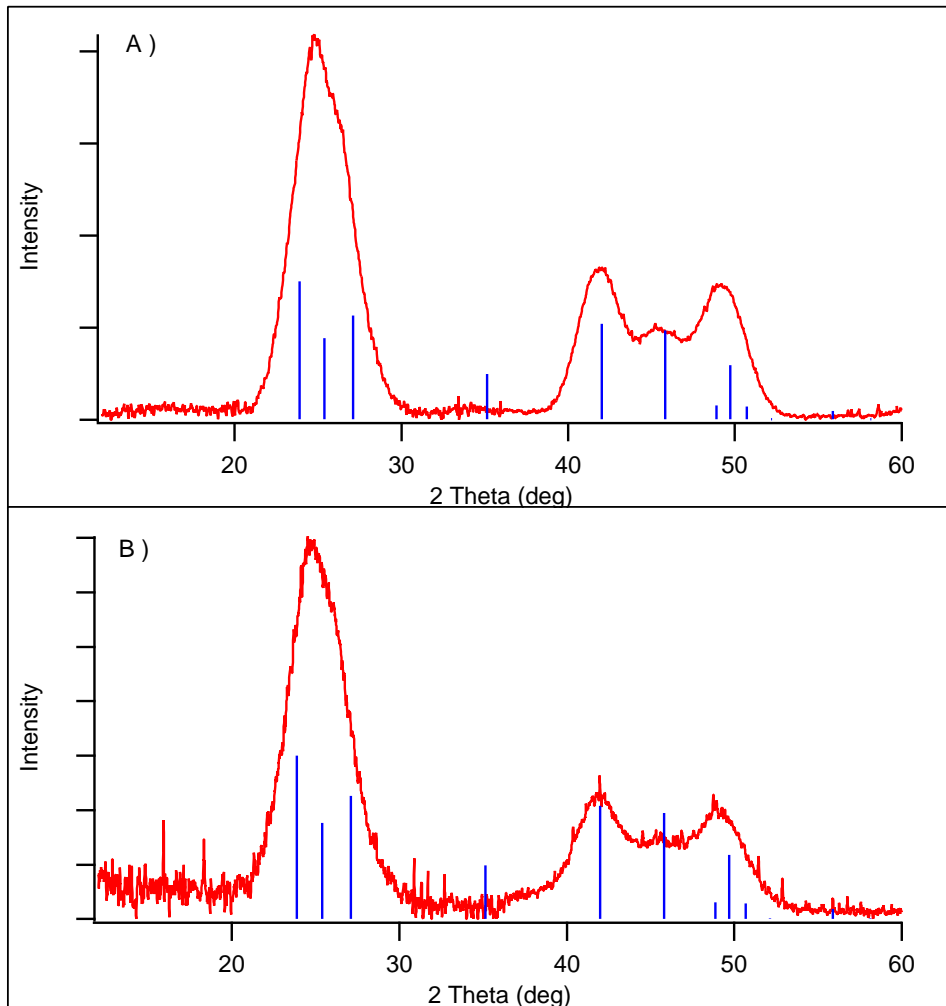
Figure 5.1: XRD of 4% (A) and 8% (B) S CdSe alloy. TEM of the 8% sample. The a lattice constant was fit giving a value of 4.31 and 4.30 $\mathring{A}$ for the 4% and 8% sulfur concentrations, respectively.

The lower sulfur concentration was achieved by allowing partial decomposition of thiophenol during the reaction, while the higher concentration requires elemental sulfur addition[91, 80]. The CdSSe nanocrystals are spherical and exhibit wurtzite symmetry based upon X-ray diffraction (Fig. 5.1A,B) and TEM (Fig. 5.1C) measurements.

MPL experiments were performed at the National High Magnetic Field Laboratory (NHFML-FSU) using an Ar+ ion laser (70 μW @ 458 nm) coupled through a UV fiber optic into a Janis cryostat (4.2-300 K). The cryostat was placed into the 31 T resistive magnet (0 - 31 T) to allow field dependent photoluminescence to be measured. Circularly polarized excitation was generated using a plastic polarizer and a quarter wave plate mounted inside the cryostat in front of the sample. Right and left circularly polarized spectra were collected with a fixed circular polarizer by measuring -31T to 31 T for simplicity in data collection. Circular polarized photoluminescence was collected on a separate fiber coupled to a one-meter monochromator (600 g/mm) using a Princeton Instruments LN$_2$ cooled CCD (512 X 1024 pixels).

5.3   Discussion and Conclusion

In Figure 5.2A, we plot the observed spectral shift in PL for σ^+ and σ^- polarized spectra between 0 T and 31 T for the two doping levels in CdSSe. In a nanocrystalline semiconductor, the electronic properties are expected to exhibit classical Brillouin behavior as a function of magnetic field. This allows the experimental data to be fit to a Langevin function by taking into account the random orientation of the nanocrystals relative to the orientation of the applied field [85] and by explicitly expressing two independent J states (labeled as a and b)to allow mixing if Δ_{bd} is small. While independent states were not previously considered for nanocrystalline CdSe MPL data since the J=2 state is forbidden, the inclusion of independent states allows the loss of forbbiddenness to be assessed arising from mixing, where the intensities will be made up of I$_+^a$/I$_-^b$ (σ^-) and I$_-^a$/I$_+^b$ (σ^+), where I^b is the formally dark J=2 state. In the fit, the intensity is relative to the a - state, which is assumed to dominate the intensity contribution and dictate the polarization [37].

$$
\begin{aligned}
I_{\mp}(cos\theta) = &((1 \pm cos\theta)^2 e^{\frac{g\mu_B Hcos\theta}{2k_B T}} + \\
&(1 \mp cos\theta)^2 e^{-\frac{g\mu_B Hcos\theta}{2k_B T}})/(e^{\frac{g\mu_B Hcos\theta}{2k_B T}} + e^{-\frac{g\mu_B Hcos\theta}{2k_B T}})
\end{aligned}
\tag{5.1}
$$
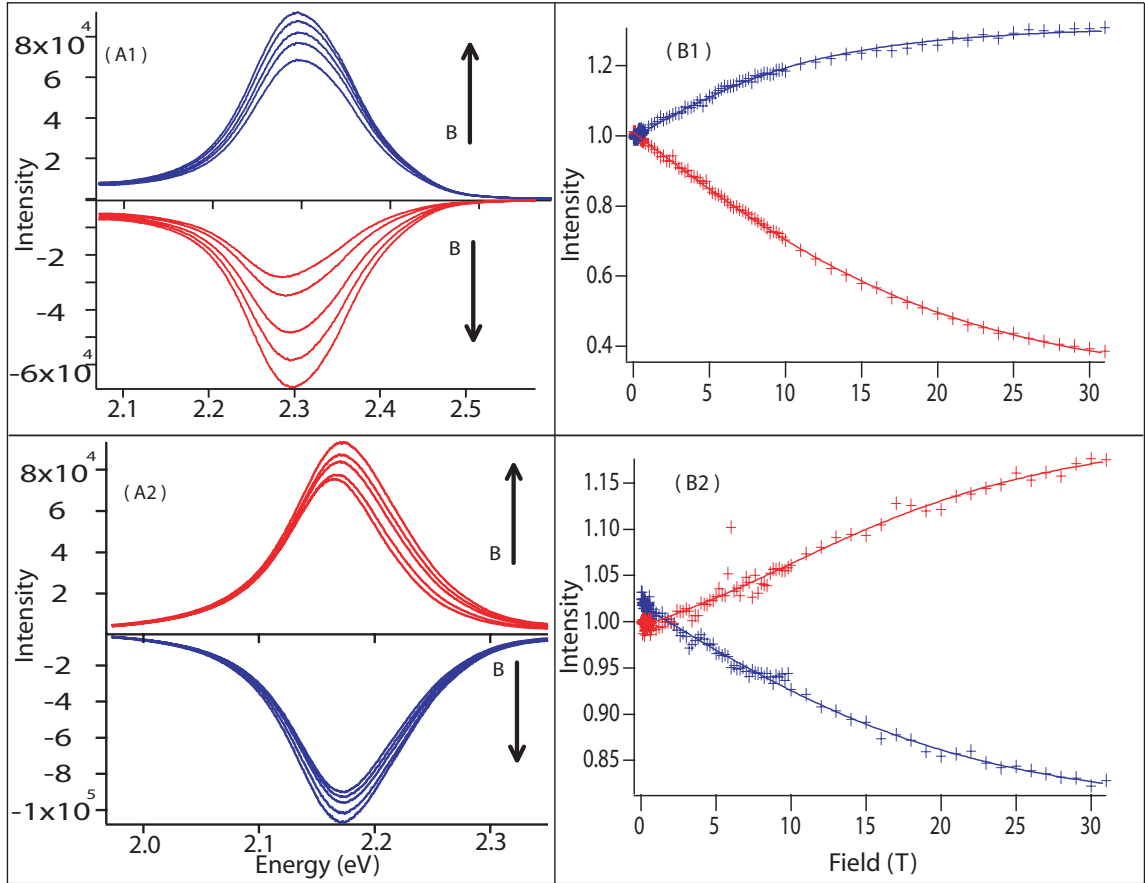
Figure 5.2: A)(CdSe 4% S (1), CdSSe 8 % S (2)) Circularly polarized photoluminescence (σ^- (positive), σ^+ (negative)) taken at 4.2 K for 0.01, 5, 10, 20 and 31T. B)(CdSe (1), CdSSe (2)) Circularly polarized photoluminescence intensity data and two state contribution fit (σ^- (solid), σ^+ (open)) taken at 4.2 K.

The g value is the exciton polarization dependent g value, H is the field and $\cos\theta$ is the dipole angle with respect to the field direction. The expression allows state mixing to occur with loss of spin polarization by a spin flip process. The fit to the data is shown in 5.2B and fits the data quantitatively. Attempts to fit the intensity data to a single emitting state as perviously described fails to fit the experimental data.

The inclusion of the second state to fit the MPL data suggests loss of the dark exciton character through a loss of local Brillouin zone symmetry by formation of the alloy with subsequent loss of J=2 character. It is known that the formation of a solid-solution CdSSe alloy can result in a lowering of the symmetry from the wurtzite C'_{6v} to a C'_{3v} lattice symmetry in a homogenous alloy, thus relaxing the forbiddeness of the J=2 state. [92, 93] The lowered symmetry would occur along the $< 002 >$ face due to loss of the 6_3 (S_6 in Schoenfliss notation) improper rotation axis. This is the axis involved in exciton recombination in CdSe nanocrystals. By inclusion of the spin orbit terms and projection of the spinor levels (spin states) using double group tables [30, 94, 95], a reversal of the (Γ_9) and (Γ_7) states in C'_{3v} arises (Figure 2). The change in symmetry produces a new set of states labeled Γ_6 ($E'_{1/2}$) and Γ_{4+5} ($E'_{3/2}$), which split under magnetic field by $\sim$ g S μ_BH (first order Zeeman approximation). In the exciton model, figure 5.3B, the lowered symmetry results in the loss of the J=± 2 state character and formation of a new J=$\pm 1^b$ level. The $|1>$ states' behavior is similar to that of the known $|2>$ dark state. If the J=$\pm 1^a$,$\pm 1^b$ states are within k_BT then mixing can arise allowing facile spin depolarization, which would fully describe the requisite inclusion of two discrete levels to fit the intensity data. The possibility of two states with allowed character would explain the saturation in the intensity data for the CdSSe since the states compete for intensity but have opposite spin polarity. The observation of saturation could not be account by a single state.[85]

The presence of two states has a dramatic impact on the intensity and energy levels of the states as a function of field, particularly leading to spin depolarization of the circularly polarized transitions. Intensity of each state depends on the magnitude of Δ_{bd}, since the two states would need to be thermally populated at 4.2K, and the g-value for the state. If we define the four polarized transitions as $(|+1^a>,|+1^b>,|-1^a>,|-1^b>)$, then the g-values and intensities can be extracted from the fit to equation 1. The g-values will not be equivalent when mixing arises between the states and will depend on the magnitude of mixing.
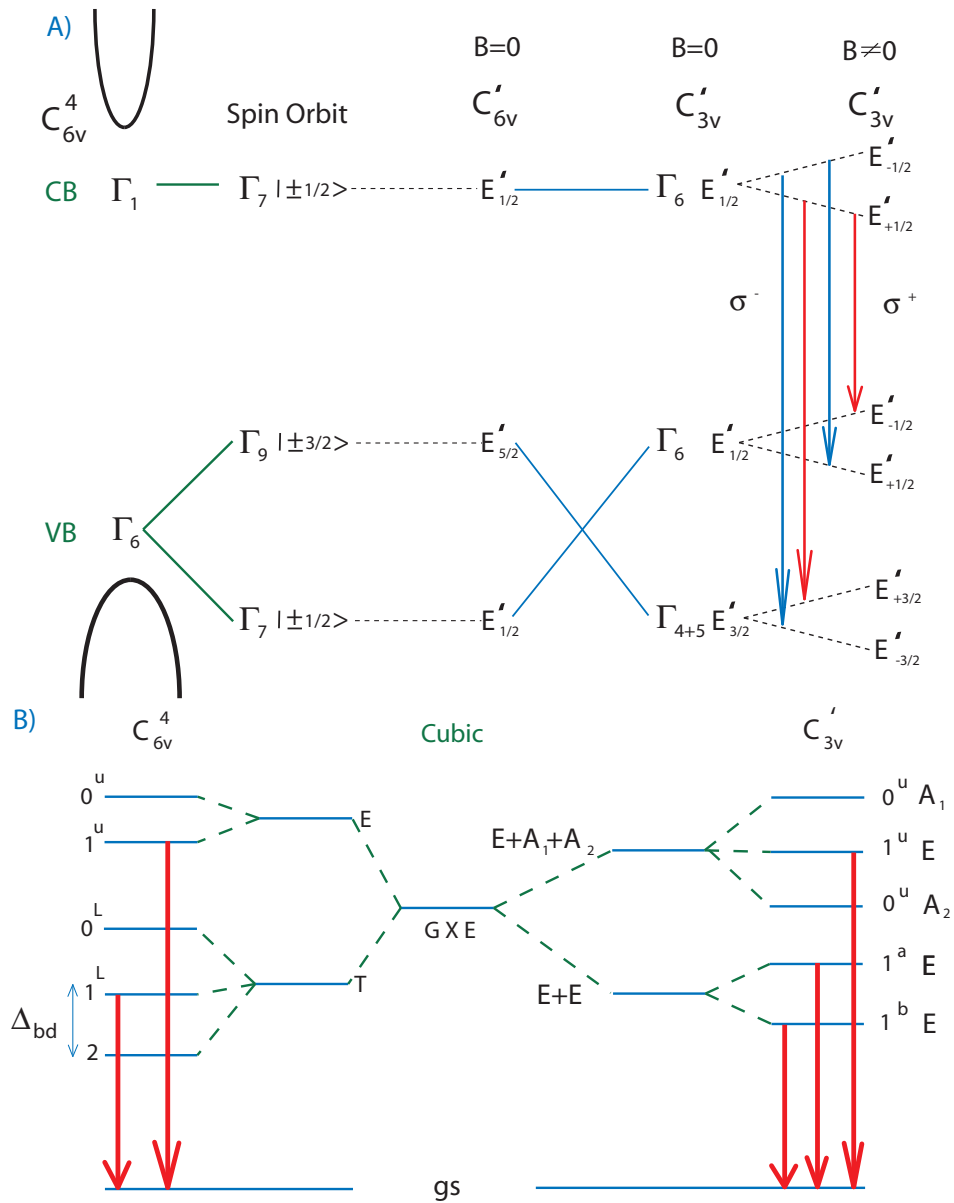
Figure 5.3: A) Band diagram for a wurtzite structure with the spin designations. the double symmetry state character for the C_{6v}'s wurtzite structure symmetry is shown. Reduction of symmetry from a C'_{6v} to a C'_{3v} using double groups probes an inversion of the $E_{5/2}$ and $E_{1/2}$ level. The crystal field Γ_7 is not shown. B) The correlation diagram for the exciton model for a cubic (T_d) to hexagonal (C^4_{6v}) and to a C'_{3v} is shown.

Fitting the intensity data (Fig. 5.2b) for the individual σ^+ and σ^- polarizations assuming a spin of 1/2 yields values for the 4% sulfur sample,where the σ^+ is composed of g = +1.40 ($|+1^a>$), -1.40 ($|+1^b>$) and σ^- is composed of g = -0.76 ($|+1^a>$), +0.24 ($|+1^b>$). The 8% sample gives σ^+ values of g = +0.52 ($|+1^a>$), -0.64 ($|+1^b>$) and σ^- is composed of g = -1.01 ($|+1^a>$), +1.31 ($|+1^b>$). The presence of mixing is most apparent in the larger S content (Figure 5.2B-2), where a crossing of the intensities occurs at low field (2.0 T), with the σ^+ level exhibiting a nearly sigmoidal shape with field supporting a mixing of $|+1^a>$ and $|+1^b>$. State mixing and changes in Δ_{bd} value with increasing S content is a more likely explanation for the observed crossing of energy levels, rather than phonon population at low field as has been suggested previously.[85]

If the loss of dark character is to be believed, then the energy plots (Figure 5.4A) for the CdSSe samples should exhibit a bowing of the trajectory at high field due to state mixing. The bowing will be more extreme in the higher sulfur content sample presumably due to higher degree of state mixing. Inspection of Figure 5.4 shows significant bowing at high field consistent with prediction. Assuming the bowing in the E plot reflects the separation between the $|1>$ exciton levels, the value of (Δ_{bd}) can be extracted by projecting the value at zero field (Fig. 3A), assuming a crossing of the states, yielding a value for Δ_{bd} of 3 meV for the 4% CdSSe sample. This value is close to the theoretical Δ_{bd} value in pure CdSe nanocrystals of 6 meV for 3.0 nm diameter CdSe[85, 89]. As the concentration of S is increased, the value of Δ_{bd} is convoluted by strong mixing and the inversion of the exciton levels. This does not allow the energy splitting to be cleanly extracted suggesting these levels are intimately mixed even at low field.

The two state model generated by loss of dark character in the alloy fits both the intensity and energy trajectories. To fit the field dependent energy of the photoluminescence, E(H), a second order perturbation expression for the Zeeman splitting can be used. The second order Zeeman splitting includes a Landé splitting term, a diamagnetic contribution, and an el-ph coupling term, where

$$E(H) = E_o + g\mu_B SH + DH^2 +$$
$$\alpha(Coth[g\mu_B SH/k_B T] - 1/(g\mu_B SH/k_B T))$$

(5.2)

E_o is the zero Kelvin bandgap, g is the exciton Landé term, S is the exciton spin, H is the magnetic field, D is the diamagnetic contribution due to electron cyclotron resonance, α is the electron-phonon (el-ph) coupling constant, and T is the temperature.
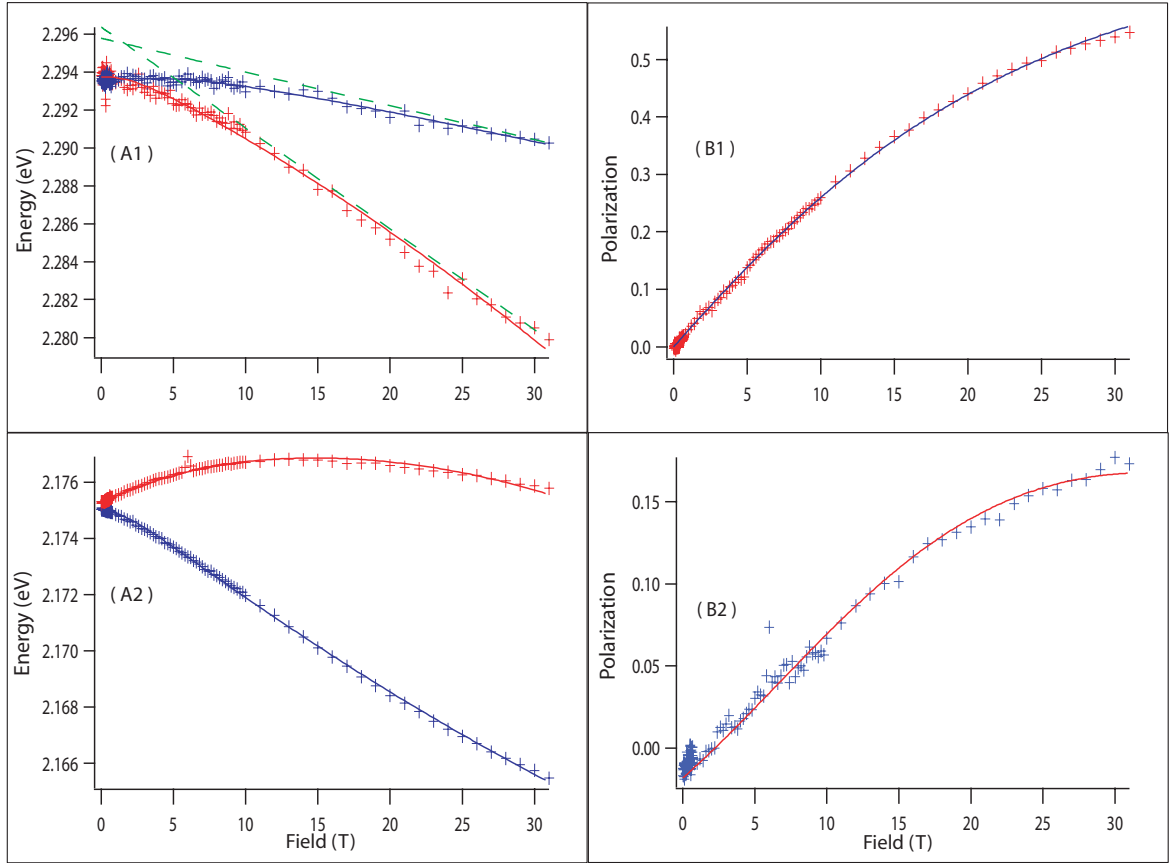
Figure 5.4: A) Photoluminescence energy as a function of polarization and field. This includes the energy fit for 4% (1) and 8% (2) CdSSe samples. The 4 % sample shows the extrapolation of the high field splitting (—) to extract Δ_{bd}. B) Polarization dependence of the intensity and fit for 4% (1) and 8% (2) CdSSe samples.

The magnitude for 4 percent S CdSe is 4.2×10^{-7} eV/T^2 and 8 percent S CdSe is 4.4×10^{-7} eV/T^2. Although a value for CdSe is not available the value compares to 1.6×10^{-7} eV/T^2 of bulk Cu:CdSe[96]

No attempt is made to separate contributions from the different states J=1^a, 1^b due to the lack of resolution in the spectral profile. Since the contribution from the J=1^a is dominant, it will reflect a weighted value and therefore we report only the g$^{\sigma^+}$ and g$^{\sigma^-}$ values without state deconvolution.

In the low sulfur concentration sample, fitting the energy profiles yields a g-value of 1.2 for the σ^- state. The experimentally extracted g-value is consistent with previously reported average g values for pure NC-CdSe[37, 97]. The g-value for the σ^- photoluminescence in 4% CdSSe is 3.2 providing the strongest evidence of mixing between the $|-1>$ and $|+1>$ states at high fields. Mixing of the states depolarizes the $|-1>$ state, where one predicts the g-value for the $|-1>$ state should approach the value for the $|+1^b>$ level if mixing occurs, which has been theoretical predicted to be 4.0, if we assume the J=2 state calculation still applies[98, 37]. While the assumption is flawed, the asymmetry in g-value supports the 2 state model.

In the 8% CdSSe, the g-value for the $|+1>$ photoluminescence state is 3.5 and for the $|-1>$ state a value of 0.98 is extracted. The inversion of the g-value for the 8% sample is surprising, but suggests that an inversion of the $|1^a>$ and $|1^b>$ level must occur resulting in mixing of the $|+1^b>$ with the $|-1^a>$ level; and therefore, the unexpected large value of g for the σ^- state. This observations supports the results observed for the intensity data behavior which indicate a loss of the initial spin value for the lower state, as has been predicted by Ivinchenko[92] for a symmetry broken system.

If a mixing with the $|1^b>$ state occurs, it is expected to also have a dramatic effect on the polarization of the $|1^a>$ state since the spin coherence will be lost due to depopulation of the $|-1^a>$ by $|+1^b>$. A plot of the polarization data is generated by plotting

$$\rho = I_- - I_+/I_- + I_+ \tag{5.3}$$

(Figure 5.4B). Evidence of loss of polarization is seen for the larger S content, where a ρ value of 60% for CdSSe (x = 4%) and a ρ value of 17 % for x = 8% is observed. The dramatic difference in the values for ρ between the two samples is due to changes ordering of the states. The expected value for ρ in the absence of state mixing (using a bulk value for

g = 0.6 and 4.2 K) CdSe yields a g value of 54% at 31 T, which is far higher than observed for the 8% sample. The lowered value is attributed to spin loss due to state mixing.

Integrating over all angles and using eqn 6.3, the polarization data can be fit allowing the average g-value of σ^+ and σ^- to be extracted

$$\rho = \int_0^1 \frac{I_-(cos\theta) - I_+(cos\theta)}{I_-(cos\theta) + I_+(cos\theta)} dcos\theta \tag{5.4}$$

where the integration covers all angles Θ. Fitting the ρ value provides an average g-value of 1.74 for the NC-CdSSe samples. The calculated g-value data is large compared to bulk CdSe values (g = 0.6) and earlier reports on pure NC CdSe, where values of 1.2 and 0.75 have been reported. The larger g-value from the fit to ρ is indicative of state mixing in the CdSSe alloy samples, as previously suggested.

As the magnitude of the perturbation increases with sulfur incorporation, we also expect changes in the electron phonon coupling matrix element (α) based on eqn 6.2. In eqn 5.2 the el-ph term (α) is size dependent[99, 100, 86, 101, 102, 77].

$$\alpha = \left(\frac{1}{\epsilon_\infty} - \frac{1}{\epsilon_0}\right)\frac{e^2}{2r_p^2}\frac{1}{\hbar\omega_L} \tag{5.5}$$

where ϵ_∞ and ϵ_0 are the high and low frequency dielectric constants, e is the charge of an electron, r_p is the polaron radii, and ω_L is the LO phonon frequency. A large polaron will typically exhibit a large α. A large value of α leads to efficient spin relaxation. In the two samples the average value of α is 0.31 or 4% S and 0.22 for 8%. These values are consistent with values theoretically predicted for NC-CdSe[99]. From the value of α, the size of the emissive excitonic polaron can be extracted using eqn. 2. This predicts a diameter of 3.9 - 4.5 nm for the CdSSe alloy samples which correlates reasonably with the measured NC diameter by TEM. While the result is not surprising, the observation is important as it confirms that the photoluminescence arises from a self trapped excitonic polaron of the size of the nanocrystal rather than a localized emissive state, as described by Klimov, et al[103, 104, 105, 106].

CHAPTER 6

CdSSe Temperature Dependent Magneto-photoluminescence

CdSSe nanocrystals were prepared to study the magneto-optical photoluminescence properties. The involvement of phonons was observed in the mixing of states to produce a lower than expected low temperature polarization ratio. The observation of two emitting state results from the lowering of symmetry due to the sulfur incorporation. A phonon frequency of 100 cm^{-1} was found to be involved in the mixing of the emitting state shown by changing the magnetic field and observing the change in the mixing that occurs as a function of field.

6.1   Introduction

The size excitonic nature of CdSe has been of great interest[107, 108, 109, 69]. The observation of excitonic fine-structure for CdSe has prompted single molecule experiments that suggest the interactions between the bright and dark exciton. In an earlier report the fine-structure of the exciton under line- narrowed photoluminescence exhibited a phonon progression indicative of electron-phonon coupling playing a role in the relaxation of CdSe[110, 85]. In addition, Furis et al have observed a temperature dependent spin polarization under circular polarized light, with loss of spin integrity with increasing temperature as phonon population allows relaxation between the bright and dark exciton[88]. The equilibrium between the bright and dark exciton states has been in question for many years[85, 111, 112]. The dynamics of the relaxation has had many explanations including the observed fast relaxation are influenced by carrier trapping auger, phonon, and tunneling processes[85, 113, 114]. In this communication we describe the observation of two states in equilibrium which at low temperatures and under field can be differentiated through the use of circularly polarized light.
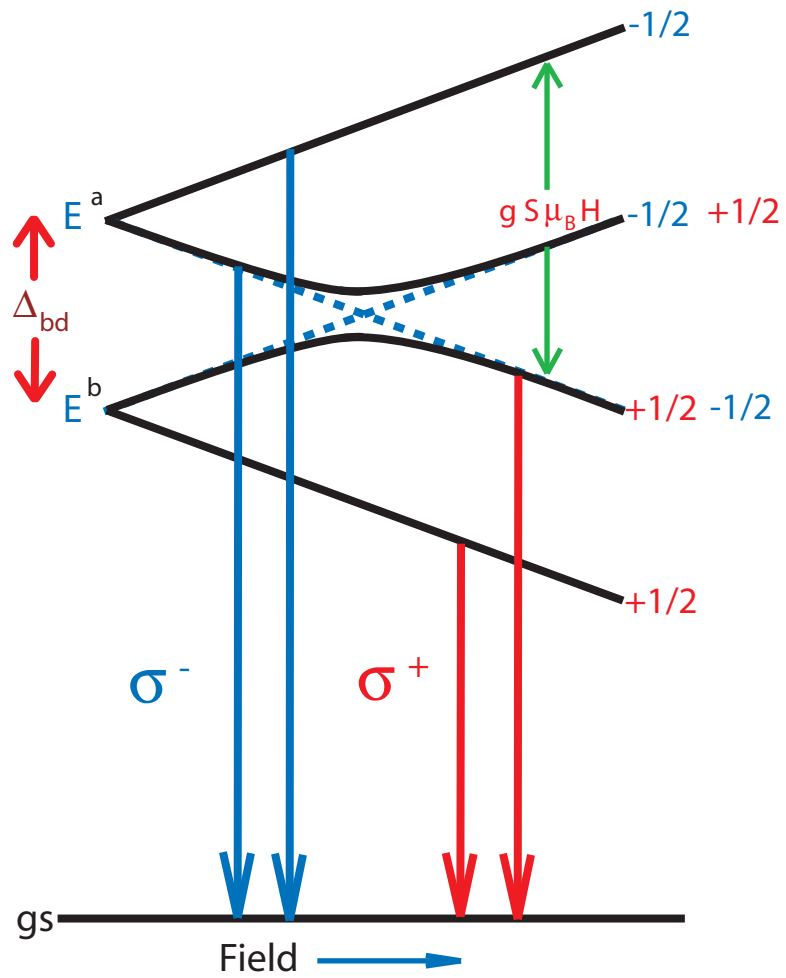
Figure 6.1: The splitting of the exciton when a C'_{3v} lowering of symmetry occurs to a wurtzite structure. The allowed transitions are labeled as a function of circular polarized direction.

The subtle change in symmetry from addition of sulfur brings about the ability to analyze the interaction between the bright and dark exciton. The nature of the relaxation can be analyzed with the use of impurities to observe the change that occurs when a dopant is added in small concentrations.

In a semiconductor, a reduction of temperature induces a change in the thermal population of states, which leads to a differentiation of the states greater than the available thermal energy. Recently, we observed a Debye temperature of 82 K which results in an average phonon energy of 7 meV.[78] This is the minimum energy two states can have before they are thermally scattered and little differentiation is observed between them. This energy is greater than the thermal energy available making it possible to differentiate the two states.

6.2   Theory

The ability to differentiate the different states and mixing associated is dependent on the temperature. As the phonon density becomes significant ($\sim$20 K) both states are indistinguishable due to thermal phonon population. As a result of electron-phonon coupling, the first two excitons (E_1 and E_2) can be populated at room temperature, resulting in the observed temperature dependent photoluminescence. The nature of the el-ph interaction will be size dependent, as has been suggested by CdSe pressure dependent studies[85, 77]. The temperature dependence of the photoluminescence can be described by invoking the Huang-Rhys model to account for E_1 and E_2 coupling, where the observed PL energy is,

$$E(T) = E(0) + (E(1) - E(0)) \left(\frac{k_B T}{\hbar \omega}\right)^3 \int_0^{\frac{\hbar \omega}{k_B T}} \frac{x^3}{e^{-x} - 1} - S_\alpha \hbar \omega (Coth(\frac{\hbar \omega}{2 k_B T}) - 1) \quad (6.1)$$

where E(0) is the zero-point energy and ω represents the average lattice phonon frequency for el-ph interaction. In bulk CdSe (wurtzite symmetry), the available optical phonons for coupling E_1 and E_2 are 25.9, 14.2, 4.0 meV attributed to the A_1, B_1, and E_2 modes, respectively[38]. For a nanocrystal, since the electrons are extremely susceptible to changes in the crystal momentum as a result of the changing surface potential, the K$\neq$0 phonons may play a role in the electron phonon interactions involved in the spin-flip transition[115]. In eqn 6.1, E(1) is dominated by the energy of the E_2 state, when E_1 and E_2 are thermally equilibrated. This is easily explained by considering that the rate of radiative relaxation from E_2 to the ground state is faster due to efficient phonon coupling. If E_1 and E_2 are strongly

coupled, then rapid depopulation of the E_1 state into E_2 will occur when the temperature is greater than the Debye temperature. At temperatures below the Debye temperature, the E_1 and E_2 state population would need to be explicitly defined as independently populated states.

To account for the contributions of phonons to the equilibration of the E_1 and E_2, phonon contributions are added in eqn 6.1 as a probability between the available phonon energy and the maximum allowed phonon energy[116] resulting in $\left(\frac{k_B T}{\hbar \omega}\right)^3 \int_0^{\frac{\hbar \omega}{k_B T}} \frac{x^3}{e^{-x}-1}$. This results in the ability to differentiate the E_1 and the E_2 state as a function of temperature or magnetic field. As T$\to$ 0, the equilibration of the states will not arise due to lack of phonon density in the system. The equilibration can be followed in the energy spectrum where a blue shift as the temperature is increased from 4.2 K as the E_2 begins to be populated from the available phonons followed by a red shift arising from the electron-phonon interaction.

Of great interest is the polarization ratio extracted from the intensity ratios between right and left circular polarized excitation. As a result of the two states contributing to the photoluminescence the polarization ratio is dependent on the independent contribution to the bulk polarization. For this we use the polarization of two states and therefore two sets of polarizations containing the two polarizations. The intensity is integrated over all angles to produce and average orientation of the magnetic field to the dipole. The intensity follows

$$
\begin{aligned}
I_{\mp}(cos\theta) = ((1 \pm cos\theta)^2 e^{\frac{g\mu_B H cos\theta}{2k_B T}} + \\
(1 \mp cos\theta)^2 e^{-\frac{g\mu_B H cos\theta}{2k_B T}})/(e^{\frac{g\mu_B H cos\theta}{2k_B T}} + e^{-\frac{g\mu_B H cos\theta}{2k_B T}})
\end{aligned}
\tag{6.2}
$$

where the g-value is the the Landé splitting factor, H is the field and θ is the angle of the magnetic field with respect to the direction of the dipole. The polarization is then equal to

$$
\rho = I_- - I_+/I_- + I_+
\tag{6.3}
$$

where the two different polarizations are used. To extract out the different polarizations from the different states, the equation is as follows where

$$
P_{total} = P_1(1 - x) + P_2(x)
\tag{6.4}
$$

where x determines the polarization ratio between the two states.

6.3   Experimental

The materials are prepared by the lyothermal method used by Magana et al[69, 78] utilizing $[Cd_{10}Se_4(SPh)_{16}]$ in hexadecylamine (HDA). Five nanometer 2% sulfur CdSSe was isolated as pyridine passivated nanocrystals. For the photoluminescence measurements, optically transparent thin films were prepared by dissolving the sample in pyridine, adding N-(3-(trimethoxisilyl)-propyl) EthyleneDiamine, and allowing the sample to condense into a cross-linked amorphous organosilane glass (10 μm) for 12 hrs at 298 K. The magneto-photoluminescence (MPL) experiments were performed at the National High Magnetic Field Laboratory (NHFML-FSU) using an Ar^+ ion laser (70 μW @ 458 nm) coupled through a UV fiber optic into a Janis cryostat (4.2-300 K) which was placed into the 31 T resistive magnet (0 $\rightarrow$ 30 T) to allow temperature dependent photoluminescence at different fields to be measured. Circularly polarized excitation was generated using a plastic polarizer and a quarter wave plate mounted inside the cryostat in front of the sample. The photoluminescence was collected on a separate fiber coupled to a one-meter monochromator (600 g/mm) with a Princeton Instruments nitrogen cooled CCD (512 X 1024 pixels).

6.4   Discussion and Conclusion

In figure 6.2 the intensity spectra is analyzed using equation 6.1. With decreasing temperature, the photoluminescence energy shifts to high value as the phonon population is decreasing. Analysis of the plot shows a decrease in the energy below 20 K. This suggest the contribution of another state. As the field is increased to 30 T, the observed photoluminescence is still dominated by the thermalized E_1 and E_2 exciton states resulting from thermally driven spin-flip. The temperature dependence of the intensity is expected due to the reduction of the non-radiative pathways associated with a thermally activated spin-flip. Each of the polarization is going to contain two components due to a thermally induced spin-flip.

From the polarization ratios one can fit the g-values for the different excitons. As observed in table x at 5 T the two states have equal polarizations where as the field is increased the ratio stops increasing to maximum of 70:30 ratio of state one to two. The g-values also reflect the change in the magnitude ratios to reflect their contribution. The values are not far from the expected g of 4[37].
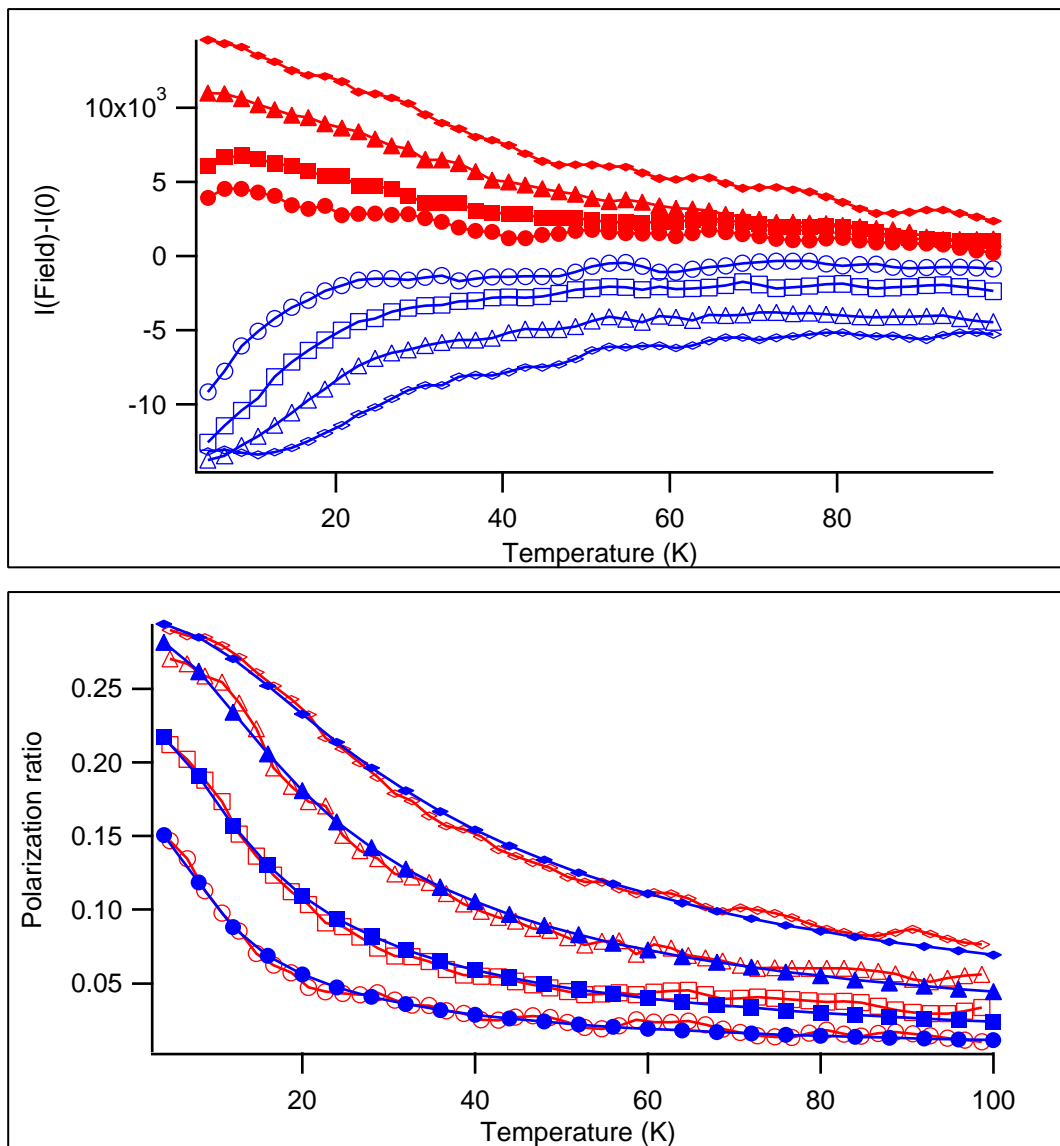
Figure 6.2: A) 4.2 K Magneto-photoluminescence Intensity difference with respect to the intensity at zero field. Each plot is the difference at 5.0 T (○), 10.0 T (□), 20 T (△), and 30T (◇) for right (open) and left (closed) circularly polarized excitation. B) The polarization ratio at 5.0 T (○), 10.0 T (□), 20 T (△), and 30T (◇).

Table 6.1: Polarization fit using a two state model where the g-value of is set to be the same for each state

Field (T)	ratio	g_1	g_2
5	0.50	-1.35	4.25
10	0.65	-3.22	3.96
20	0.70	-4.12	3.76
30	0.70	-3.57	3.57

The temperature dependent energy spectra was analyzed using eqn 6.1, where E_1 and E_2 exciton states can be assigned to E_1= 2.1935 eV, and E_2= 2.2053 eV coupled by 12 meV phonon contributions. As shown in figure 6.3,the thermalization of the two states is accompanied by a change in the observed energy for σ^- and σ^+ consistent with the change in population of the two states as temperature is decreased. The energy shift tracks the population equilibrium between the two states, which shifts with increasing applied field. The difference in the polarization changes more significantly for the σ^-, than the σ^+ since the σ^+, state is the groundstate, while σ^- is the thermally activated state. The difference between E_1 and E_2 is Δ_{bd} which is of the order of 6 meV in pure CdSe[85]. The second state is observed through the spinflip that occurs between states where one can see the disorder in the Zeeman splitting of this state as a result of the mixing that occurs.

From analysis of the zero kelvin energy as a function of field the Zeeman splitting can be extracted (Fig. 6.4). Using a first order Zeeman splitting the g-value is calculated to be 9.4 and 6.3 for E_1 and E_2, respectively. The average phonon frequency (Debye temperature) from the fit to eqn 6.1 shows an increase from 22 K to 95 K that indicates the available phonons that populate the E_2 states as the field increases. This is consistent with the Debye temperature of the nanocrystals measured by heat capacity is 84 K[78].

The use of temperature dependence to separate emissive states allows one to determine the range of energy necessary to couple the two states. Using a magnetic field we can distinctively determine the effect of the Zeeman splitting on the population distribution. The phonons involved appears to be linear with magnetic field indicating the strength of the electron phonon coupling. As a function of magnetic field the localization of the exciton is observed in the increase of the electron phonon coupling. The coupling constant for both polarizations follow the same pattern starting with a zero field coupling constant of 0.1 to 1 at 30 T indicating the localization of the exciton photoluminescence. From the electron-phonon one can calculate the polaron size. The relation follows

$$\alpha = (\frac{1}{\epsilon_\infty} - \frac{1}{\epsilon_0})\frac{e^2}{2r_p^2}\frac{1}{\hbar\omega_L} \tag{6.5}$$

where e is the electron Coulomb potential, ϵ_∞ and ϵ_0 are the high and low frequency dielectric constants, ω_L is the Debye frequency, and r_p is the polaron radii. Using heat capacity measured 84 K Debye temperature, the polaron radius from 2.7 nm to 0.9 at 30 T.
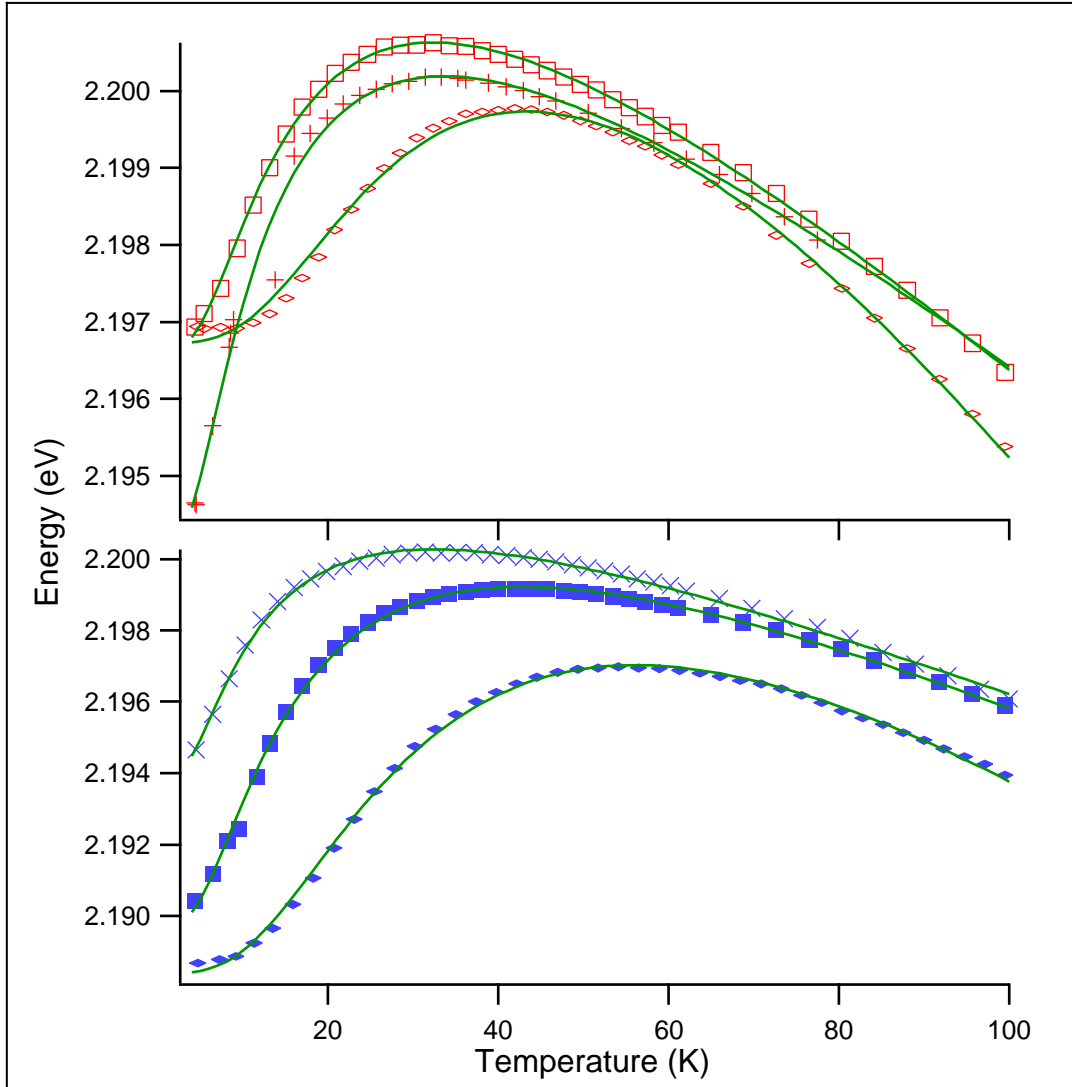
Figure 6.3: Magneto-photoluminescence Energy after fitting to a Voigt function of CdSe at 0.01 T ($\diamond$), 10 T ($\square$), and 30T ($+$) at 4.2 K for right (open) and left (solid) circular polarized light. The spectra were fit to eqn 6.1 resulting in the solid line in each spectrum.
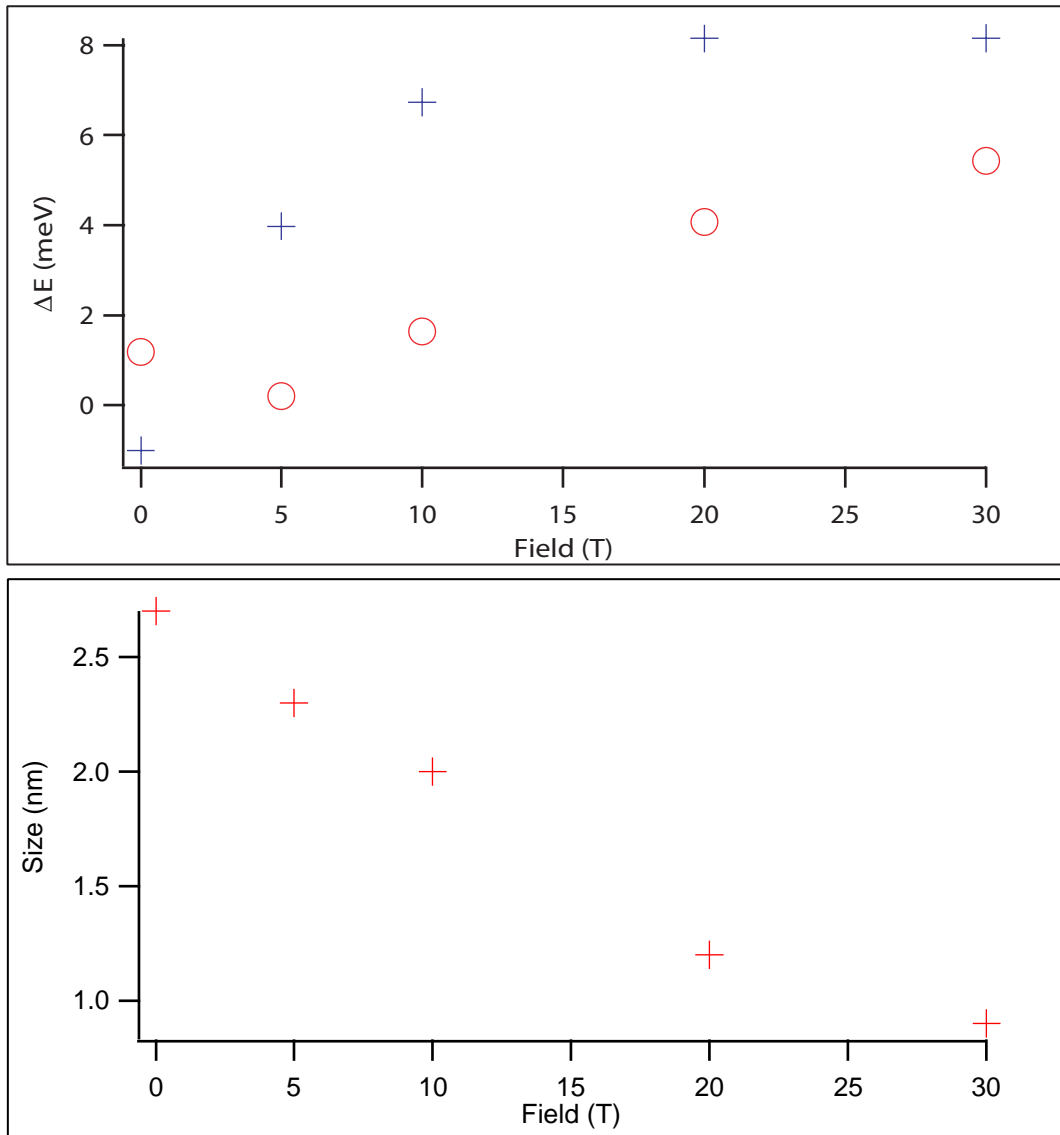
Figure 6.4: A) Change in polarization energy from fit for CdSSe as a function of field for the first (∘) and second excitons (+) at 4.2 K. B) The polaron size is calculated using equation 6.5 as a function of applied field.

116

The surprising result is that the size of the polaron is the size of the particle and by the time it gets to 30 Tesla the size has reduced to a 2 nm diameter.

The temperature dependent magneto-photoluminescence allows determination of Δ_{bd} by extracting the thermal contribution to the mixing of the states. The localization of the exciton as a function magnetic field is not surprising because of the doping of sulfur is expected to induce localization of the exciton.

REFERENCES

[1] Louis Brus. Chemical approaches to semiconductor nanocrystals. *Journal of Physics and Chemistry of Solids*, 59(4):459–465, 1998. 1

[2] D. D. Awschalom, J. Warnock, J. M. Hong, L. L. Chang, M. B. Ketchen, and W. J. Gallagher. Magnetic manifestations of carrier confinement in quantum wells. *Phys. Rev. Lett.*, 62(2):199–202, 1989. 1, 3.1

[3] D. D. Awschalom, M. E. Flatte, and N. Samarth. Spintronics. *Sci. Am.*, 286(6):66–73, 2002. 1

[4] R. L. Aggarwal, J. K. Furdyna, and S. von Molnar. *Diluted magnetic (semimagnetic) semiconductors*. Mater. Res. Soc. symp. proc., v. 89. Mater. Res. Soc., Pittsburgh, Pa., 1987. 1, 3.1

[5] R.L. Aggarwal, J.K. Furdyna, and S. von Molnar, editors. *Semiconductors and Semimetals*, volume 25 of *Diluted Magnetic Semiconductors*. Academic Press, Inc, New York, 1988. 1, 1.5.2

[6] W. J. M. Dejonge and H. J. M. Swagten. Magnetic-properties of diluted magnetic semiconductors. *Journal of Magnetism and Magnetic Materials*, 100(1-3):322–345, 1991. 1

[7] J. K. Furdyna. Diluted magnetic semiconductors. *J. Appl. Phys.*, 64(4):R29–R64, 1988. 1, 1.4.3, 1.5.2, 2.0.3, 3.1, 3.1, 4.1, 5.1

[8] J. A. Gaj. Magneto-optical properties of large-gap diluted magnetic semiconductors. *Semiconductors and Semimetals*, 25:275–309, 1988. 1

[9] J. A. Gaj, R. R. Galazka, and M. Nawrocki. Giant exciton faraday-rotation in cd1-xmnxte mixed-crystals (reprinted from solid-state commun, vol 25, pg 193-195, 1978). *Solid State Communications*, 88(11-12):923–925, 1993. 1

[10] R. R. Galazka, S. Nagata, and P. H. Keesom. Paramagnetic-spin-glass-antiferromagnetic phase-transitions in cd1-xmnxte from specific-heat and magnetic-susceptibility measurements. *Phys. Rev. B*, 22(7):3344–3355, 1980. 1, 2.0.3, 2.0.3, 3.1

[11] S. B. Oseroff. Magnetic-susceptibility and electron-paramagnetic-res measurements in concentrated spin-glasses - cd1-xmnxte and cd1-xmnxse. *Phys. Rev. B*, 25(11):6584–6594, 1982. 1, 2.0.3, 2.0.3, 2.2, 3.1

[12] Y. Shapira, S. Foner, D. H. Ridgley, K. Dwight, and A. Wold. Technical saturation and magnetization steps in diluted magnetic semiconductors - predictions and observations. *Physical Review B*, 30(7):4021–4023, 1984. 1, 3.1

[13] Donald Phillip Mullin. *Microwave Studies of Semimagnetic Semiconductors*. PhD thesis, Purdue University, 1980. 1, 2.0.3, 2.0.3

[14] L. Bryja and J. A. Gaj. Photoluminescence of cd1-xmnxse. *Acta Physica Polonica A*, 67(2):303–306, 1985. 1

[15] J. A. Gaj, R. R. Gatazka, and M. Nawrocki. Giant exciton faraday-rotation in cd1-xmnxte mixed-crystals. *Solid State Commun.*, 25(3):193–195, 1978. 1, 3.1

[16] J. A. Gaj, R. Planel, and G. Fishman. Relation of magneto-optical properties of free-excitons to spin alignment of mn2+ ions in cd1-xmnxte. *Solid State Communications*, 29(5):435–438, 1979. 1, 4.3.1, 4.3.1

[17] S. Nagata, R. R. Galazka, D. P. Mullin, H. Akbarzadeh, G. D. Khattak, J. K. Furdyna, and P. H. Keesom. Magnetic-susceptibility, specific-heat, and the spin-glass transition in hg1-xmnxte. *Physical Review B*, 22(7):3331–3343, 1980. 1, 2.0.3

[18] A. Twardowski, E. Rokita, and J. A. Gaj. Valence band spin-orbit-splitting in cdte and cd1-xmnxte and giant zeeman effect in the gamma-7 band of cd1-xmnxte. *Solid State Commun.*, 36(11):927–930, 1980. 1, 3.1

[19] L. E. Brus. Electron–electron and electron-hole interactions in small semiconductor crystallites: The size dependence of the lowest excited electronic state. *The Journal of Chemical Physics*, 80(9):4403–4409, 1984. 1, 1.5.1

[20] Steven C. Erwin, Lijun Zu, Michael I. Haftel, Alexander L. Efros, Thomas A. Kennedy, and David J. Norris. Doping semiconductor nanocrystals. *Nature*, 436(7047):91–94, 2005. 1, 2.0.3, 3.1

[21] Hideo Ohno. Ferromagnetic semiconductors for spin electronics. *Journal of Magnetism and Magnetic Materials*, 242-245(Part 1):105–107, 2002. 1

[22] D. R. Gamelin. Doped semiconductor nanocrystals: Synthesis, characterization, physical properties, and applications. In Karlin Kenneth D., editor, *Progress in Inorganic Chemistry*, volume 54, page 519. John Wiley, New Jersey, 2005. 1, 2.0.3, 2.0.3, 4.1

[23] D. J. Norris, N. Yao, F. T. Charnock, and T. A. Kennedy. High-quality manganese-doped znse nanocrystals. *Nano Letters*, 1(1):3–7, 2001. 1, 2.0.3

[24] K. M. Hanif, R. W. Meulenberg, and G. F. Strouse. Magnetic ordering in doped cd1-xcoxse diluted magnetic quantum dots. *Journal of the American Chemical Society*, 124(38):11495–11502, 2002. 1, 2.0.3, 2.1, 3.3.1

[25] F. V. Mikulec, M. Kuno, M. Bennati, D. A. Hall, R. G. Griffin, and M. G. Bawendi. Organometallic synthesis and spectroscopic characterization of manganese-doped cdse nanocrystals. *J. Am. Chem. Soc.*, 122(11):2532–2540, 2000. 1, 2.0.3, 2.2, 3.2

[26] W. Chen, A. G. Joly, and J. Z. Zhang. Up-conversion luminescence of mn2+ in zns : Mn2+ nanoparticles. *Physical Review B*, 6404(4):041202, 2001. 1, 2.0.3

[27] Jr. Norman, Thaddeus J., Donny Magana, Thea Wilson, Colin Burns, Jin Z. Zhang, Daliang Cao, and Frank. Bridges. Optical and surface structural properties of mn2+-doped znse nanoparticles. *J. Phys. Chem. B*, 107:6309–6317, 2003. 1, 2.0.3, 2.1

[28] R. W. Meulenberg, T. van Buuren, K. M. Hanif, T. M. Willey, G. F. Strouse, and L. J. Terminello. Structure and composition of cu-doped cdse nanocrystals using soft x-ray absorption spectroscopy. *Nano Letters*, 4(11):2277–2285, 2004. 1, 2.0.3, 2.1

[29] D.L. Beke. *Landolt-Brnstein Group III: Condensed Matter*, volume 33 of *Diffusion in Semiconductors*. Springer-Verlag GmbH, New York, 1998. 1

[30] R. L. Flurry Jr. *Symmetry Groups Theory and Chemical Applications*. Prentice-Hall, Inc., New Jersey. 1, 5.3

[31] M. Hamermesh. *Group Theory and its Application to Physical Problems*. Dover Publications, Inc., New York. 1

[32] W. S. Struve. *Fundamentals of Molecular Spectroscopy*. John Wiley & Sons, New York. 1

[33] A. K. Zvezdin and V. A. Kotov. *Studies in Condensed Matter Physics*. Modern Magnetooptics and Magnetooptical Materials. J W Arrowsmith Ltd, Philadelphia, 1997. 1

[34] C. Kittel. *Introduction to Solid State Physics*. John Wiley $ Sons, Inc, New Jersey, 2005. 1

[35] N. W. Ashcroft and Mermin N. D. *Solid State Physics*. Thomson Learning Inc., Madrid, 1976. 1, 2.0.3, 2.2

[36] E. S. R. Gopal. *Specific Heats at Low Temperatures*. Plenum Press, New York, 1966. 1, 3.3.1, 3.3.2

[37] E. Johnston-Halperin, D. D. Awschalom, S. A. Crooker, Al. L. Efros, M. Rosen, X. Peng, and A. P. Alivisatos. Spin spectroscopy of dark excitons in cdse quantum dots to 60 t. *Phys. Rev. B*, 63(20):205309, Apr 2001. 1.2.2, 5.3, 5.3, 6.4

[38] F. Widulle, S. Kramp, N. M. Pyka, A. Gobel, T. Ruf, A. Debernardi, R. Lauck, and M. Cardona. The phonon dispersion of wurtzite cdse. *Physica B: Condensed Matter*, 263-264:448–451, 1999. 1.3, 6.2

[39] M.G. Berrettini, G. Braun, J.G. Hu, and G.F. Strouse. Nmr analysis of surfaces and interfaces in 2-nm cdse. *J. Am. Chem. Soc.*, 126(22):7063–7070, 2004. 1.3.4

[40] P. Bruno and C. Chappert. Ruderman-kittel theory of oscillatory interlayer exchange coupling. *Phys. Rev. B*, 46:261–270, 1992. 1.4.2, 1.4.2, 3.3.1

[41] B. E. Larson, K. C. Hass, H. Ehrenreich, and A. E. Carlsson. Theory of exchange interactions and chemical trends in diluted magnetic semiconductors. *Phys. Rev. B*, 37(8):4137–4154, Mar 1988. 1.4.2, 3.3.1

[42] T. Jungwirth, W. A. Atkinson, B. H. Lee, and A. H. MacDonald. Interlayer coupling in ferromagnetic semiconductor superlattices. *Phys. Rev. B*, 59(15):9818–9821, 1999. 1.4.3, 3.1, 3.3.1

[43] Y. Shapira, S. Foner, P. Becla, D. N. Domingues, M. J. Naughton, and J. S. Brooks. Nearest-neighbor exchange constant and mn distribution in $zn_{1-x}mn_x$te from high-field magnetization step and low-field susceptibility. *Phys. Rev. B*, 33(1):356–365, 1986. 1.4.3, 3.3.1

[44] K. H Hellwege, editor. *Landolt-Börnstein Group III: Crystal and Solid State Physics*, volume 17B of *Semiconductors*. Springer-Verlag GmbH, New York, 1982. 1.4.3, 3.3.1

[45] V. K. Bazhenov and V. I. Fistul'. Isoelectronic impurities in semiconductors: Current status(review). *Sov. Phys. Semicond.*, 18(8):843–853, 1984. 1.4.3

[46] Dong Yu, Congjun Wang, and Philippe Guyot-Sionnest. n-Type Conducting CdSe Nanocrystal Solids. *Science*, 300(5623):1277–1280, 2003. 1.4.3, 3.3.1

[47] Arthur L. Robinson and Richard H. Bube. Photoelectronic properties of defects in cdse single crystals. *Journal of Applied Physics*, 42(13):5280–5295, 1971. 1.4.3, 3.3.1

[48] D. Nesheva, S. Reynolds, C. Main, Z. Aneva, and Z. Levi. Defect states in cdse nanocrystalline layers. *phys. stat. sol. (a)*, 202(6):1081–1087, 2005. 1.4.3, 3.1, 3.3.1

[49] S. A. Wolf, D. D. Awschalom, R. A. Buhrman, J. M. Daughton, S. von Molnar, M. L. Roukes, A. Y. Chtchelkanova, and D. M. Treger. Spintronics: A spin-based electronics vision for the future. *Science*, 294(5546):1488–1495, 2001. 2.0.3

[50] D. Zipse, J. M. North, R. M. Achey, N. S. Dalal, S. Hill, R. S. Edwards, E. S. Choi, and J. S. Brooks. Semiconductivity, spin delocalization, and excited states of the single molecule magnets fe8br8 and mn-12-acetate (invited). *Journal of Applied Physics*, 95(11):6900–6905, 2004. 2.0.3

[51] N. Feltin, L. Levy, D. Ingert, and M. P. Pileni. Magnetic properties of 4-nm cd1-ymnys nanoparticles differing by their compositions, y. *J. Phys. Chem. B*, 103:4–10, 1999. 2.0.3

[52] S. L. Cumberland, K. M. Hanif, A. Javier, G. A. Khitrov, G. F. Strouse, S. M. Woessner, and C. S. Yun. Inorganic clusters as single-source precursors for preparation of cdse, znse, and cdse/zns nanomaterials. *Chemistry of Materials*, 14(4):1576–1584, 2002. 2.0.3, 2.1, 5.2

[53] O. E. Raola and G. F. Strouse. Synthesis and characterization of eu-doped cadmium selenide nanocrystals. *Nano Letters*, 2(12):1443–1447, 2002. 2.0.3, 2.1

[54] N. S. Norberg, K. R. Kittilstved, J. E. Amonette, R. K. Kukkadapu, D. A. Schwartz, and D. R. Gamelin. Synthesis of colloidal mn2+: Zno quantum dots and high-tc ferromagnetic nanocrystalline thin films. *Journal of the American Chemical Society*, 126(30):9387–9398, 2004. 2.0.3, 3.1

[55] Kuei Fang Hsu, Sim Loo, Fu Guo, Wei Chen, Jeffrey S. Dyck, Ctirad Uher, Tim Hogan, E. K. Polychroniadis, and Mercouri G. Kanatzidis. Cubic agpbmsbte2+m: Bulk thermoelectric materials with high figure of merit. *Science*, 303(5659):818–821, 2004. 2.0.3

[56] J. Lu, S. Wei, W. C. Yu, H. B. Zhang, and Y. T. Qian. Structure and luminescence of 2d dilute magnetic semiconductors: Cd1-xmnxse center dot l-0.5 (l = diamines). *Chem. Mater.*, 17(7):1698–1703, 2005. 2.0.3

[57] M. Miyake, T. Torimoto, M. Nishizawa, T. Sakata, H. Mori, and H. Yoneyama. Effects of surface charges and surface states of chemically modified cadmium sulfide nanoparticles immobilized to gold electrode substrate on photoinduced charge transfers. *Langmuir*, 15(8):2714–2718, 1999. 2.0.3

[58] Robert J. Friauf. Correlation oeffects for diffusion in ionic crystals. *J. Appl. Phys.*, 33(1):494, 1962. 2.0.3

[59] Dillon Mapother, H. Neslon Crooks, and Robert Maurer. Self-diffusion of sodium in sodium chloride and sodium bromide. *J. Chem. Phys.*, 18(9):1231, 1950. 2.0.3

[60] T. Lover, W. Henderson, G. A. Bowmaker, J. M. Seakins, and R. P. Cooney. Electrospray mass spectrometry of thiophenolate-capped clusters of cds, cdse, and zns and of cadmium and zinc thiophenolate complexes: Observation of fragmentation and metal, chalcogenide, and ligand exchange processes. *Inorganic Chemistry*, 36(17):3711–3723, 1997. 2.1

[61] Benjamin L. Frankamp, Andrew K. Boal, Mark T. Tuominen, and Vincent M. Rotello. Direct control of the magnetic interaction between iron oxide nanoparticles through dendrimer-mediated self-assembly. *Journal of the American Chemical Society*, 127(27):9731, 2005. 2.2, 2.2

[62] J. T. Culp, J. H. Park, M. W. Meisel, and D. R. Talham. Monolayer, bilayer, multilayers: Evolving magnetic behavior in langmuir-blodgett films containing a two-dimensional iron-nickel cyanide square grid network. *Inorg. Chem.*, 42(9):2842–2848, 2003. 2.2, 3.3

[63] D. Magana and G.F. Strouse. in preparation. 2007. 2.2

[64] J. S. Van-Wieringen. Paramagnetic resonance of divalent manganese incorporated in various lattices. *Discussions of the Faraday Society*, 19:118, 1955. 2.2, 2.2

[65] T. Igarashi, M. Ihara, T. Kusunoki, K. Ohno, T. Isobe, and M. Senna. Characterization of mn2+ coordination states in zns nanocrystal by epr spectroscopy and related photoluminescence properties. *Journal of Nanoparticle Research*, 3(1):51–56, 2001. 2.2

[66] C. B. Murray, C. R. Kagan, and M. G. Bawendi. Synthesis and characterization of monodisperse nanocrystals and close-packed nanocrystal assemblies. *Annual Review of Materials Science*, 30:545–610, 2000. 2.2

[67] K. R. Kittilstved and D. R. Gamelin. Manipulating polar ferromagnetism in transition-metal-doped zno: Why manganese is different from cobalt (invited). *J. Appl. Phys.*, 99(8):08M112, 2006. 3.1, 3.1

[68] B. Beschoten, P. A. Crowell, I. Malajovich, D. D. Awschalom, F. Matsukura, A. Shen, and H. Ohno. Magnetic circular dichroism studies of carrier-induced ferromagnetism in $(ga_{1-x}mn_x)as$. *Phys. Rev. Lett.*, 83(15):3073–3076, 1999. 3.1

[69] D. Magana, S. Perera, A.G. Harter, N. S. Dalal, and G.F. Strouse. Switching-on superparamagnetism in mn:cdse quantum dots. *J. Am. Chem. Soc.*, 128(9):2931–2939, 2006. 3.1, 3.2, 3.2, 3.3.1, 3.3.1, 4.2, 6.1, 6.3

[70] H. Ohno. Making Nonmagnetic Semiconductors Ferromagnetic. *Science*, 281:951–956, 1998. 3.1

[71] T. Dietl. Origin of ferromagnetism and nano-scale phase separations in diluted magnetic semiconductors. *Physica E: Low-dimensional Systems and Nanostructures*, 35(2):293–299, 2006. 3.1

[72] T. Dietl, H. Ohno, F. Matsukura, J. Cibert, and D. Ferrand. Zener Model Description of Ferromagnetism in Zinc-Blende Magnetic Semiconductors. *Science*, 287(5455):1019–1022, 2000. 3.1

[73] T. Jungwirth, Jürgen König, Jairo Sinova, J. Kučera, and A. H. MacDonald. Curie temperature trends in (iii,mn)v ferromagnetic semiconductors. *Phys. Rev. B*, 66(1):012402, 2002. 3.1, 3.3.2

[74] P. V. Radovanovic, N. S. Norberg, K. E. McNally, and D. R. Gamelin. Colloidal transition-metal-doped zno quantum dots. *Journal of the American Chemical Society*, 124(51):15192–15193, 2002. 3.1

[75] Kevin R. Kittilstved, Dana A. Schwartz, Allan C. Tuan, Steve M. Heald, Scott A. Chambers, and Daniel R. Gamelin. Direct kinetic correlation of carriers and ferromagnetism in co[sup 2+]: Zno. *Physical Review Letters*, 97(3):037203, 2006. 3.1

[76] J. M. D. Coey, S. von Molnar, and R. J. Gambino. Magnetic heat capacity of an amorphous gd-al alloy. *Solid State Commun.*, 24(2):167–170, 1977. 3.1, 3.3.2, 3.3.2

[77] R. W. Meulenberg and G. F. Strouse. Pressure-induced electronic coupling in cdse semiconductor quantum dots. *Physical Review B*, 66(3):035317, 2002. 3.3.1, 5.3, 6.2

[78] D. Magana, N.S. Dalal, S. von Molnar, and G.F. Strouse. submitted. 2007. 4.1, 4.2, 6.1, 6.3, 6.4

[79] K. Ando and H. Munekata. Magneto-optical study of spin-carrier interactions in (in,mn)as. *Journal of Magnetism and Magnetic Materials*, 272-276(3):2004–2005, 2004. 4.1

[80] P.I. Archer, S.A. Santangelo, and D.R. Gamelin. Direct observation of sp-d exchange interactions in colloidal mn2+- and co2+-doped cdse quantum dots. *Nano Letters*, 7(4):1037–1043, 2007. 4.3, 5.2

[81] S. Lee, M. Dobrowolska, and J. K. Furdyna. Zeeman mapping of exciton localization in self-assembled cdse quantum dots using diluted magnetic semiconductors. *Solid State Communications*, 141(6):311–315, 2007. 4.3

[82] K. P. Odonnell and X. Chen. Temperature-dependence of semiconductor band-gaps. *Applied Physics Letters*, 58(25):2924–2926, 1991. 4.3.1

[83] J.M. An, A. Franceschetti, and A. Zunger. The excitonic exchange splitting and radiative lifetime in pbse quantum dots. *Nano Letters*, 2007. 5.1

[84] S. Xu, A. A. Mikhailovsky, J. A. Hollingsworth, and V. I. Klimov. Hole intraband relaxation in strongly confined quantum dots: Revisiting the ıphonon bottleneckȷ problem. *Phys. Rev. B*, 65(4):045319, Jan 2002. 5.1

[85] M. Nirmal, D. J. Norris, M. Kuno, M. G. Bawendi, A. L. Efros, and M. Rosen. Observation of the dark exciton in cdse quantum dots. *Physical Review Letters*, 75(20):3728–3731, 1995. 5.1, 5.3, 5.3, 5.3, 6.1, 6.2, 6.4

[86] Al. L. Efros and M. Rosen. The electronic structure of semiconductor nanocrystals. *Annual Review of Materials Science*, 30(1):475–521, 2000. 5.1, 5.3

[87] J. Kim, C.Y. Wong, P.S. Nair, K.P. Fritz, S. Kumar, and G.D. Scholes. Mechanism and origin of exciton spin relaxation in cdse nanorods. *Journal of Physical Chemistry B*, 110(50):25371–25382, 2006. 5.1

[88] M. Furis, J. A. Hollingsworth, V. I. Klimov, and S. A. Crooker. Time- and polarization-resolved optical spectroscopy of colloidal cdse nanocrystal quantum dots in high magnetic fields. *Journal of Physical Chemistry B*, 109(32):15332–15338, 2005. 5.1, 6.1

[89] M. Furis, H. Htoon, M. A.Petruska, V. I. Klimov, T. Barrick, and S. A. Crooker. Bright-exciton fine structure and anisotropic exchange in cdse nanocrystal quantum dots. *Physical Review B (Condensed Matter and Materials Physics)*, 73(24):241313, 2006. 5.1, 5.3

[90] L.A. Swafford, L.A. Weigand, M.J. Bowers, J.R. McBride, J.L. Rapaport, T.L. Watt, S.K. Dixit, L.C. Feldman, and S.J. Rosenthal. Homogeneously alloyed $cds_x se_{1-x}$ nanocrystals: Synthesis, characterization, and composition/size-dependent band gap. *Journal of the American Chemical Society*, 128(37):12299–12306, 2006. 5.1

[91] G. F. Strouse. *Pending.* 5.2

[92] E.L. Ivchenko. Spectroscopy of spin-polarized excitons in semiconductors. *Pure & Appl. Chem.*, 67(3):463–472, 1995. 5.3, 5.3

[93] V. D. Kulakovskii, G. Bacher, R. Weigand, T. Kümmell, A. Forchel, E. Borovitskaya, K. Leonardi, and D. Hommel. Fine structure of biexciton emission in symmetric and asymmetric cdse/znse single quantum dots. *Phys. Rev. Lett.*, 82(8):1780–1783, Feb 1999. 5.3

[94] P. Tronc and Yu. E. Kitaev. Exact symmetries of electron bloch states and optical selection rules in [001] gaas/alas quantum wells and superlattices. *Phys. Rev. B*, 63(20):205326, May 2001. 5.3

[95] Hans A. Bethe. *Splitting of Terms in Crystals.* Consultants Bureau, New York, 1958. 5.3

[96] E. Molva and Le Si Dang. Magneto-optical study of li and na acceptor bound excitons in cdte: Fine structure and cubic crystal-field effect. *Phys. Rev. B*, 32(2):1156–1164, Jul 1985. 5.3

[97] J. A. Gupta, D. D. Awschalom, Al. L. Efros, and A. V. Rodina. Spin dynamics in semiconductor nanocrystals. *Phys. Rev. B*, 66(12):125307, Sep 2002. 5.3

[98] The $|1>$ states' behavior is similar to that of the known $|2>$ dark state. 5.3

[99] Dmitriy V. Melnikov and W. Beall Fowler. Bound polaron in a spherical quantum dot: Strong electron-phonon coupling case. *Phys. Rev. B*, 63(16):165302, Apr 2001. 5.3, 5.3

[100] Dmitriy V. Melnikov and W. Beall Fowler. Bound polaron in a spherical quantum dot: The all-coupling variational approach. *Phys. Rev. B*, 64(19):195335, Oct 2001. 5.3

[101] A. P. Alivisatos, T. D. Harris, P. J. Carroll, M. L. Steigerwald, and L. E. Brus. Electron–vibration coupling in semiconductor clusters studied by resonance raman spectroscopy. *The Journal of Chemical Physics*, 90(7):3463–3468, 1989. 5.3

[102] J. J. Shiang, I. M. Craig, and A. P. Alivisatos. Resonance raman depolarization in cdse nanocrystals. *Zeitschrift fr Physik D*, 26(1):358–360, 1993. 5.3

[103] M. C. Nuss, W. Zinth, and W. Kaiser. Femtosecond carrier relaxation in semiconductor-doped glasses. *Applied Physics Letters*, 49(25):1717–1719, 1986. 5.3

[104] Victor I. Klimov and Duncan W. McBranch. Auger-process-induced charge separation in semiconductor nanocrystals. *Phys. Rev. B*, 55(19):13173–13179, May 1997. 5.3

[105] Victor I. Klimov and Duncan W. McBranch. Femtosecond $1p$-to- $1s$ electron relaxation in strongly confined semiconductor nanocrystals. *Phys. Rev. Lett.*, 80(18):4028–4031, May 1998. 5.3

[106] V. Klimov, P. Haring Bolivar, and H. Kurz. Ultrafast carrier dynamics in semiconductor quantum dots. *Phys. Rev. B*, 53(3):1463–1467, Jan 1996. 5.3

[107] A. V. Malko, A. A. Mikhailovsky, M. A. Petruska, J. A. Hollingsworth, H. Htoon, M. G. Bawendi, and V. I. Klimov. From amplified spontaneous emission to microring lasing using nanocrystal quantum dot solids. *Applied Physics Letters*, 81(7):1303–1305, 2002. 6.1

[108] S. Dayal and C. Burda. Surface effects on quantum dot-based energy transfer. *Journal of the American Chemical Society*, 129(25):7977–7981, 2007. 6.1

[109] J. H. Park, D. G. Choi, T. K. Lee, Eunsoon Oh, Sanghoon Lee, and J. K. Furdyna. Localization and interdot carrier transfer in cdse and cdznmnse quantum dots determined by cw and time-resolved photoluminescence. *Applied Physics Letters*, 90(20):201916, 2007. 6.1

[110] M. Nirmal, C. B. Murray, and M. G. Bawendi. Fluorescence-line narrowing in cdse quantum dots: Surface localization of the photogenerated exciton. *Phys. Rev. B*, 50(4):2293–2300, Jul 1994. 6.1

[111] A. Javier, C. S. Yun, J. Sorena, and G. F. Strouse. Energy transport in cdse nanocrystals assembled with molecular wires. *Journal of Physical Chemistry B*, 107(2):435–442, 2003. 6.1

[112] C. de Mello Donega, M. Bode, and A. Meijerink. Size- and temperature-dependence of exciton lifetimes in cdse quantum dots. *Physical Review B (Condensed Matter and Materials Physics)*, 74(8):085320, 2006. 6.1

[113] V. I. Klimov, D. W. McBranch, C. A. Leatherdale, and M. G. Bawendi. Electron and hole relaxation pathways in semiconductor quantum dots. *Phys. Rev. B*, 60(19):13740–13749, Nov 1999. 6.1

[114] V. I. Klimov, A. A. Mikhailovsky, D. W. McBranch, C. A. Leatherdale, and M. G. Bawendi. Quantization of multiparticle auger rates in semiconductor quantum dots. *Science*, 287(5455):1011–1013, 2000. 6.1

[115] B. Esser. On the theory of resonance raman scattering in disordered semiconductors. *Phys. Stat. Sol. (b)*, 89(2):633–643, 1978. 10.1002/pssb.2220890238. 6.2

[116] D. L. Goodstein, editor. *States of Matter*. Diluted Magnetic Semiconductors. Dover Publications, Inc, New York, 1985. 6.2

BIOGRAPHICAL SKETCH

Donny Magana

EDUCATION

Institution	Concentration	Dates
Florida State University	Physical	2004-2007

PhD Chemistry Advisor: Professor Geoffrey Strouse

Research Title: Magnetic and Optical Properties of Doped nanomaterials

University of California, Santa Barbara	Physical	2002-2004

PhD Chemistry Advisor: Professor Geoffrey Strouse

Research Title: Magnetic and Optical Properties of Doped nanomaterials

University of California, Santa Cruz	Physical	June 2002

B.S. Chemistry Advisor: Professor Jin Z. Zhang

Research Title: Synthesis and Characterization of MnCdS

RESEARCH EXPERIENCE

August, 2002- 2004 Department of Chemistry and Biochemistry, Univiversity of California, Santa Barbara 2004- 2007 Department of Chemistry and Biochemistry, Florida State University

Advisor: Professor Geoff Strouse

-Synthesis of dilute magnetic semiconductor and metal nanoparticles -Magnetic characterization -Optical characterization

June, 2000- August, 2002 Department of Chemistry and Biochemistry, University of California, Santa Cruz

Advisor: Professor Jin Z. Zhang

-Synthesis of gold and Mn:ZnSe nanoparticles -Investigation of optical properties of nanoparticles

AWARDS

Mitsubishi chemical- Center for Advanced Materials Graduate Student award, UCSB, 2002-2003

UCLeads 2001-2002

PATENT

"Method for synthesis of colloidal nanoparticles" (UC Case 2004-218). US patent: 20060060998

ORAL PRESENTATIONS

"Paramagnetic groundstate of Mn:CdSe nanoparticles" Fame, 2007

"Formation of a Spin wave in Mn:CdSe" FIMS, 2006

"Magneto-photoluminescence of Mn:CdSe nanoparticles" Fame, 2006

"Magneto-optical properties of Mn:CdSe nanoparticles" Spring MRS, 2006

"Optical Properties of Dilute Magnetic Semiconductor Nanoparticles" Fall ACS, 2004

"Ferromagnetic Interactions in Manganese Cadmium Selenide nanoparticles" Fall MRS, 2003

REFEREED PUBLICATIONS

Chi-Dong Park, Donny Magana, and A. E. Stiegman "High-Quality Fe and -Fe2O3 Magnetic Thin Films from an Epoxide-Catalyzed Sol-Gel Process", Chem. Mat., ASAP, (2007).

Cristina Moisii, Eric W. Deguns, Adrian Lita, Sean D. Callahan, Lambertus J. van de Burgt, Donny Magana, A. E. Stiegman "Coordination Environment and Vibrational Spectroscopy of Cr(VI) Sites Supported on Amorphous Silica", Chem. Mat., 18(17), 3965-3975, (2006).

Donny Magana, Susanthri C. Perera, Andrew G. Harter, Naresh S. Dalal, Geoffrey F. Strouse, "Switching-on Superparamagnetism in Mn:CdSe Quantum Dots", J.Am.Chem.Soc., 128(9), 2931-2939, (2006).

Jeffrey A. Gerbec, Donny Magana, Aaron Washington, Geoffrey F. Strouse, "Microwave Enhanced Reaction Rates for Nanoparticle Synthesis", J.Am.Chem.Soc., 127(45), 15791-15800, (2005).

A. Javier, D. Magana, T. Jennings and G.F. Strouse, "Nanosecond Exciton Recombination Dynamics in Colloidal CdSe Quantum Dots Under Ambient Conditions" Appl. Phys. Let., 83, 1423 (2003).

Norman, Thaddeus J., Jr.; Magana, Donny; Wilson, Thea; Burns, Colin; Zhang, Jin Z.; Cao, Daliang; Bridges, Frank, "Optical and Surface Structural Properties of Mn2+-Doped ZnSe Nanoparticles." J. Phys. Chem. B, 107, 6309-6317, (2003).

T. Norman, Jr, C. Grant, D. Magana, D. Cao, F. Bridges, J. Liu, T. van Buuren, J. Z. Zhang, "Near infrared absorption of gold nanoparticle aggregates" J. Phys. Chem. B, 106, 7005-7012 (2002).